

OAK RIDGE
NATIONAL LABORATORY

MANAGED BY UT-BATTELLE
FOR THE DEPARTMENT OF ENERGY

ORNL/TM-2002/86

**Aspects of the Mechanical Behavior of Stitched
T300 Mat/Urethane 420 IMR Composite**

**S. Deng
X. Li
Y. J. Weitsman**



ORNL-27 (4-00)

DOCUMENT AVAILABILITY

Reports produced after January 1, 1996, are generally available free via the U.S. Department of Energy (DOE) Information Bridge.

Web site <http://www.osti.gov/bridge>

Reports produced before January 1, 1996, may be purchased by members of the public from the following source.

National Technical Information Service
5285 Port Royal Road
Springfield, VA 22161
Telephone 703-605-6000 (1-800-553-6847)
TDD 703-487-4639
Fax 703-605-6900
E-mail info@ntis.fedworld.gov
Web site <http://www.ntis.gov/supporVordernowabout.htrn>

Reports are available to DOE employees, DOE contractors, Energy Technology Data Exchange (ETDE) representatives, and International Nuclear Information System (INIS) representatives from the following source.

Office of Scientific and Technical Information
P.O. **Box** 62
Oak Ridge, TN 37831
Telephone 865-576-8401
Fax 865-576-5728
E-mail reports@adonis.osti.gov
Website <http://www.osti.gov/contact.html>

This report was prepared as an account of work sponsored by an agency of the United States Government. Neither the United States Government nor any agency thereof, nor any of their employees, makes any warranty, express or implied, or assumes any legal liability or responsibility for the accuracy, completeness, or usefulness of any information, apparatus, product, or process disclosed, or represents that its use would not infringe privately owned rights. Reference herein to any specific commercial product, process, or service by trade name, trademark, manufacturer, or otherwise, does not necessarily constitute or imply its endorsement, recommendation, or favoring by the United States Government or any agency thereof. The views and opinions of authors expressed herein do not necessarily state or reflect those of the United States Government or any agency thereof.

**ASPECTS OF THE MECHANICAL BEHAVIOR OF STITCHED
T300 MAT/URETHANE 420 IMR COMPOSITE**

S. Deng,* X. Li,* and Y. J. Weitsman*,†

*Department of Mechanical and Aerospace Engineering and Engineering Science, The University of Tennessee,
Knoxville, TN 37996

†Metals and Ceramics Division, Oak Ridge National Laboratory, *Oak Ridge*, TN 37831

October 2002

Prepared by
OAK RIDGE NATIONAL LABORATORY
Oak Ridge, Tennessee 37831
managed by
UT-BATTELLE, LLC
for the
U.S. DEPARTMENT OF ENERGY
under contract DE-AC05-00OR22725



CONTENTS

	Page
ABSTRACT	1
1. INTRODUCTION	1
2. MATERIALS	3
3. BASIC PROPERTIES	7
3.1 MICROSTRUCTURAL OBSERVATIONS	7
3.2 SPECIMEN PREPARATION	7
3.3 TENSILE TESTS	8
3.4 FAILURE RESPONSE	13
3.5 ANALYTICAL EVALUATION OF PLY PROPERTIES	13
3.5.1 Preliminaries	13
3.5.2 Evaluation of $Q_{11} + Q_{22}$, Q_{12} , and Q_{66}	27
3.5.3 Predictions for Other Orientations	28
3.6 EVALUATION OF Q_{11} AND Q_{22}	29
4. TIME-DEPENDENT DEFORMATION OF CROSSPLY LAYUPS	31
4.1 EXPERIMENTAL PROGRAM AND DATA	31
4.1.1 Tensile Tests	31
4.1.2 Creep and Recovery Tests	31
4.1.3 Additional Tests	34
4.2 DATA REDUCTION	36
4.2.1 Creep and Recovery	36
4.2.2 Long-Term Representation of Creep Data	41
5. PREDICTIONS FOR CROSSPLY BEHAVIOR	47
5.1 EFFECT OF LOAD ORIENTATION ANGLE ON CREEP	47
5.2 CREEP UNDER TWO-STEP STRESS INPUT	49
6. THE TIME-DEPENDENT AND NONLINEAR RESPONSE OF QUASI-ISOTROPIC LAYUPS	51
6.1 MATERIALS AND TESTING PROGRAM	51
6.2 LINEAR RANGE OF LAMINATE RESPONSE	52
6.2.1 Tensile Properties of $[0/90/45/-45]_S$ Laminates	52
6.3 STRESS-STRAIN BEHAVIOR IN THE NONLINEAR RANGE	55
6.3.1 Crossply Composite	55
6.3.2 Quasi-Isotropic Composite	56
6.3.3 Basic Nonlinear Properties and an Approximate Model	59
6.4 TIME-DEPENDENT RESPONSE	68
6.4.1 Data	68
6.4.2 Data Reduction	68
6.4.3 Correlation Between Tensile Response and Creep Behavior	70
6.4.4 Prediction of Creep Behavior of Quasi-Isotropic Composites Based on Crossply Viscoelastic Characterization	71
7. CONCLUSIONS	73
REFERENCES	75
Appendix A. POWER-LAW PARAMETERS	A-1
Appendix B. OPTIMAL DETERMINATION OF LINEAR PARAMETERS A_i AND NONLINEAR PARAMETERS τ_i OF THE PRONY SERIES	B-1

Appendix C. THE MODELING OF PLASTIC NONLINEARITY IN POLYMERIC COMPOSITES	C-1
Appendix D. OPTIMAL NONLINEAR LEAST-SQUARE DATA FITTING SCHEME TO DETERMINE THE PLASTIC PARAMETERS a , A , AND n	D-1
Appendix E. A MATHEMATICAL DEMONSTRATION FOR THE DEPARTURE FROM QUASI-ISOTROPY CAUSED BY NONLINEARITY	E-1

LIST OF FIGURES

Figure		Page
1	Micrographs of cross section with fibers at 0/90°: (a) at lower magnification, dark areas indicate fiber tows; (b) at higher magnification showing individual fibers within each tow	4
2	Schematic diagram for the cutting of the oriented specimens	7
3	Modulus vs orientation angle	10
4	Poisson's ratio vs orientation angle	11
5	Tensile strength vs orientation angle	11
6	Failure strain vs orientation angle	12
7(a)	Typical stress-strain response to failure at various orientation angles ([±45] _{6T})	12
7(b)	Typical stress-strain curves of [±45] _{3S} with loads applied at various orientations about the 0° fiber direction	13
8	Photographs of failed specimens after uniaxial tensile loading in horizontal direction: (a) failed 0° specimens; (b) an enlarged portion close to main crack	14
9	Micrographs of cross-section of 0° fracture surface: (a) at higher magnification; (b) at lower magnification	15
10	Photographs of failed specimens after uniaxial tensile loading in horizontal direction: (a) failed 30° specimens; (b) an enlarged portion close to main crack	16
11	Micrograph of a 30° specimen in the vicinity of the main crack region	17
12	Photographs of failed specimens after uniaxial tensile loading in horizontal direction: (a) failed 45° specimens; (b) an enlarged portion close to main crack	18
13	Micrograph of a 45° specimen around the main crack region	19
14	Photographs of failed specimens after uniaxial tensile loading in horizontal direction: (a) failed -45° specimens; (b) an enlarged portion close to main crack	20
15	Photographs of failed specimens after uniaxial tensile loading in horizontal direction: (a) failed 60° specimens; (b) an enlarged portion close to main crack	21
16	Photographs of failed specimens after uniaxial tensile loading in horizontal direction: (a) failed 70° specimens; (b) an enlarged portion close to main crack	22
17	Micrograph of a 70° specimen around the main crack region	23
18	Photographs of failed specimens after uniaxial tensile loading in horizontal direction: (a) failed 90° specimens; (b) an enlarged portion close to main crack	24
19	A unidirectionally reinforced ply with the principal axes of symmetry and state of stresses	25
20	Unidirectionally reinforced plies orientated at angles $\theta + \frac{\pi}{2}$ with loading applied relative to the common direction x and y	26

21	Variation of tensile stiffness within the linear range of stress-strain response vs loading orientation for $[\pm 45]_{3S}$ crossply laminates and comparison with predictions of classical laminate theory	28
22	Poisson's ratio vs loading orientation for $[\pm 45]_{3S}$ crossply laminates and comparison with predictions of classical laminate theory	28
23	The idealized model for the evaluation of E_2	29
24	Schematic drawing of the creep and recovery response of viscoelastic material: (a) step load input; (b) strain output	31
25	Average values and standard deviations for 5-h creep data of 45° coupons at 23°C and their power-law fits for various stress levels	33
26	Average values and standard deviations during 15-h recovery, following 5-h creep, and their power-law predictions under various stress levels for 45° coupons at 23°C	33
27	Creep and recovery data collected on a multigaged $[\pm 45]_{3S}$ coupon exhibiting nonuniform deformation within a test specimen	34
28	X-ray images showing damage in $[\pm 45]_{3S}$ composite ($\phi = 45^\circ$) at various stress levels	34
29	X-ray images showing damage after creep loading in $[45/-45]_{3S}$ composite ($\phi = 30^\circ$) at various stress levels	35
30	Typical creep and recovery curves of $[\pm 45]_{3S}$ laminate coupons ($\phi = 45^\circ$) at 23°C under various stress levels	36
31	Typical creep and recovery curves of $[\pm 45]_{3S}$ laminate coupons ($\phi = 45^\circ$) at 73°C under various stress levels	37
32	Comparison of the typical creep-recovery curves under the same stress level 31 MPa at different temperatures, showing the effect of temperature on the creep deformation	37
33	Comparison of the creep and recovery curves under different creep durations, showing the influence of creep time on the permanent deformation	38
34	Plot of permanent residual strain vs applied stress for 45° coupons at 23°C with different creep durations, showing the influence of stress and creep time on the permanent deformation	38
35	Plot of permanent residual strain vs applied stress for 45° coupons at different temperatures, showing the influence of stress and temperature on the permanent deformation	39
36	Plot of permanent residual strain vs applied stress for test coupons with three orientation angles, showing the influence of loading orientation on the permanent deformation	39
37	Typical creep data (upper plot) and the modified viscoelastic portion (lower plot)	40
38	Typical creep data and the power-law prediction with shift factor ($\phi = 45^\circ$, 5-h creep, 50°C)	41
39	Creep and recovery data and corresponding power-law fits: (a) creep, (b) recovery	42
40	Experimental creep and recovery data and modified power-law fits	43
41	Comparison of the predictions (Prony series and power-law models) to experimental creep and recovery data	45

42	Comparison of creep data from three replicate specimens with theoretical predictions for stress-strain response within the linear range ($\phi = 15^\circ$, 5-h creep, 23°C)	48
43	Comparison of creep data from three replicate specimens with theoretical predictions for stress-strain response within the linear range ($\phi = 34^\circ$, 5-h creep, 23°C)	48
44	Creep and recovery data of 0° coupons under stress levels of 168 MPa and 350 MPa ($\phi = 0^\circ$, 5 h creep, 15-h recovery, 23°C)	49
45	Experimental data and model prediction under a two-step load history for $[\pm 45]_{3S}$ coupons at 23°C	50
46	Illustration of quasi-isotropic laminates with layup misalignment	51
47	Stiffness vs orientation angle of quasi-isotropic composite at 23°C	53
48	Influence of laminate layup misalignment on the stiffness of quasi-isotropic composite	54
49	Typical stress-strain curves of crossply composite, with loads applied at orientation angle $\phi = 0^\circ$ under two temperatures	55
50	Typical stress-strain curves of crossply composite, with loads applied at orientation angle $\phi = 45^\circ$ under three temperatures	56
51	Typical stress-strain curves of quasi-isotropic composite at various orientations at 23°C	57
52	Typical stress-strain curves of quasi-isotropic stitched composite at various orientations at 50°C	57
53	Typical stress-strain curves of quasi-isotropic composite at various orientations at 73°C	58
54	Typical stress-strain curves of quasi-isotropic composite at various orientations at 120°C	58
55	Comparison of stress-strain curves of quasi-isotropic composite with two different loading orientations ($\phi = 0^\circ$ and 22.5°) at 120°C	59
56	Longitudinal and transverse strains vs stress for quasi-isotropic and $[\pm 45^\circ]_{3S}$ coupons at 120°C	60
57	Schematic drawing of strain compatibility requirements for composite laminates	61
58	Predicted and recorded values of longitudinal and transverse strains for the laminates and loading conditions noted in Fig. 55	64
59	Predictions of the anisotropic response of quasi-isotropic laminate beyond the linear range, under loading at various orientations about the fiber direction	66
60	Predicted values of the longitudinal and transverse components of plastic strains for quasi-isotropic laminates loaded at various orientations about the fiber direction and for $[\pm 45]_{3S}$ laminates	67
61	Maximal and minimal values of transverse plastic strain in the individual plies of a quasi-isotropic laminate loaded at 22.5° about the 0° fiber direction	67
62	Typical creep-recovery curves of quasi-isotropic composite with two orientations at 73°C	68
63	Typical creep-recovery curves of quasi-isotropic composite with two orientations at 120°C	69
64	Typical creep-recovery curves of quasi-isotropic composite with different loading orientations at 23°C	69

65	Typical stress-strain to failure response of quasi-isotropic composite at 120°C with loads applied at $\phi = 0^\circ$ and $\phi = 22.5^\circ$ about the fiber direction	71
66	Prediction of creep behavior of quasi-isotropic composite based on crossply viscoelastic characterization	72

LIST OF TABLES

Table		Page
1	The properties of T300 stitched mat/420 IMR urethane and neat resin (ACC data)	5
2	Tensile data for T300 stitched mat/STR-420 urethane IMR	8
3	Creep and recovery test program	32
4	Least-square error in correspondence to number of exponential parameters	44
5	Prony series parameters of fit to the early 5-h creep data in Fig. 20(a)	44
6	Creep and recovery test program	52
7	Tensile data for quasi-isotropic composite coupons loaded at various orientations	53
8	Parameters used for the simulations of the creep and recovery results ($\phi = 0^\circ, 73^\circ\text{C}$)	70
9	Parameters used for the simulations of the creep and recovery results ($\phi = 22.5^\circ, 73^\circ\text{C}$)	71
A.1	Best-fit power-law parameters D_0, D_1 , and n for creep data at 31 MPa and several temperatures.. ..	A-1
A.2	Best-fit power-law parameters D_0, D_1 , and n for creep data at 46.5 MPa and several temperatures.. ..	A-2



ASPECTS OF THE MECHANICAL BEHAVIOR OF STITCHED T300 MAT/URETHANE 420 IMR COMPOSITE

S. Deng, X. Li, and Y. J. Weitsman

ABSTRACT

This report presents experimental and analytical results concerning the behavior of crossply and quasi-isotropic laminates manufactured of stitch-bonded T300/urethane 420 IMR polymeric composites. Based on extensive creep and recovery data at various levels of stress and temperature, as well as on strain-to-failure information, it was possible to arrive at empirical expressions relating deformation to the previous input as well as to input duration. These expressions were incorporated within the formalisms of viscoelasticity and laminate theory to illuminate some basic underlying mechanistic aspects of the material at hand, thereby enabling the prediction of anticipated response under more complex stress and temperature inputs.

1. INTRODUCTION

Stitched T300/urethane 420 IMR composite is a candidate material for application in the automotive industry. This material consists of strands of T300 carbon fibers that are injected with urethane polymeric resin. Composites are formed by the light stitching of pairs of unidirectionally reinforced plies that are oriented perpendicularly to each other. Stitch lines run at 45° about the fiber direction and are spaced at 5 mm apart. Sets of crossply pairs are also laid up at ±45° to each other to form quasi-isotropic laminates. Details of the processing of these materials are provided elsewhere.¹⁻³

This report forms one part of an extensive study on the durability of polymeric composites for automotive applications that aims at the establishment of design criteria for these materials. The specific purpose of this report is to provide an understanding of some basic aspects that underlie the mechanical behavior of the material at hand. In this respect, the results presented here are a continuation of a previously published report.⁴ The issues discussed in the present report include basic lamina material properties, as well as time-dependent behavior and nonlinear response of both crossply and quasi-isotropic layups.

A comprehensive account of various other aspects of the mechanical response of this composite is provided elsewhere.¹⁻³

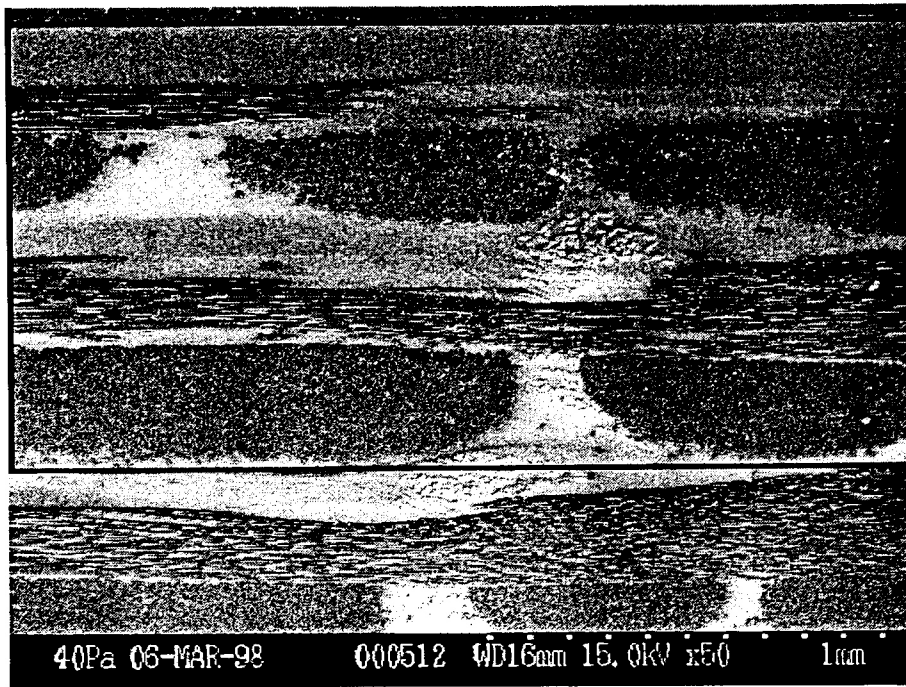


2. MATERIALS

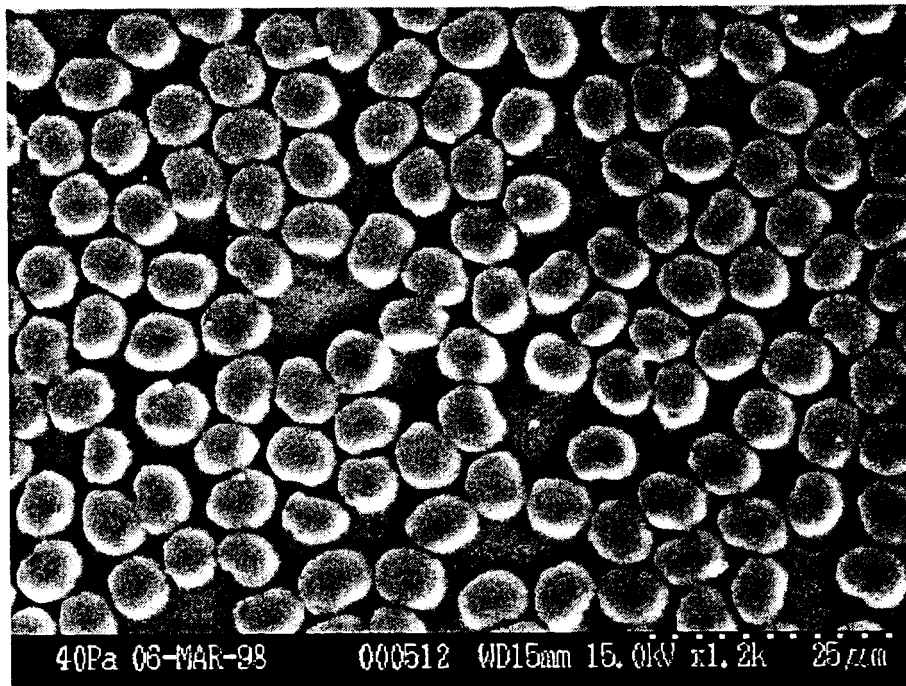
Several plaques, with in-plane dimensions of 610 mm by 610 mm, were provided by the Automotive Composite Consortium (ACC). The plaques were made of T300 stitch-bonded mat/420 IMR urethane with $[0/90]_{3S}$ and $[0/90]_6$ layups, while three additional plaques consisted of $[0/90/\pm 45]_S$ quasi-isotropic layups. The average thickness of the crossply plaques was 3 mm; that of the quasi-isotropic plaques varied between 2 and 2.4 mm. The stitched T300 mats were injected with urethane resin in a rapid injection molding process. Overall fiber volume fraction ranged between $41 \pm 4\%$. The matrix and the fiber tow configuration is detailed in **Figs. 1(a) and (b)**.^{*} Stitching was applied to each $[0/90]$ pair of layers, with stitches spaced at 5 mm apart to minimize the relative movement of the fiber strands during processing. Test coupons with dimensions of 203.2 mm by 25.4 mm were cut from the above plaques at various orientations ϕ about the fiber direction on the top ply, and crossply glass fiber/epoxy tabs, 1.6mm thick, were attached to these coupons in some circumstances.

Several mechanical properties are listed in Table 1.

^{*}See also Fig. 23.



(a)



(b)

Fig. 1. Micrographs of cross section with fibers at 0/90°: (a) at lower magnification, dark areas indicate fiber tows; (b) at higher magnification showing individual fibers within each tow.

Table 1. The properties of T300 stitched mat/420 IMR urethane and neat resin (ACC data)

<i>Composite (tensile properties)</i>	
Fiber volume fraction	39.0% to 44.3% (by weight)
Strength (0°/90°)	477 MPa
Modulus	46.7 GPa
Poisson's ratio	0.05
Failure strain	1.01%
<i>Neat resin (tensile properties)</i>	
Strength	68.2 MPa
Modulus	3.58 GPa ^a
Poisson's ratio	0.385
Failure strain	2.64%

^aA value of 2 GPa was employed in the sequel, based on data obtained at ORNL.



3. BASIC PROPERTIES

3.1 MICROSTRUCTURAL OBSERVATIONS

Two small samples were cut off from the crossply plaque along 0° and 90° fiber directions. The sample cross section was polished with alumina powder up to $1\ \mu\text{m}$. Micrographs were obtained from scanning electron microscopes (SEMs) and stored in digital format, as shown in Fig. 1. Figure 1(a) gives a low-magnification image where the dark area of the tow appears on the lighter background of the urethane resin. In the larger magnification image, exhibited in Fig. 1(b), individual fibers can be observed within the urethane matrix within the tow.

Particle analysis was performed on a Macintosh Centris 610 computer using the public domain NIH image program (version 1.60). Twenty micrographs similar to those shown in Fig. 1(b) were used to determine the fiber volume fraction within the tow, resulting in an average fiber volume fraction of 66.5% in that region. The average volume fraction of the tow within the composites was found to be 64.5%, which results in the overall fiber volume fraction of approximately 42.9%.

3.2 SPECIMEN PREPARATION

Forty-two crossply specimens, each measuring 203 mm long and 25 mm wide, were cut from the aforementioned plaques. The specimens were cut at different orientations, according to the cutting scheme shown in Fig. 2. After cutting, the specimens were dog-bone shaped with a nominal central width of 20 mm.

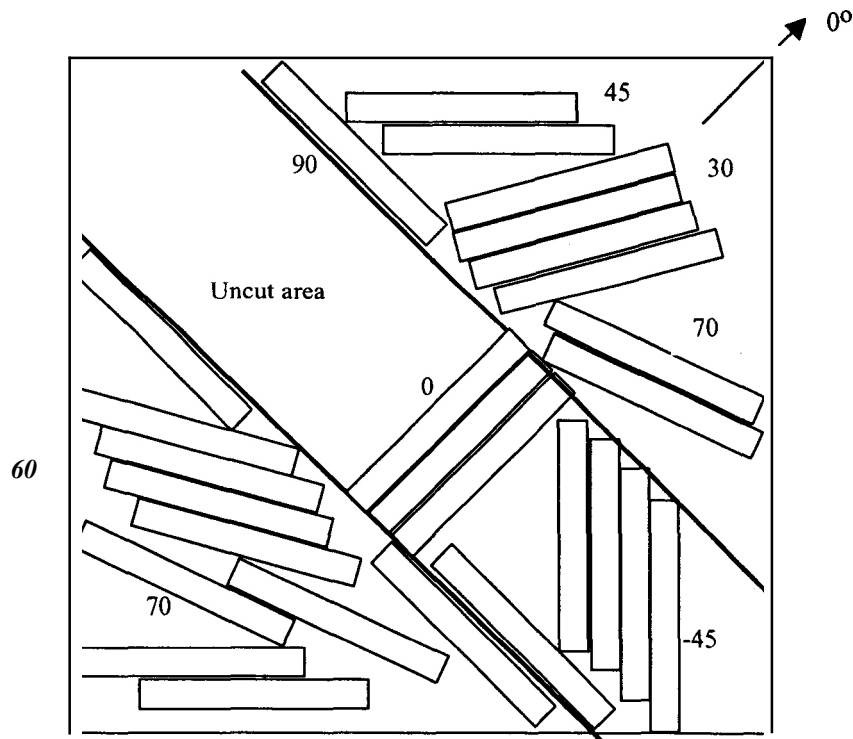


Fig. 2. Schematic diagram for the cutting of the oriented specimens.

3.3 TENSILE TESTS

All tensile tests were performed on an 810 MTS machine. For the crossply samples, two extensometers were used to measure longitudinal tensile strains on both sides of the specimen. In addition, two strain gages were mounted transversely to the loading direction with M-Bond 200 adhesive to measure transverse strain on both sides of the specimen. In accordance with the American Society for Testing and Materials (ASTM) D3039,⁵ the tests were carried out under displacement control at a loading rate of 1.27 mm/min. The measurements on the opposing faces of the test coupons were intended to detect the amount of bending that may be present due to layup asymmetry (such as in the $[0/90]_6$ plaques) or due to any other layup imperfections.

Results of the modulus, Poisson's ratio, tensile strength, and failure strain measurements are summarized in Table 2 and plotted in Figs. 3 to 7 for crossply specimens cut at various orientation angles. Although these results contain a degree of scatter, they nevertheless agree with the premise that they should exhibit symmetry about the 45° angle. The values plotted in Figs. 3 and 4 apply to the linear range of stress-strain response.

Typical stress-strain behavior to failure is shown in Figs. 7(a) for the $[\pm 45]_{6T}$ and 7(b) for the $[\pm 45]_{3S}$ layups. Note again the similarity in the behavior of coupons oriented at the paired angles of (0°; 90°), (30°; 60°), and (+45°; -45°).

Table 2. Tensile data for T300 stitched mat/STR-420 urethane IMR^a

Orientation (deg)	Specimen ID	Stiffness (GPa)	Poisson's ratio	UTS (MPa)	Failure strain (%)
0	C7-25	40.1	N/A	536.4	1.27
		48.7	N/A		1.05
	C7-26	43.5	0.040	506.9	1.10
		51.0	0.062		0.95
	C7-27	40.7	0.024	498.5	1.08
		46.6	0.116		1.10
Average		45.1	0.061	513.9	1.09
30	c7-5	13.8	N/A	166.9	N/A
		15.9	N/A		N/A
	c7-4	13.1	0.592	158.1	6.95
		13.4	0.752		7.21
	C7-6	12.8	0.509	159.1	5.69
		15.2	0.773		5.86
	c7-3	12.5	0.672	163.5	5.62
		14.8	0.900		4.51
Average		14.0	0.700	161.9	5.97

Table 2. (continued)

Orientation	Specimen ID	Stiffness (GPa)	Poisson's ratio	UTS (MPa)	Failure strain (%)
45	C7-23	11.0	N/A	145.5	5.50
		12.0	N/A		NIA
	C7-24	10.0	0.729	141.9	6.10
		11.5	0.750		5.10
	C7-2	10.8	0.759	139.9	4.00
		12.9	0.807		4.10
		12.5	0.760		4.50
C7-1	12.6	0.776	135.2	6.10	
	11.7	0.764		140.6	5.06
Average					
-45	C7-14	10.3	N/A	131.0	4.30
		10.9	N/A		N/A
	C7-13	9.6	0.660	133.1	4.84
		9.6	0.780		4.35
	C7-11	9.5	0.770	133.8	5.50
		10.6	0.672		5.70
	C7-12	8.8	0.630	127.4	4.90
		10.7	0.820		4.70
10.0		0.722	131.3		4.90
Average					
60	C7-18	14.5	N/A	179.3	5.62
		14.0	N/A		NIA
	C7-17	13.3	0.703	186.7	4.95
		14.0	0.694		4.76
	C7-20	12.5	0.671	163.7	7.66
		13.0	0.660		8.59
		12.3	0.770		5.67
C7-19	14.5	0.749	171.3	5.15	
	13.5	0.708		175.3	6.06
Average					
70	c7-7	23.4	N/A	248.2	3.10
		19.0	N/A		3.00
	C7-21	17.2	0.600	209.5	3.02
		18.5	0.503		3.18
	C7-22	18.9	0.614	236.2	3.01
		21.3	0.531		3.03
		19.7	0.695		231.3
	c7-8	23.0	0.500	231.3	2.52
20.1		0.574	231.3		2.96
Average					

Table 2. (continued)

Orientation (deg)	Specimen ID	Stiffness (GPa)	Poisson's ratio	UTS (MPa)	Failure strain (%)
90	C7-16	44.1	N/A	477.1	1.18
		38.6	N/A		
	C7-10	43.9	0.068	428.3	1.00
		42.7	0.051		
	C7-15	50.8	0.082	500.3	1.00
		47.4	0.045		
	c7-9	48.5	0.086	536.1	1.08
		44.7	0.038		
Average		45.1	0.062	485.5	1.08

^aNote that two values of stiffness, Poisson's ratio and failure strain, were evaluated based on the **two** sides of the specimen. N/A indicates that the value either was not measured or exceeded the capacity of the extensometer.

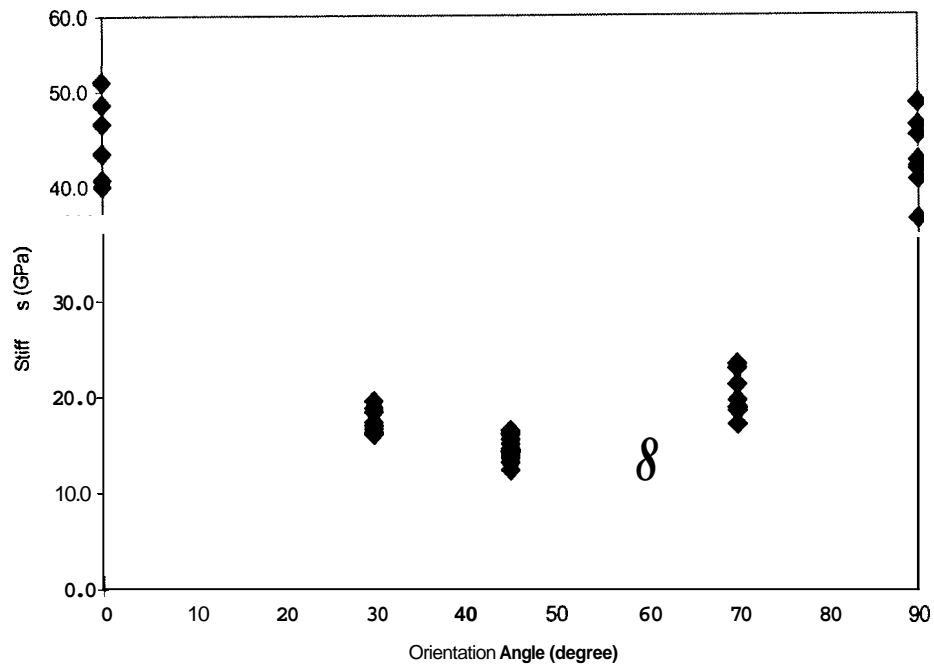


Fig. 3. Modulus vs orientation angle. Data scatter is partly due to the bending about specimens' midplanes.

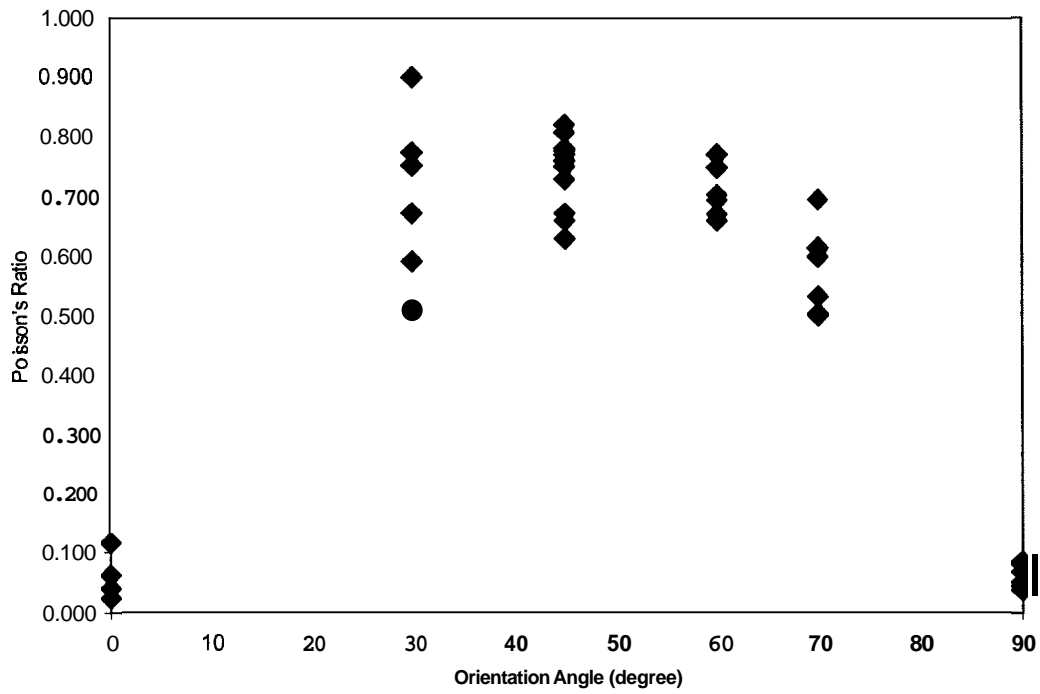


Fig. 4. Poisson's ratio vs orientation angle. Data scatter is partly due to the bending about specimens' midplanes.

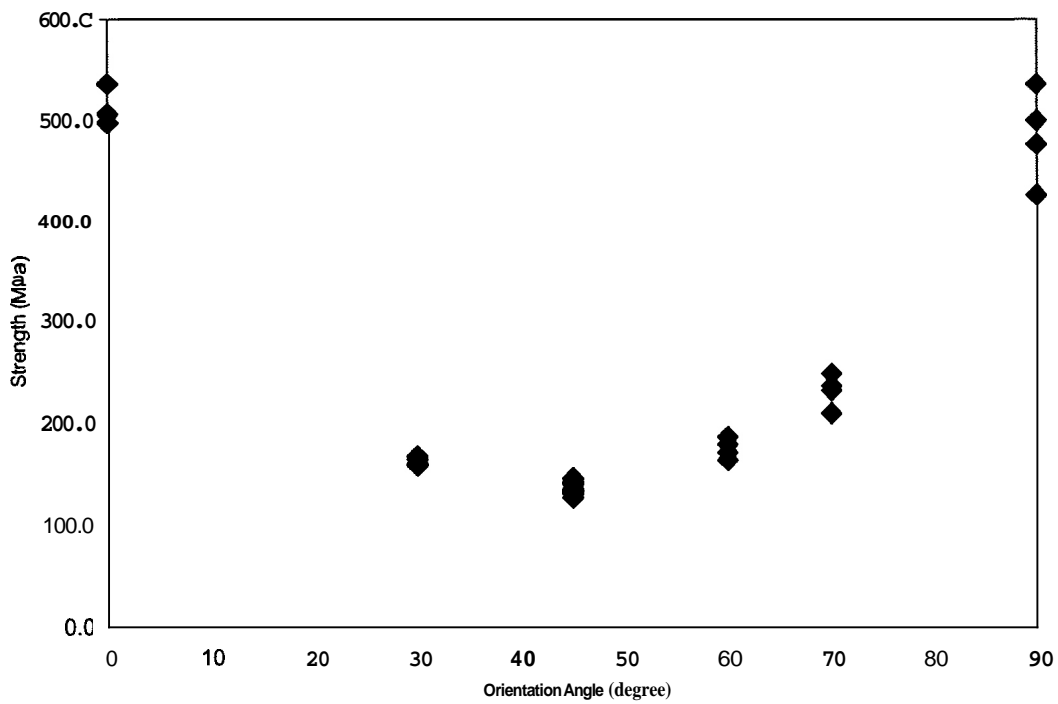


Fig. 5. Tensile strength vs orientation angle.

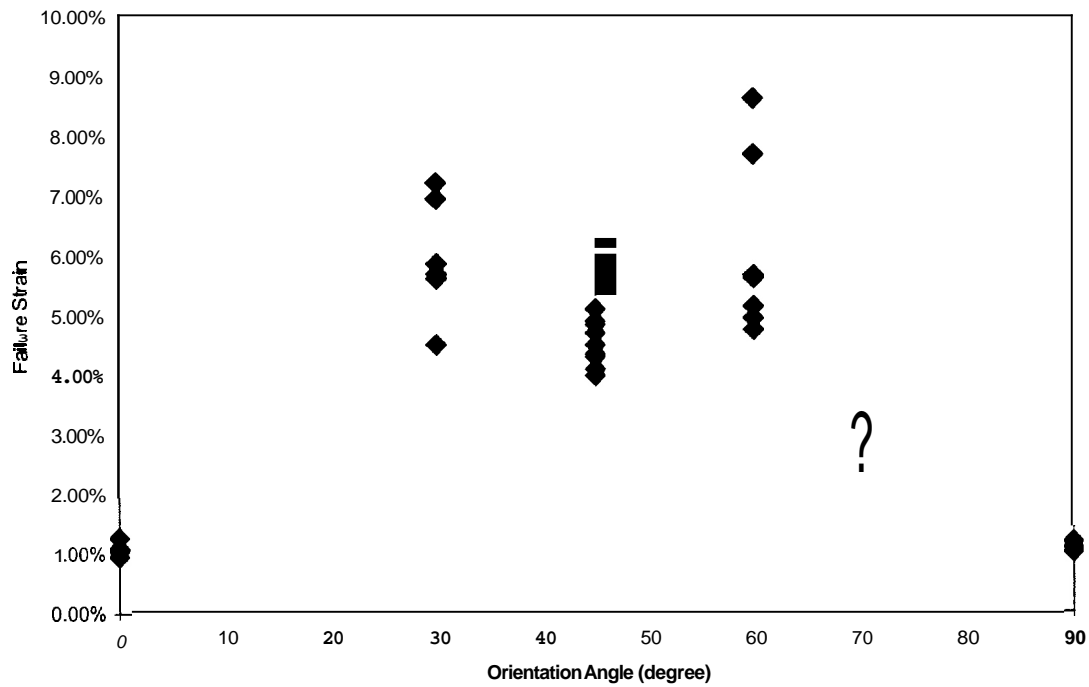


Fig. 6. Failure strain vs orientation angle.

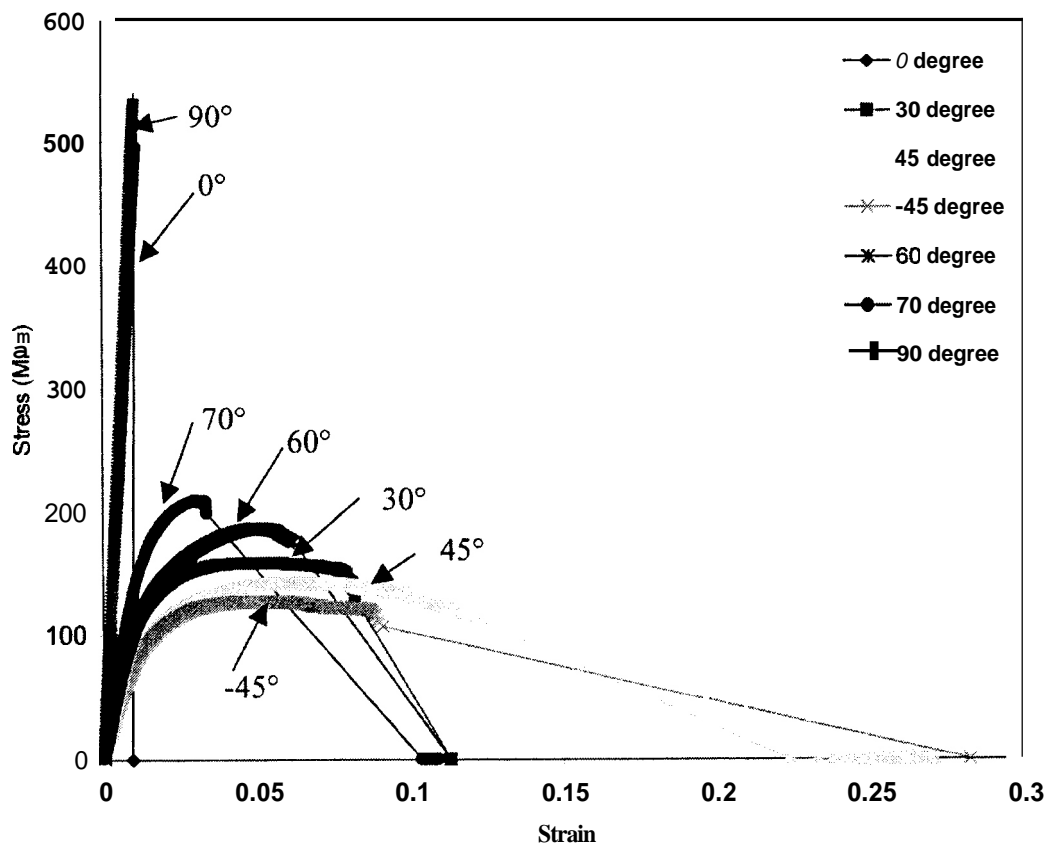


Fig. 7(a). Typical stress-strain response to failure at various orientation angles ($(\pm 45)_6T$).

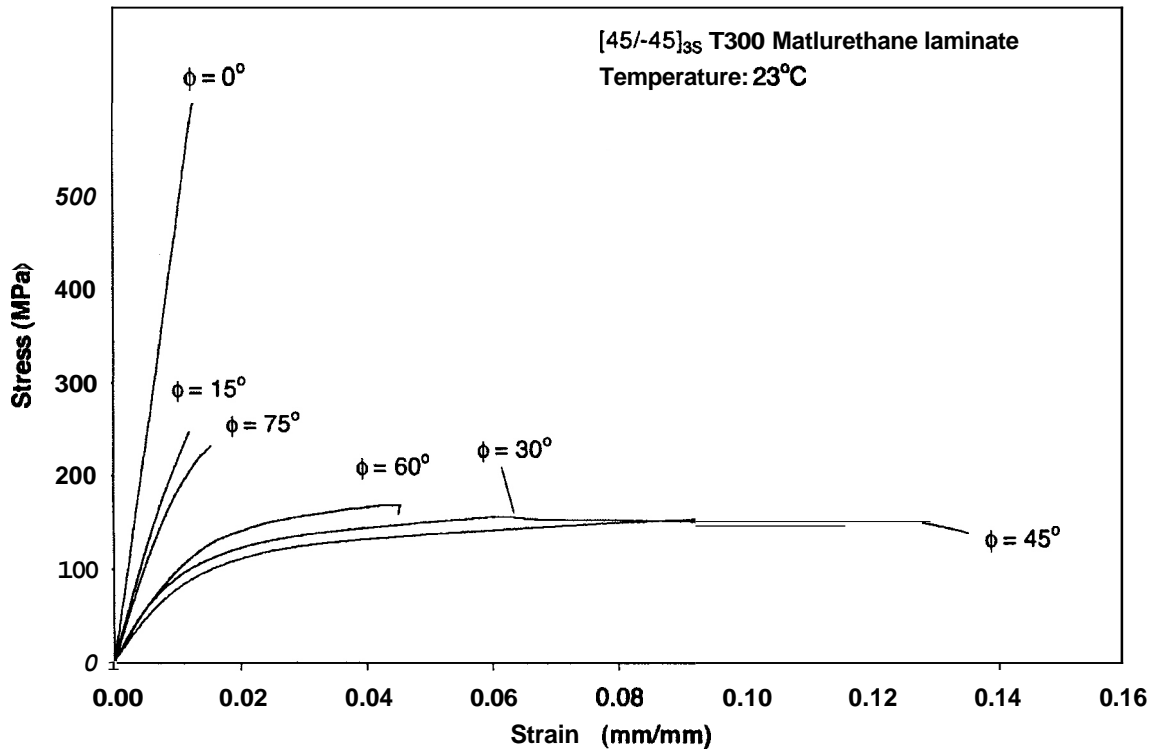


Fig. 7(b). Typical stress-strain curves of $[\pm 45]_{3S}$ with loads applied at various orientations about the 0° fiber direction.

3.4 FAILURE RESPONSE

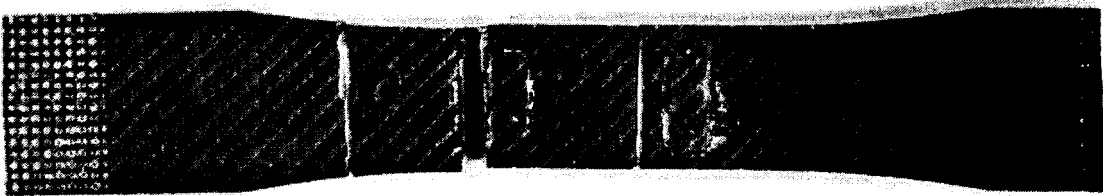
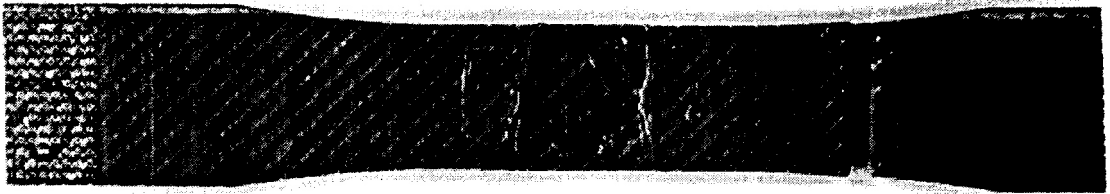
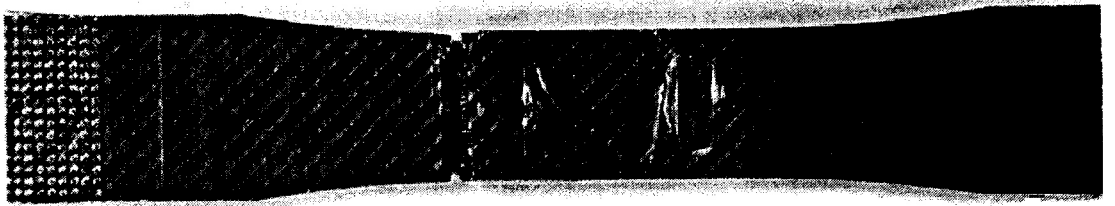
Photos and micrographs of the failed crossply specimens are shown in Figs. 8 to 18. Note that almost “clean breaks” appear for the coupons orientated at 0° and at 90° (Figs. 8 and 18); rough failure surfaces, which involve fiber pull-out, occur at all other angles. Nevertheless, the failure surfaces remain channeled parallel to the fiber directions, with negligible interference by the stitching orientation.

3.5 ANALYTICAL EVALUATION OF PLY PROPERTIES

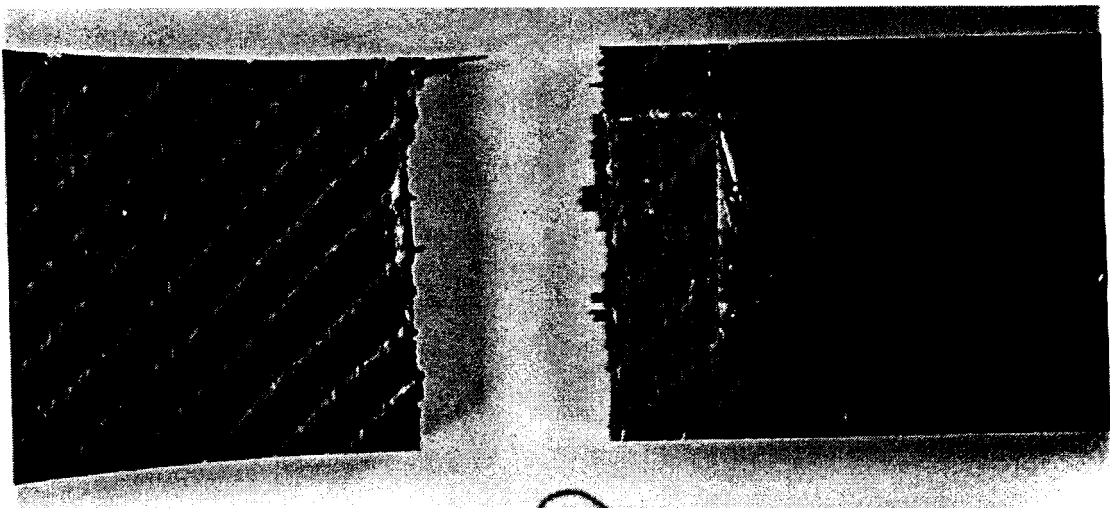
3.5.1 Preliminaries

In the analysis performed here, the basic properties of the individual ply are recovered from the foregoing crossply data through the employment of micromechanics and laminated plate theory.

The main purpose of this analysis is to determine if classic laminate plate theory, which applies in the linear-elastic range of response of laminates formed of plies that are reinforced by straight unidirectionally oriented fibers, remains valid for the current circumstance of a stitched, fiber-strand reinforced composite.

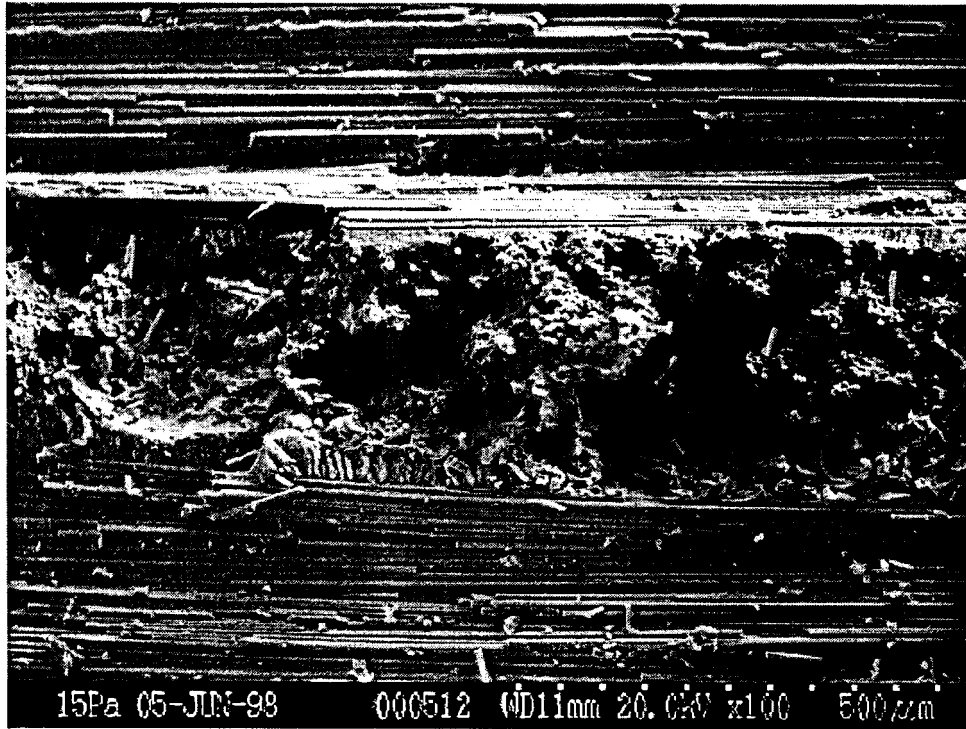


(a)

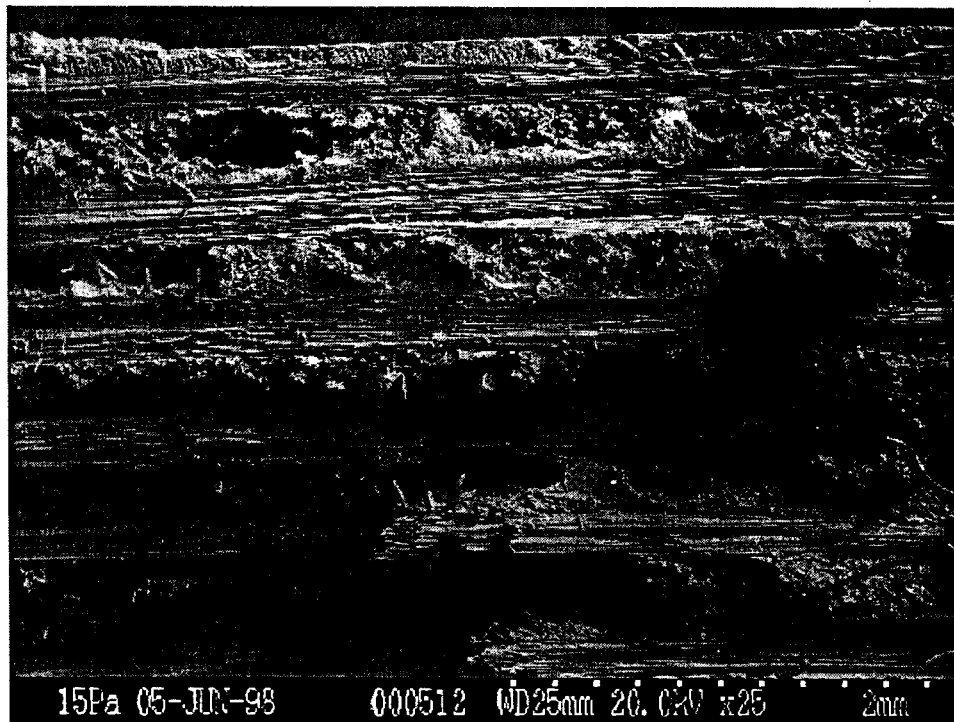


(b)

Fig. 8. Photographs of failed specimens after uniaxial tensile loading in horizontal direction: (a) failed 0° specimens; (b) an enlarged portion close to main crack.

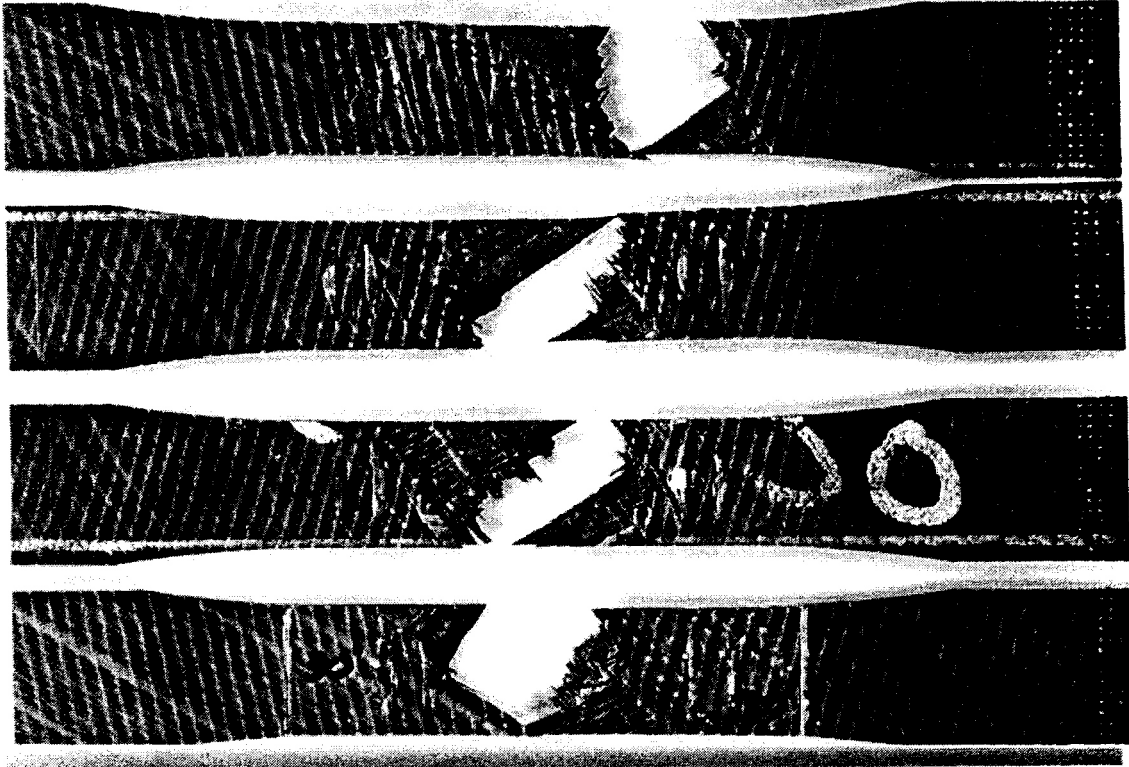


(a)

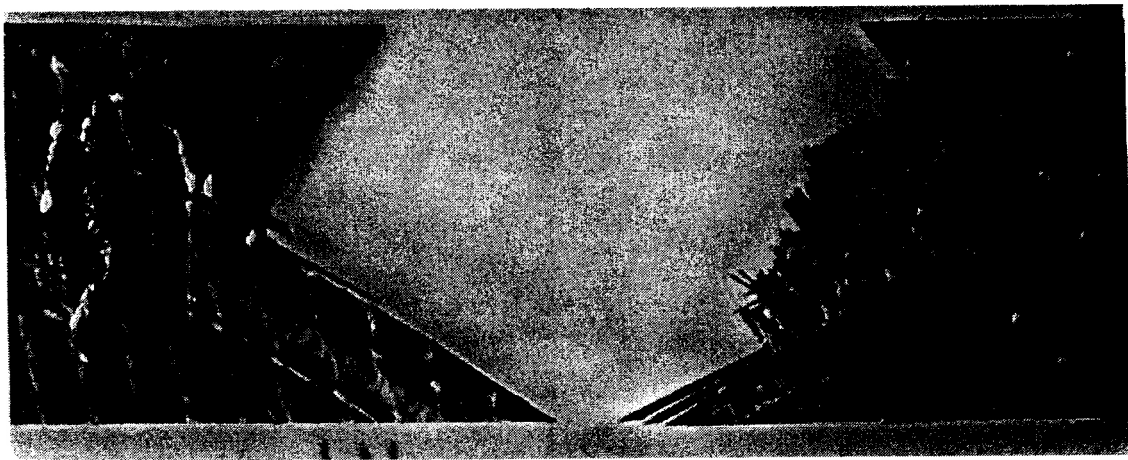


(b)

Fig. 9. Micrographs of cross-section of 0° fracture surface: (a) at higher magnification; (b) at lower magnification.



(a)

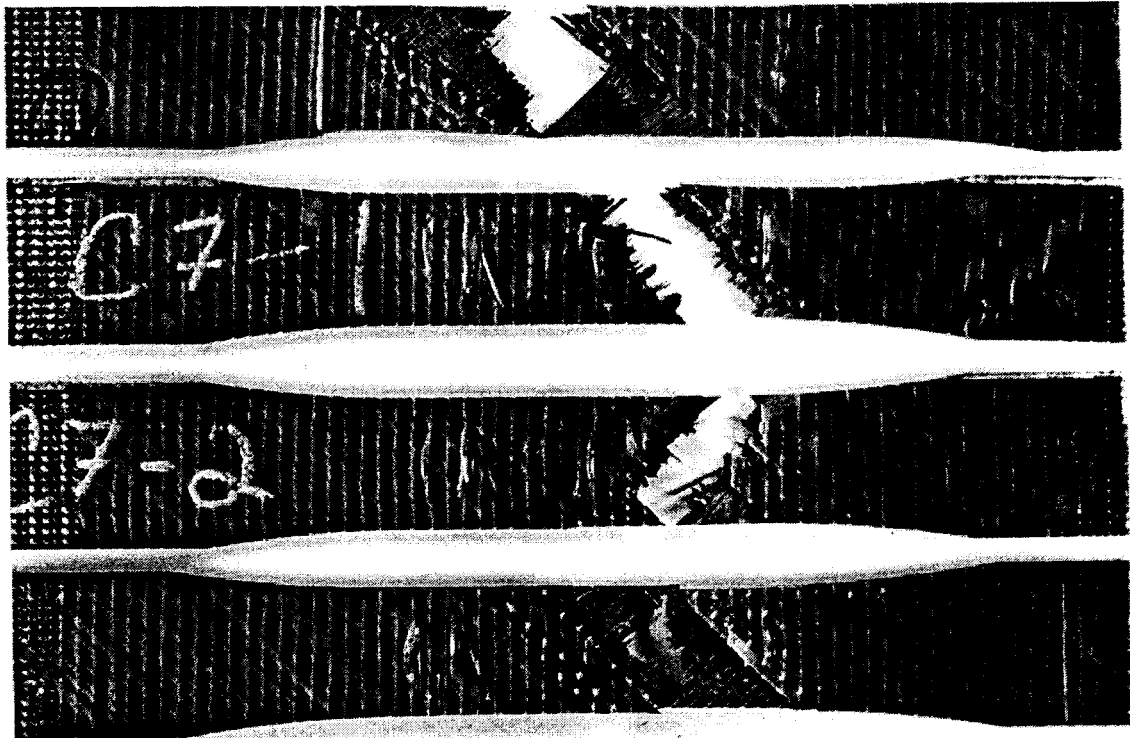


(b)

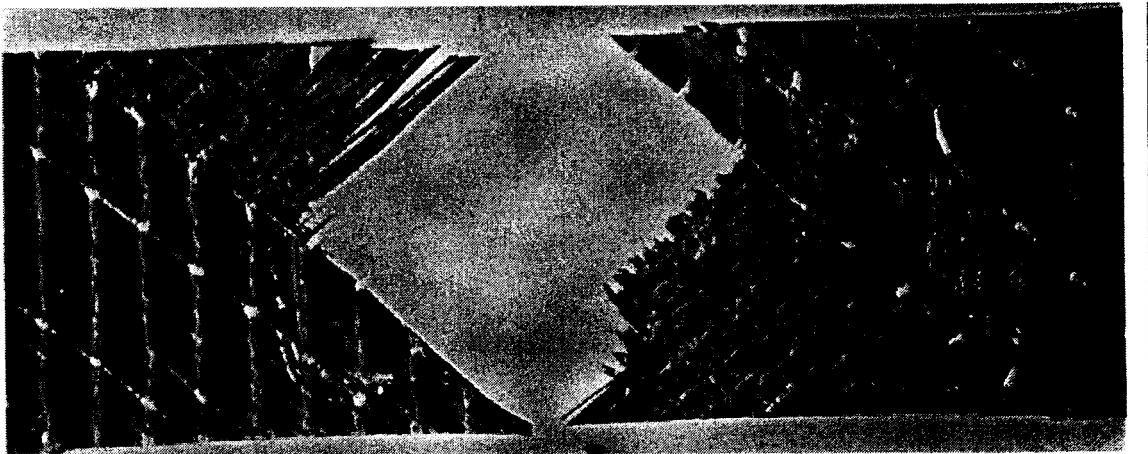
Fig. 10. Photographs of failed specimens after uniaxial tensile loading in horizontal direction: (a) failed 30° specimens; (b) an enlarged portion close to main crack.



Fig. 11. Micrograph of a 30° specimen in the vicinity of the main crack region. Secondary cracks were observed (note: specimen was loaded in vertical direction).



(a)



(b)

Fig. 12. Photographs of failed specimens after uniaxial tensile loading in horizontal direction: (a) failed 45° specimens; (b) an enlarged portion close to main crack.

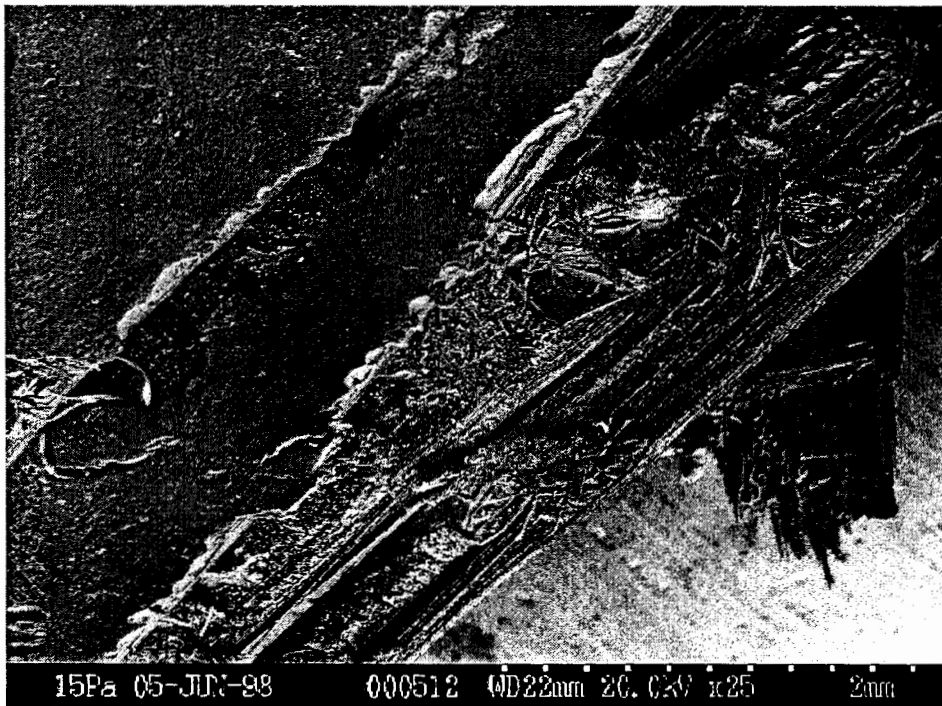
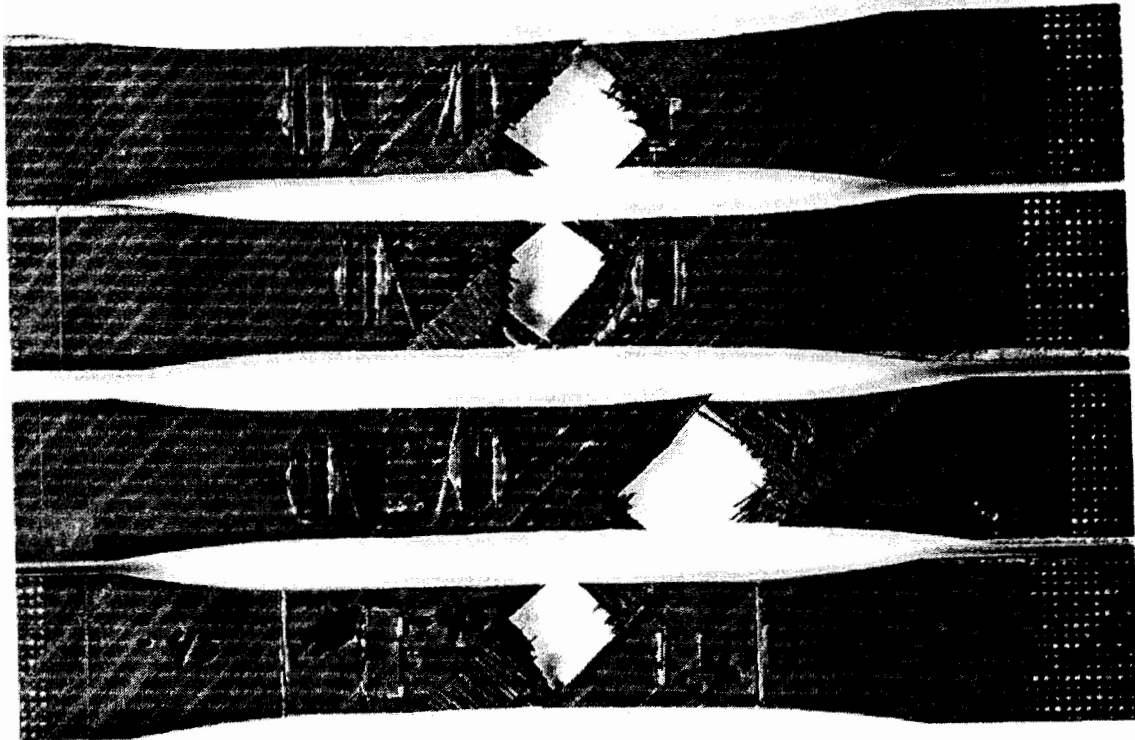
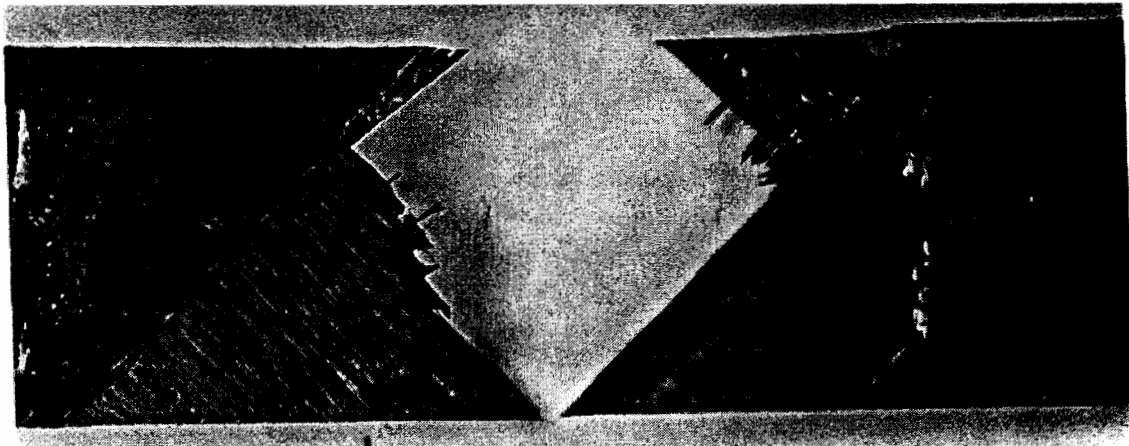


Fig. 13. Micrograph of a 45° specimen around the main crack region. Secondary cracks were observed (note: specimen was loaded in vertical direction).

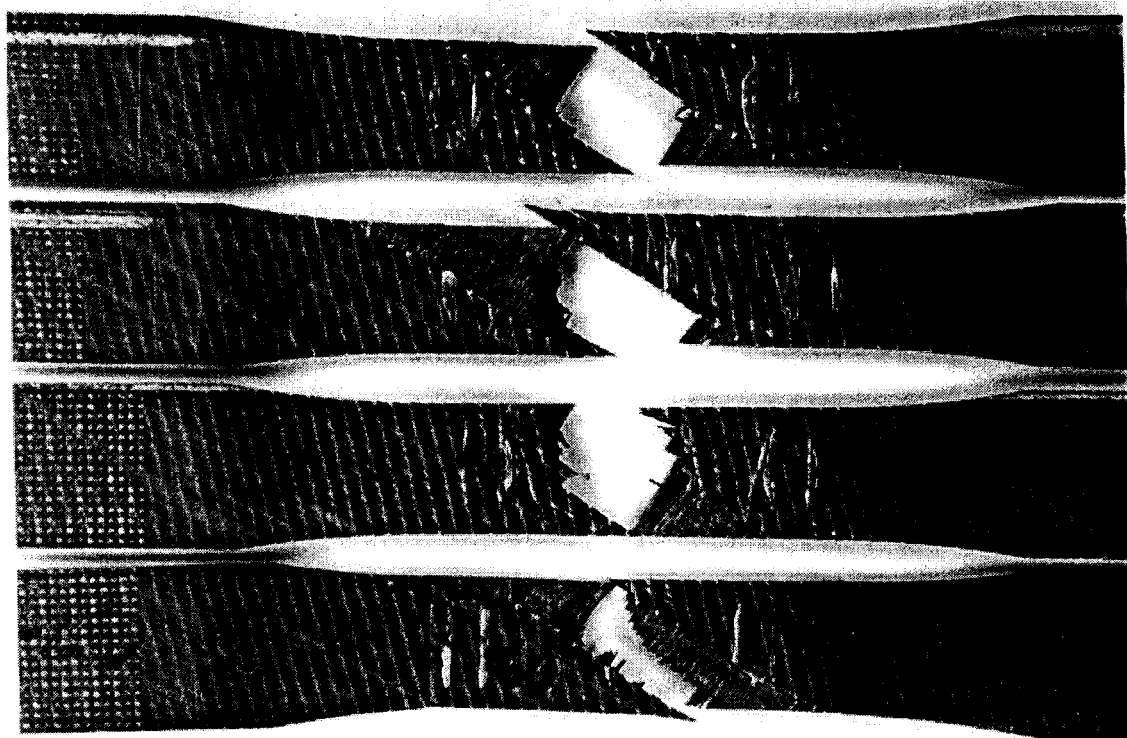


(a)



(b)

Fig. 14. Photographs of failed specimens after uniaxial tensile loading in horizontal direction: (a) failed -45° specimens; (b) an enlarged portion close to main crack.

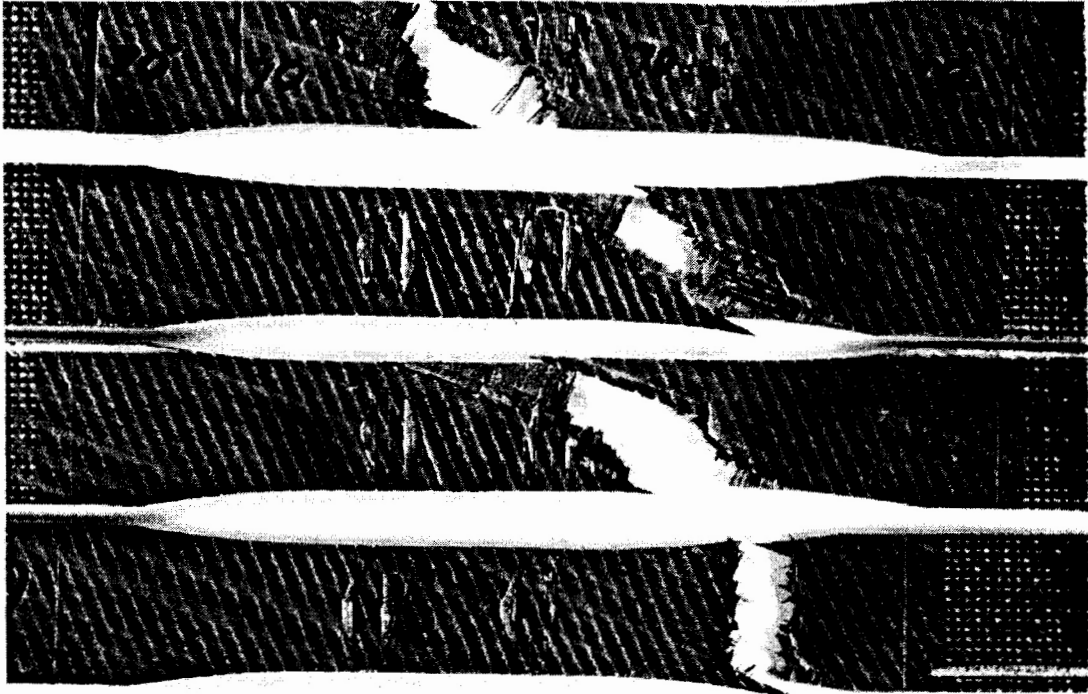


(a)

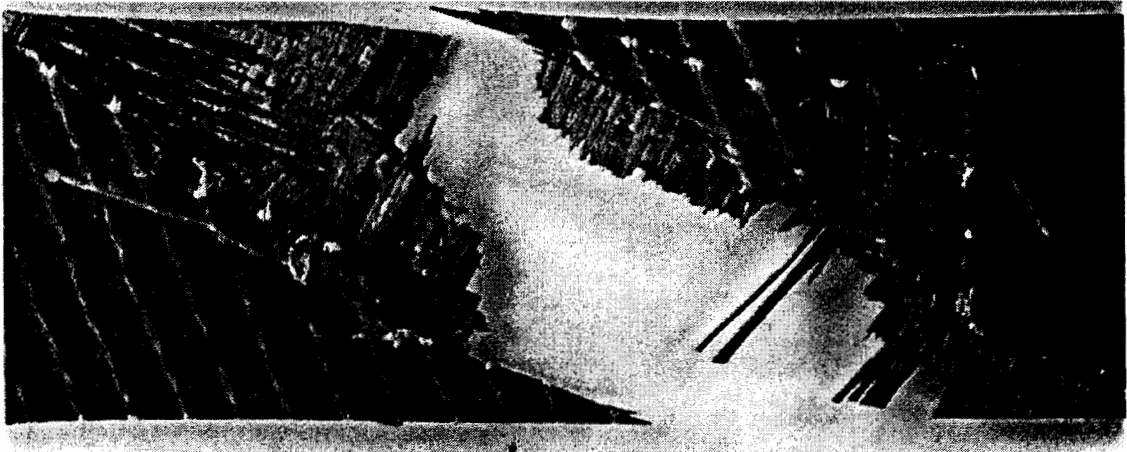


(b)

Fig. 15. Photographs of failed specimens after uniaxial tensile loading in horizontal direction: (a) failed 60° specimens; (b) an enlarged portion close to main crack.



(a)



(b)

Fig. 16. Photographs of failed specimens after uniaxial tensile loading in horizontal direction: (a) failed 70° specimens; (b) an enlarged portion close to main crack.

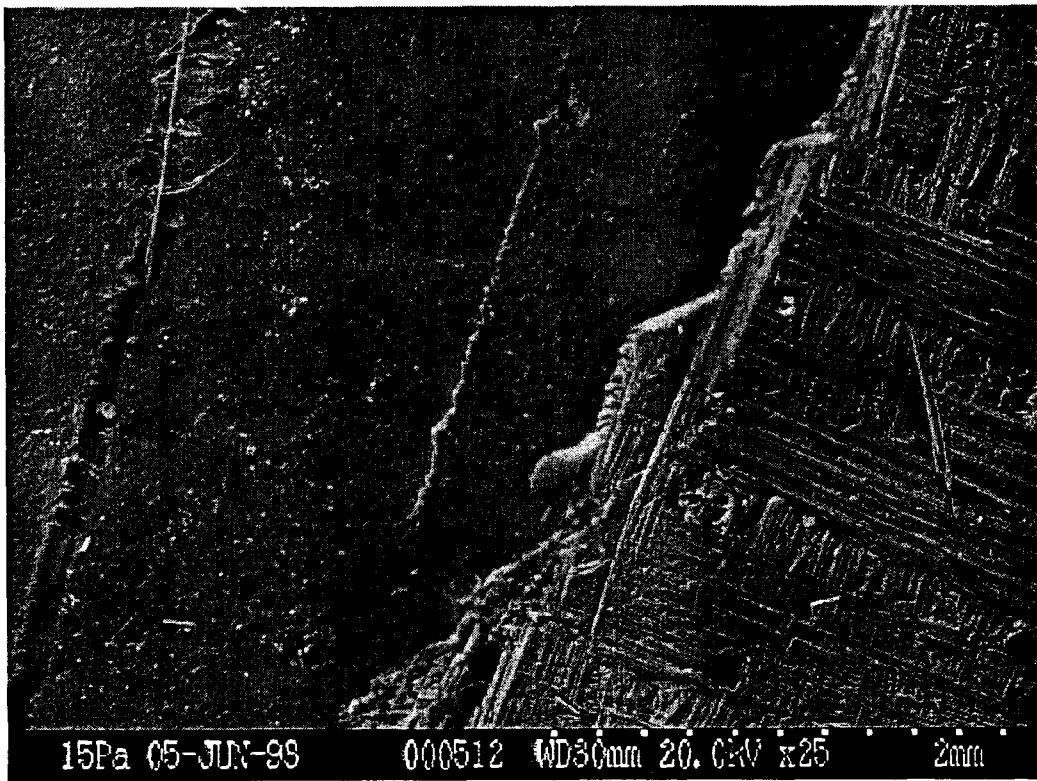
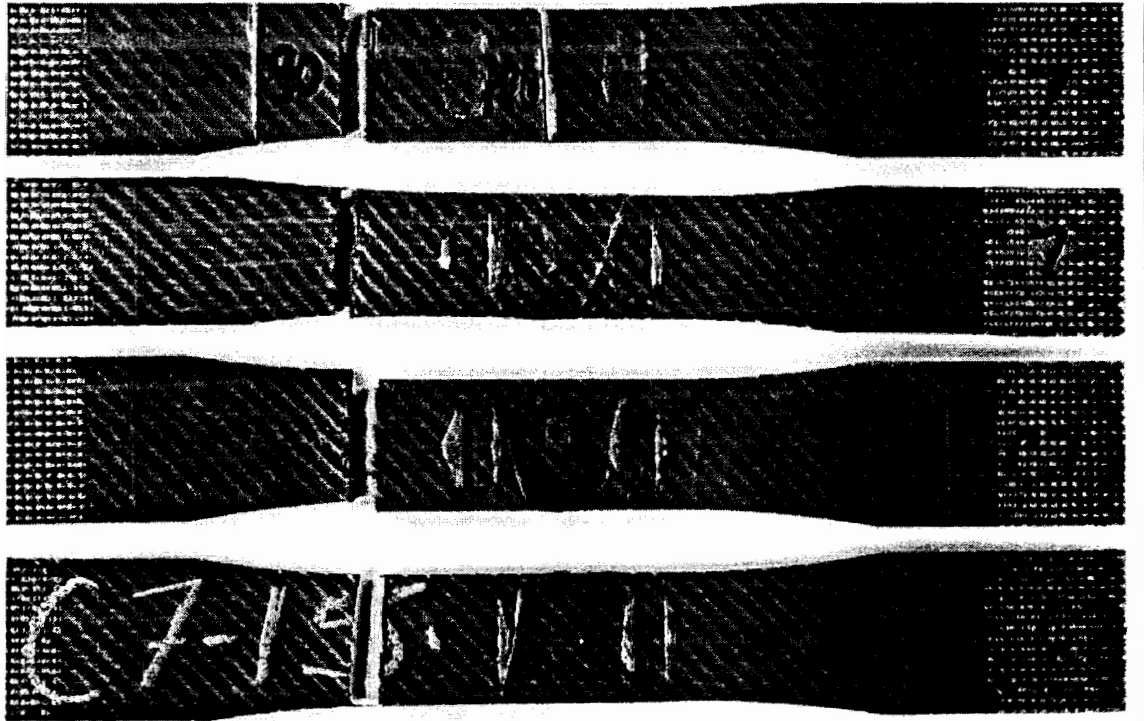
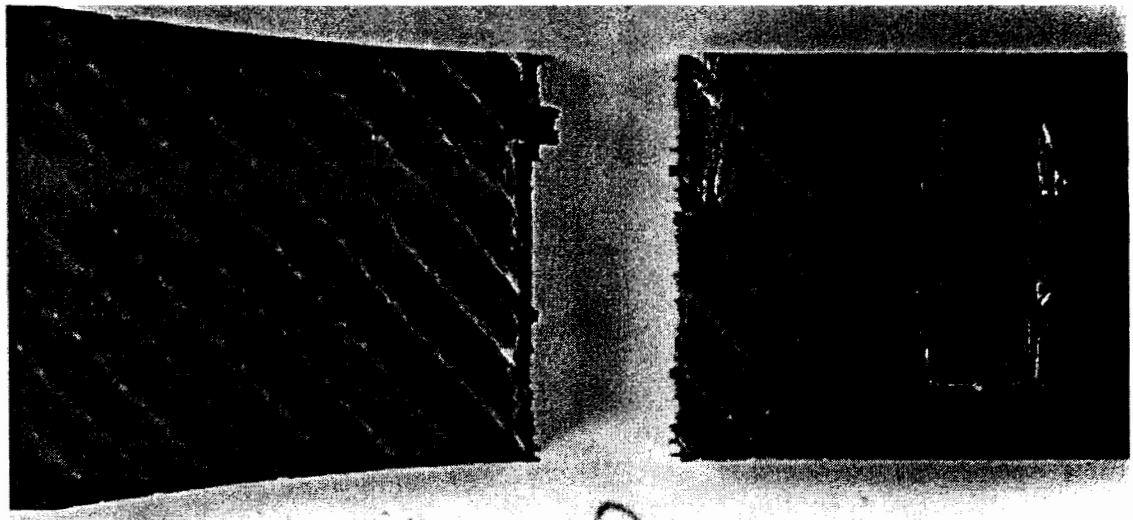


Fig. 17. Micrograph of a 70° specimen around the main crack region. Secondary cracks were observed (note: specimen was loaded in vertical direction).



(a)



(b)

Fig. 18. Photographs of failed specimens after uniaxial tensile loading in horizontal direction: (a) failed 90° specimens; (b) an enlarged portion close to main crack.

The basic linear-elastic properties of a unidirectionally reinforced lamina are the four in-plane, plane stress stiffnesses Q_{11} , Q_{12} , Q_{22} , and Q_{66} that relate stresses to strains in coordinate system X_1 and Y_1 , which coincides with the principal directions of ply symmetry, as shown in Fig. 19. Accordingly, one has⁶

$$\begin{aligned}\sigma_1 &= Q_{11}\varepsilon_1 + Q_{12}\varepsilon_2 \cdot \\ \sigma_2 &= Q_{12}\varepsilon_1 + Q_{22}\varepsilon_2 \cdot \\ \tau_6 &= Q_{66}\gamma_6 \cdot\end{aligned}\quad (1)$$

The above stiffnesses can be related in terms of the longitudinal and transverse moduli E_1 and E_2 as follows:

$$\begin{aligned}Q_{11} &= \frac{E_1}{1 - \nu_{12}\nu_{21}} \cdot \\ Q_{22} &= \frac{E_2}{1 - \nu_{12}\nu_{21}} \cdot \\ Q_{12} &= \frac{\nu_{21}E_1}{1 - \nu_{12}\nu_{21}} = \frac{\nu_{12}E_2}{1 - \nu_{12}\nu_{21}} \\ Q_{66} &= G_{12} \cdot\end{aligned}\quad (2)$$

In the above, ν_{12} is the Poisson's ratio that relates strain in the direction of Y_1 due to stress in the direction of X_1 and ν_{21} for the reverse case.

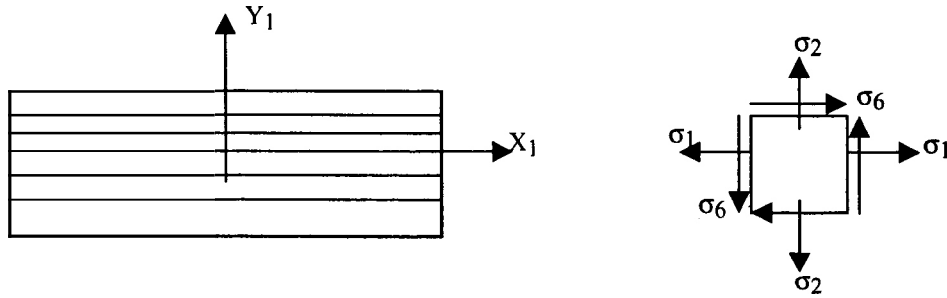


Fig. 19. A unidirectionally reinforced ply with the principal axes of symmetry and state of stresses.

When the lamina principal axes (X_1, Y_1) do not coincide with the loading direction (x, y) (as shown in Fig. 20), the stress-strain relations with respect to axes x and y take the following form:

$$\begin{Bmatrix} \sigma_x \\ \sigma_y \\ \tau_s \end{Bmatrix} = \begin{bmatrix} \bar{Q}_{11} & \bar{Q}_{12} & \bar{Q}_{16} \\ \bar{Q}_{12} & \bar{Q}_{22} & \bar{Q}_{26} \\ \bar{Q}_{16} & \bar{Q}_{26} & \bar{Q}_{66} \end{bmatrix} \begin{Bmatrix} \varepsilon_x \\ \varepsilon_y \\ \gamma_s \end{Bmatrix}, \quad (3)$$

where the oriented stiffnesses are related to the principal stiffnesses through tensorial transformation. For an orientation angle θ , measured positive counterclockwise from the x -axis to X_1 -axis, as shown in Fig. 20, the transformation relations read⁶ as follows:

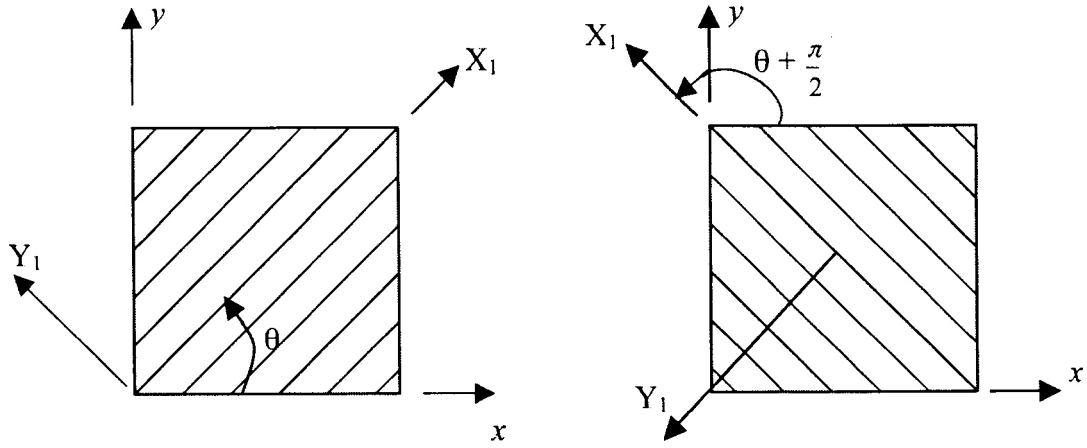


Fig. 20. Unidirectionally reinforced plies orientated at angles $\theta + \frac{\pi}{2}$ with loading applied relative to the common direction x and y .

$$\begin{aligned}
 \bar{Q}_{11} &= m^4 Q_{11} + n^4 Q_{22} + 2m^2 n^2 Q_{12} + 4m^2 n^2 Q_{66} , \\
 \bar{Q}_{22} &= n^4 Q_{11} + m^4 Q_{22} + 2m^2 n^2 Q_{12} + 4m^2 n^2 Q_{66} , \\
 \bar{Q}_{12} &= m^2 n^2 Q_{11} + m^2 n^2 Q_{22} + (m^4 + n^4) Q_{12} - 4m^2 n^2 Q_{66} , \\
 \bar{Q}_{16} &= m^3 n Q_{11} - mn^3 Q_{22} + (mn^3 - m^3 n) Q_{12} + 2(mn^3 - m^3 n) Q_{66} , \\
 \bar{Q}_{26} &= mn^3 Q_{11} - m^3 n Q_{22} + (m^3 n - mn^3) Q_{12} + 2(m^3 n - mn^3) Q_{66} , \\
 \bar{Q}_{66} &= m^2 n^2 Q_{11} + m^2 n^2 Q_{22} - 2m^2 n^2 Q_{12} + (m^2 - n^2)^2 Q_{66} ,
 \end{aligned} \tag{4}$$

in which, $m = \cos \theta$ and $n = \sin \theta$. For the angle $\theta + \frac{\pi}{2}$, the above equations can be reproduced by letting $m = -n$ and $n = m$. Straightforward manipulation of Eq. (4) yields the following expressions for the stiffnesses A , of symmetric, balanced, crossply laminates oriented at an angle θ about the x - y coordinate system:

$$\begin{aligned}
 A_{11} &= A_{22} = \frac{n_p}{2} h_o [(m^4 + n^4)(Q_{11} + Q_{22}) + 4m^2 n^2 (Q_{12} + 2Q_{66})] , \\
 A_{12} &= \frac{n_p}{2} h_o [2m^2 n^2 (Q_{11} + Q_{22}) + 2(m^4 + n^4) Q_{12} - 8m^2 n^2 Q_{66}] , \\
 A_{16} &= -A_{26} = \frac{n_p}{2} h_o [(m^3 n - mn^3)(Q_{11} + Q_{22}) + 2(mn^3 - m^3 n)(Q_{12} + 2Q_{66})] , \\
 A_{66} &= \frac{n_p}{2} h_o [2m^2 n^2 (Q_{11} + Q_{22}) - 4m^2 n^2 Q_{12} + 2(m^2 - n^2)^2 Q_{66}] ,
 \end{aligned} \tag{5}$$

where h_o is the lamina thickness, and n_p is the total number of plies.

Consequently, when subjected to a uniaxial load N_x , the longitudinal stiffness and the Poisson's ratio of the laminate are given by

$$E_x = \frac{1}{n_p h_o} \left(\frac{N_x}{\epsilon_x} \right) = \frac{1}{n_p h_o} \left(A_{11} - \frac{A_{12}^2 A_{66} + A_{66} A_{16}^2 - 2 A_{12} A_{16} A_{26}}{A_{22} A_{66} - A_{16}^2} \right), \quad (6)$$

and

$$\nu_{xy} = -\frac{\epsilon_y}{\epsilon_x} = \frac{A_{12} A_{66} - A_{16} A_{26}}{A_{22} A_{66} - A_{16}^2}. \quad (7)$$

Note that Eqs. (5), (6), and (7) contain the combined values of $Q_{11} + Q_{22}$, rather than Q_{11} and Q_{22} separately. This is a peculiarity that applies to symmetric, balanced, crossply laminates.

3.5.2 Evaluation of $Q_{11} + Q_{22}$, Q_{12} , and Q_{66}

Two laminate orientations, $\phi = 0^\circ$ and $\phi = 45^\circ$, were used to backtrack the lamina properties. The experimental data (reported in Table 2) gave average values of $E'' = 45.1$ GPa, $\nu_x^0 = 0.061$, $E_x^{45} = 11.7$ GPa, and $\nu_{xy}^{45} = 0.764$. For the case of $\phi = 45^\circ$, Eqs. (6) and (7) reduce to

$$E_x^{45} = \frac{1}{4} (Q_{11} + Q_{22}) + \frac{1}{2} (Q_{12} + 2Q_{66}) - \frac{\left[\frac{1}{2} (Q_{11} + Q_{22}) + Q_{12} - 2Q_{66} \right]^2}{Q_{11} + Q_{22} + 2Q_{12} + 4Q_{66}}, \quad (8)$$

and

$$\nu_{xy}^{45} = \frac{Q_{11} + Q_{22} + 2(Q_{12} - 2Q_{66})}{Q_{11} + Q_{22} + 2(Q_{12} + 2Q_{66})} \quad (9)$$

For $\phi = 0^\circ$, one obtains

$$E_x^0 = \frac{1}{2} (Q_{11} + Q_{22}) - \frac{2Q_{12}^2}{Q_{11} + Q_{22}}, \quad (10)$$

and

$$\nu_{xy}^0 = \frac{2Q_{12}}{Q_{11} + Q_{22}}. \quad (11)$$

Equations (8) to (11) yield four expressions for the three unknowns $Q_{11} + Q_{22}$, Q_{12} , and Q_{66} . In view of the unavailability of unidirectionally reinforced samples, these expressions, together with the experimental data for E_x^{45} , ν_{xy}^{45} , E'' , and ν_x^0 , employed in combinations of three sets at a time, yielded the following average values for the above three unknowns: $Q_{11} + Q_{22} = 91.7$ GPa, $Q_{12} = 3.1$ GPa, and $Q_{66} = 3.3$ GPa, with an uncertainty of approximately $\pm 5\%$ due to layup variabilities.

3.5.3 Predictions for Other Orientations

It is now possible to employ the foregoing values of $Q_{11} + Q_{22}$, Q_{12} , and Q_{66} together with Eqs. (5) to (7) to predict the laminate moduli and Poisson's ratio at all orientations ϕ . These predictions are shown in Figs. 21 and 22, where the average value of data recorded for $\phi = 30^\circ, 60^\circ, 70^\circ$, and 90° are shown to fit almost exactly with the predicted values.

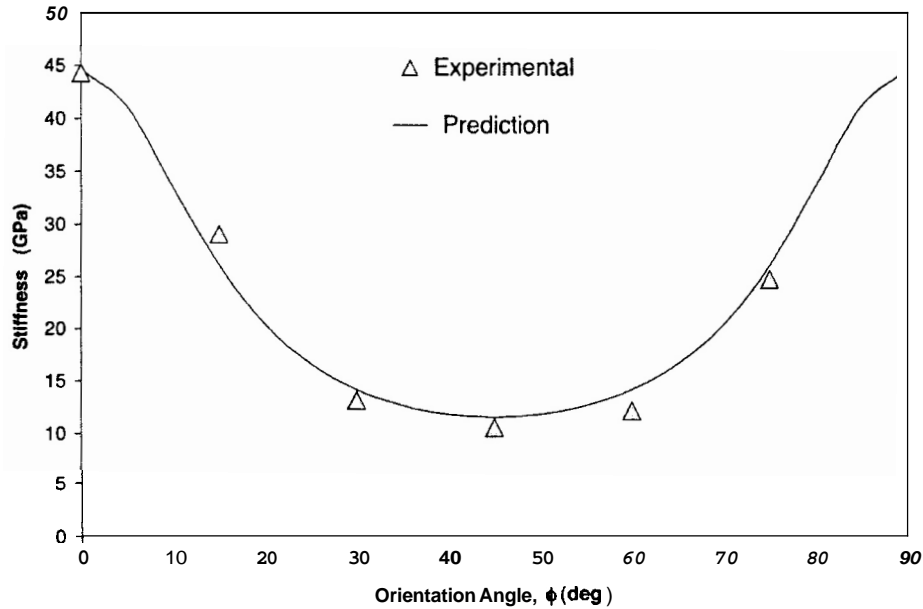


Fig. 21. Variation of tensile stiffness within the linear range of stress-strain response vs loading orientation for $[\pm 45]_{3S}$ crossply laminates and comparison with predictions of classical laminate theory.

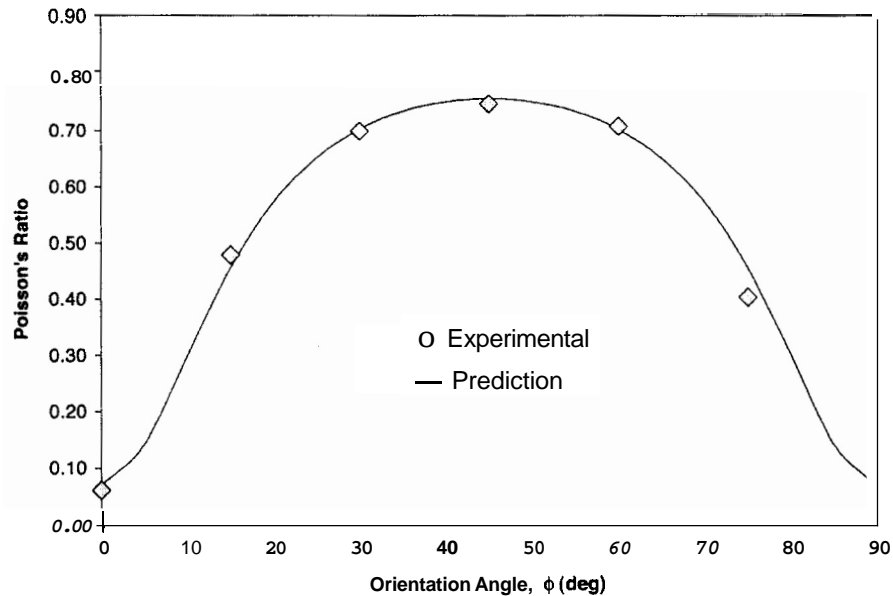


Fig. 22. Poisson's ratio vs loading orientation for $[\pm 45]_{3S}$ crossply laminates and comparison with predictions of classical laminate theory.

3.6 EVALUATION OF Q_{11} AND Q_{22}

As noted earlier, a peculiarity associated with symmetric, balanced, crossply laminates precludes the evaluation of Q_{11} and Q_{22} individually, though it is still possible to calculate their sum from laminate stress-strain data. For that purpose, the following properties were considered for the individual fiber and matrix phases:⁴

T300 fiber: $E_{1f} = 221$ GPa, $E_{2f} = 13.8$ GPa, and $\nu_{12}^f = 0.2$.
 Urethane matrix: $E_m = 2$ GPa and $\nu_m = 0.385$.

Furthermore, as noted earlier, one has $V_{Tow} = 64.5\%$ with $V_{f,Tow} = 66.5\%$. Thereby, $V_{m,Tow} = 33.5\%$; $V_{m,outside\ tow} = 35.5\%$ (thus, $V_f = 42.9\%$, $V_m = 57.1\%$).

Micromechanics considerations state that to a high degree of accuracy it is possible to assess the longitudinal modulus and Poisson's ratio of the unidirectionally reinforced composite ply by the rule of mixture. Thus,

$$E_x = V_f E_{1f} + V_m E_m = 96.9 \text{ GPa} ; \quad (12)$$

$$\nu_{12} = V_f \nu_{12}^f + V_m \nu_m = 0.31 . \quad (13)$$

Turning to the transverse modulus E_2 , the following assumptions are employed: (1) the fibers within the tow region are hexagonally arrayed, and (2) the two regions and the resin regions outside the tow are arrayed in series, as sketched in Fig. 23. Consequently, the transverse modulus within the tow region is evaluated according to the Halpin-Tsai expression:⁷

$$E_{2,Tow} = E_m \frac{1 + \xi \chi V_{f,Tow}}{1 - \chi V_{f,Tow}} . \quad (14)$$

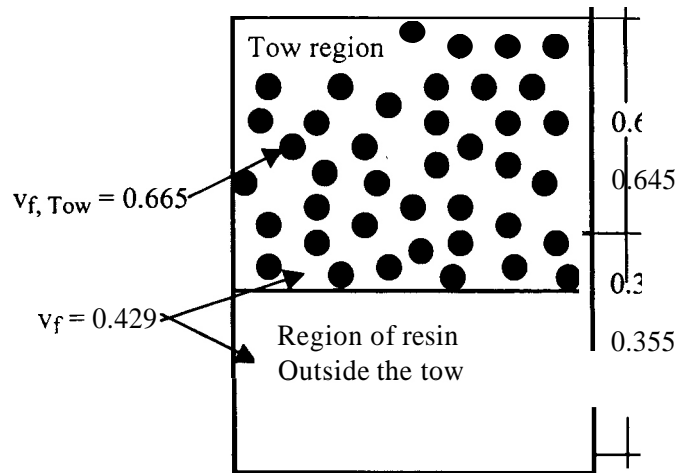


Fig. 23. The idealized model for the evaluation of E_2 . The quantity $v_{f,Tow}$ denotes the fiber volume fraction within the tow region, and v_f is the fiber volume fraction within the composite.

Thus, letting d denote fiber diameter and h the distance between the centers of neighboring fibers, one has $(d/h)^2 = 2\sqrt{3}V_{f,Tow}/\pi$, resulting in $d = 0.856h$. This, in turn, yields the following values for the auxiliary quantities $V_{mp,Tow}$, ξ , and χ : $V_{mp,Tow} = 0.012$, $\xi = 0.024$, and $\chi = 0.858$, whereby $E_{2,Tow} = 2.34$ GPa. The transverse modulus E_2 is now obtainable from the inverse rule of mixtures, which applies to phases arrayed in series; namely,

$$\frac{1}{E_2} = \frac{V_{Tow}}{E_{2,Tow}} + \frac{V_{m,outside tow}}{E_m} = \frac{0.645}{2.34} + \frac{0.355}{2}, \quad (15)$$

resulting in $E_2 = 2.25$ GPa. The quantities Q_{11} and Q_{22} can now be computed from

$$Q_{11} = \frac{E_1}{1 - \nu_{12}\nu_{21}}, \quad Q_{22} = \frac{E_2}{1 - \nu_{12}\nu_{21}}, \quad \nu_{21} = \frac{E_2}{E_1}\nu_{12}. \quad (16)$$

The above equations yield $Q_{11} = 95.7$ GPa, $Q_{22} = 2.24$ GPa, whereby $Q_{11} + Q_{22} = 97.94$ GPa. The latter result is close to, but not identical with, the average experimental value of 91.7 GPa. Reapportioning Q_{11} and Q_{22} through the factor of $91.7/97.94$, we finally get $Q_{11} \cong 89.6$ GPa and $Q_{22} = 2.1$ GPa.

4. TIME-DEPENDENT DEFORMATION OF CROSSPLY LAYUPS

4.1 EXPERIMENTAL PROGRAM AND DATA

4.1.1 Tensile Tests

Tension-to-failure tests were conducted using an 810MTS system at a constant rate of 1.016 mm/min (0.04 in./min) at temperatures of 23°C and 120°C. Longitudinal and transverse strains were recorded by strain gages and extensometry. The longitudinal strains vs stress at 23°C were shown earlier in Fig. 7.

4.1.2 Creep and Recovery Tests

Creep and recovery tests consisted of the application of a step stress of amplitude σ_0 and its subsequent removal after a time t_0 . Creep and recovery strains were recorded during the time intervals $0 < t < t_0$ and $t_0 < t < rt_0$, respectively. The values of r varied between 2 and 15. The resulting stress and strain histories are sketched in Fig. 24.

Replicate tests were performed at various levels of σ_0 , with several durations t_0 and rt_0 , at different levels of temperature and at various fiber orientations. These are listed in Table 3, where ϕ denotes orientation in degrees, and T is the temperature in degrees Celsius.

Typical results, accompanied by standard deviation scatter bands, are exhibited in Figs. 25 and 26 for $T = 23^\circ\text{C}$, $t_0 = 5$ h, $rt_0 = 20$ h (i.e., 15 h of recovery time) and various levels of σ_0 . Note the increase in data scatter with stress level σ_0 . Such an increase was also observed at higher test temperatures.

The abovementioned data scatter can be attributed to the inherent nature of multiphase materials where flaws and voids are randomly distributed. However, in the present case, those characteristics were compounded by the nonuniformity typical of the material at hand. As noted earlier, variances introduced during the manufacturing process resulted in localized nonuniformity in fiber and void volumes, resin impregnation, and fiber orientations. A somewhat extreme circumstance is exhibited in Fig. 27, where creep and recovery strains were recorded at various stations along the same test coupon. In this case, the onset of localized damage, in the form of non-uniformly distributed matrix cracks, resulted in vast discrepancies in the recorded strain data. The effects of stress, temperature, load duration, and load orientation on the time-dependent response of the composite at hand will be detailed in Sect. 4.2.1.

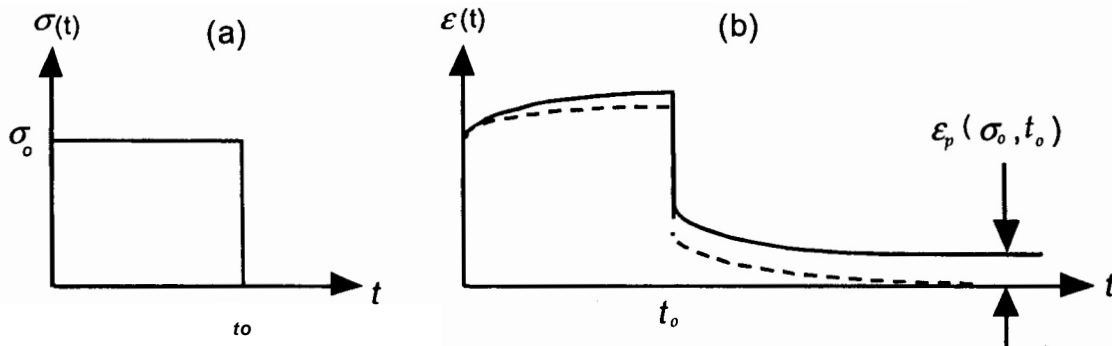


Fig. 24. Schematic drawing of the creep and recovery response of viscoelastic material: (a) step load input; (b) strain output. Solid line accounts for the permanent deformation, and the dashed line is the recoverable, viscoelastic component.

Table 3. Creep and recovery test program

Creep stress σ_0 (MPa)	Creep/recovery times $t_0/(r-1)t_0$ (h)	Number of test specimens	Creep stress σ_0 (MPa)	Creep/recovery times $t_0/(r-1)t_0$ (h)	Number of test specimens
$\phi = 45^\circ, T = 23^\circ\text{C}$			$\phi = 45^\circ, T = 120^\circ\text{C}$		
31	1/15	3	31	5/15	3
31	5/15	5	31	24/48	1
31	24/48	3	46.5	5/15	4
46.5	1/15	3	46.5	24/48	2
46.5	5/15	3	62	5/15	3
46.5	24/48	3	62	24/48	1
62	0/15	2	$\phi = 34^\circ, T = 23^\circ\text{C}$		
62	1/15	3	32.8	5/15	3
62	5/15	6	32.8	24/48	3
62	24/48	3	49.2	5/15	3
77.5	0/15	2	49.2	24/48	3
77.5	1/15	3	65.5	5/15	3
77.5	5/15	3	65.5	24/48	3
77.5	24/48	3	82	5/15	3
93	0/15	2	96	5/15	3
93	1/15	3	$\phi = 340, T = 50^\circ\text{C}$		
93	5/15	4	32.8	5/15	2
93	24/48	3	49.2	5/15	2
108.5	1/15	3	$\phi = 34^\circ, T = 73^\circ\text{C}$		
108.5	5/15	4	32.8	5/15	1
108.5	24/48	4	$\phi = 15^\circ, T = 23^\circ\text{C}$		
$\phi = 45^\circ, T = 50^\circ\text{C}$			31	24/48	1
31	5/15	3	50.4	5/15	3
46.5	5/15	3	50.4	24/48	5
$\phi = 45^\circ, T = 73^\circ\text{C}$			75.6	5/15	3
31	1/15	3	75.6	24/48	3
31	5/15	3	100.8	5/15	3
31	24/48	3	100.8	24/48	4
46.5	1/15	3	126	5/15	3
46.5	5/15	4	126	24/48	3
46.5	24/48	4	151	5/15	4
62	1/15	2	151	24/48	4
62	5/15	3	$\phi = 0^\circ, T = 23^\circ\text{C}$		
62	24/48	2	168	5/15	4
77.5	1/15	1	350	5/15	2
77.5	5/15	3	$\phi = 0^\circ, T = 73^\circ\text{C}$		
77.5	24/48	2	226	5/15	1
93	1/15	2	$\phi = 0^\circ, T = 120^\circ\text{C}$		
93	5/15	6	395	5/15	1
93	24/48	2			

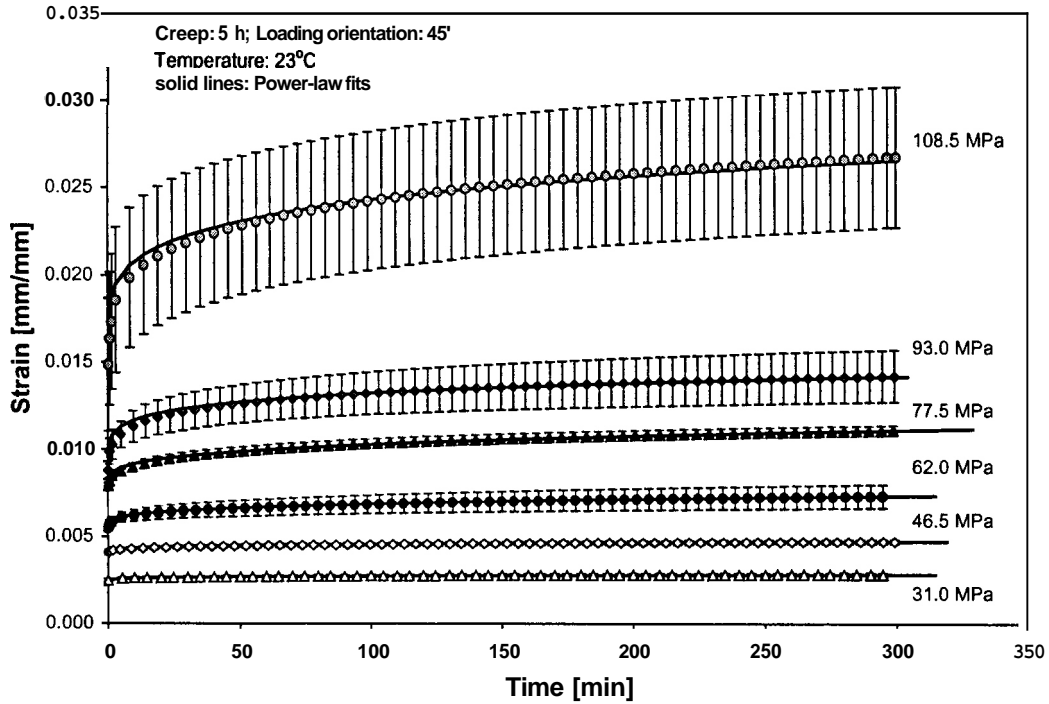


Fig. 25. Average values and standard deviations for 5-h creep data of 45° coupons at 23°C and their power-law fits for various stress levels.

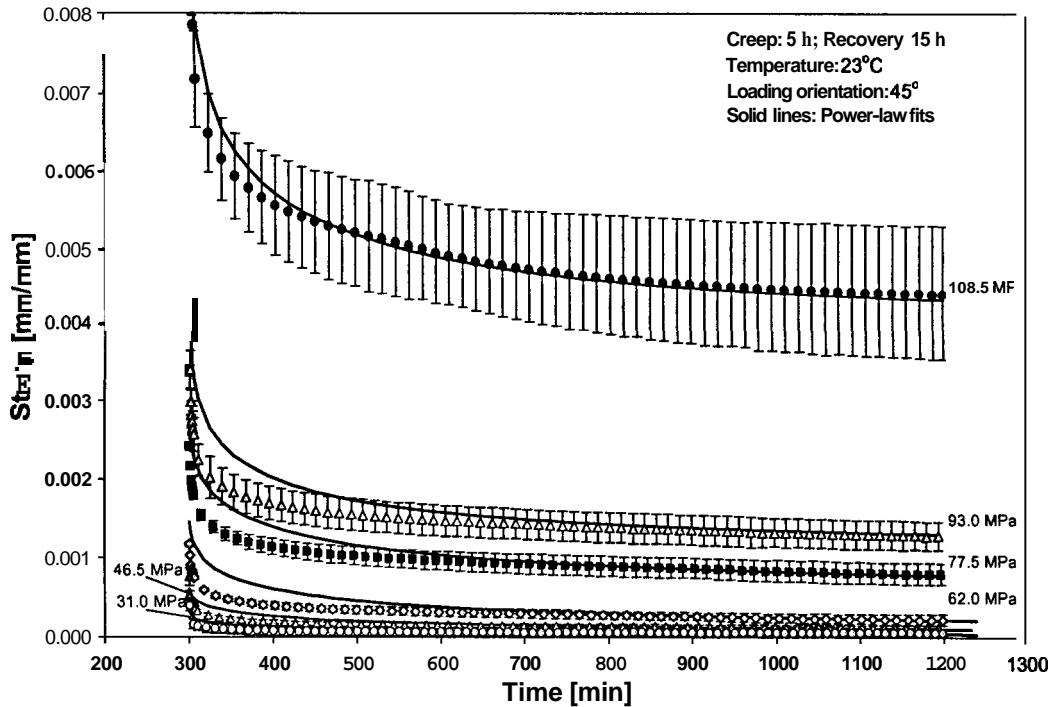


Fig. 26. Average values and standard deviations during 15-h recovery, following 5-h creep, and their power-law predictions under various stress levels for 45° coupons at 23°C.

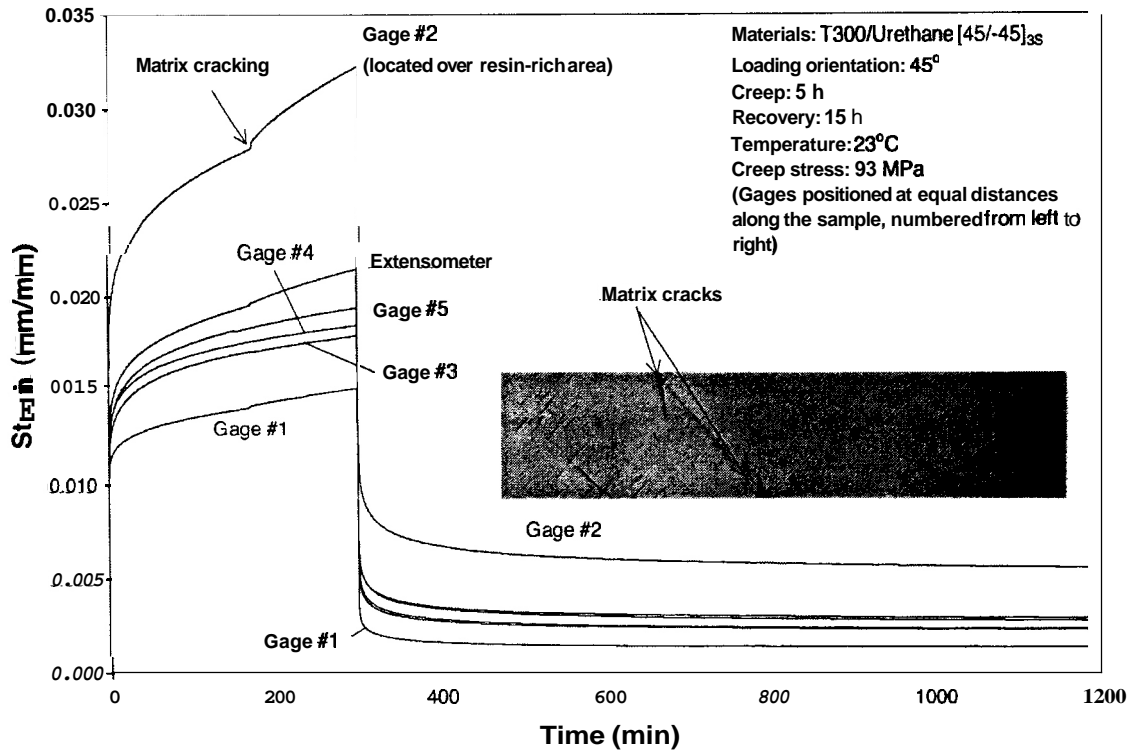


Fig. 27. Creep and recovery data collected on a multigaged $[\pm 45]_{3S}$ coupon exhibiting nonuniform deformation within a test specimen.

4.1.3 Additional Tests

Further tests included the X-ray photographic inspection of damage within test samples at increasing levels of applied stress, such as shown in Figs. 28 and 29, and the effect of coupon width on the stress-strain-to-failure response. As may be expected, in the latter case (which is not

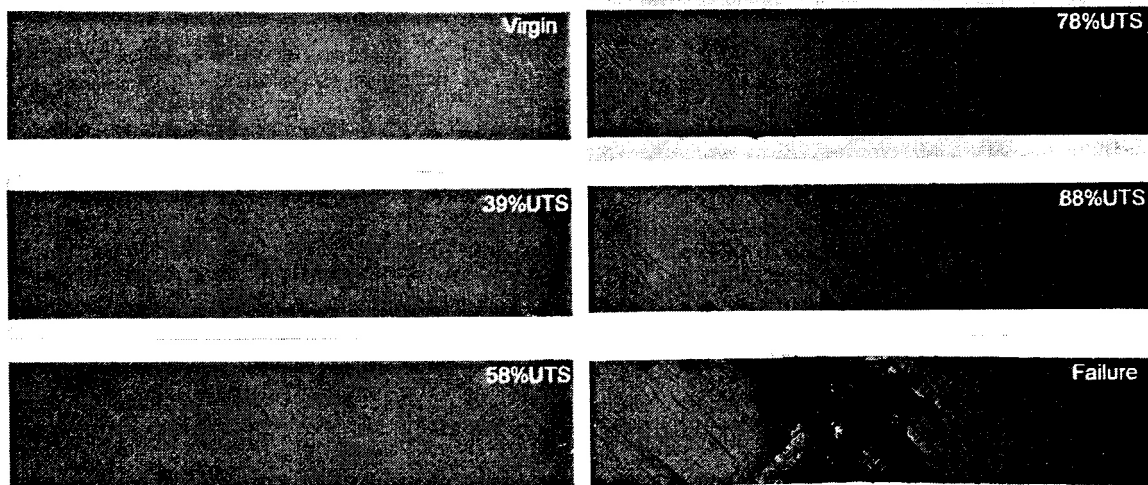


Fig. 28. X-ray images showing damage in $[\pm 45]_{3S}$ composite ($\phi = 45^\circ$) at various stress levels (in %UTS, UTS = 155 MPa).

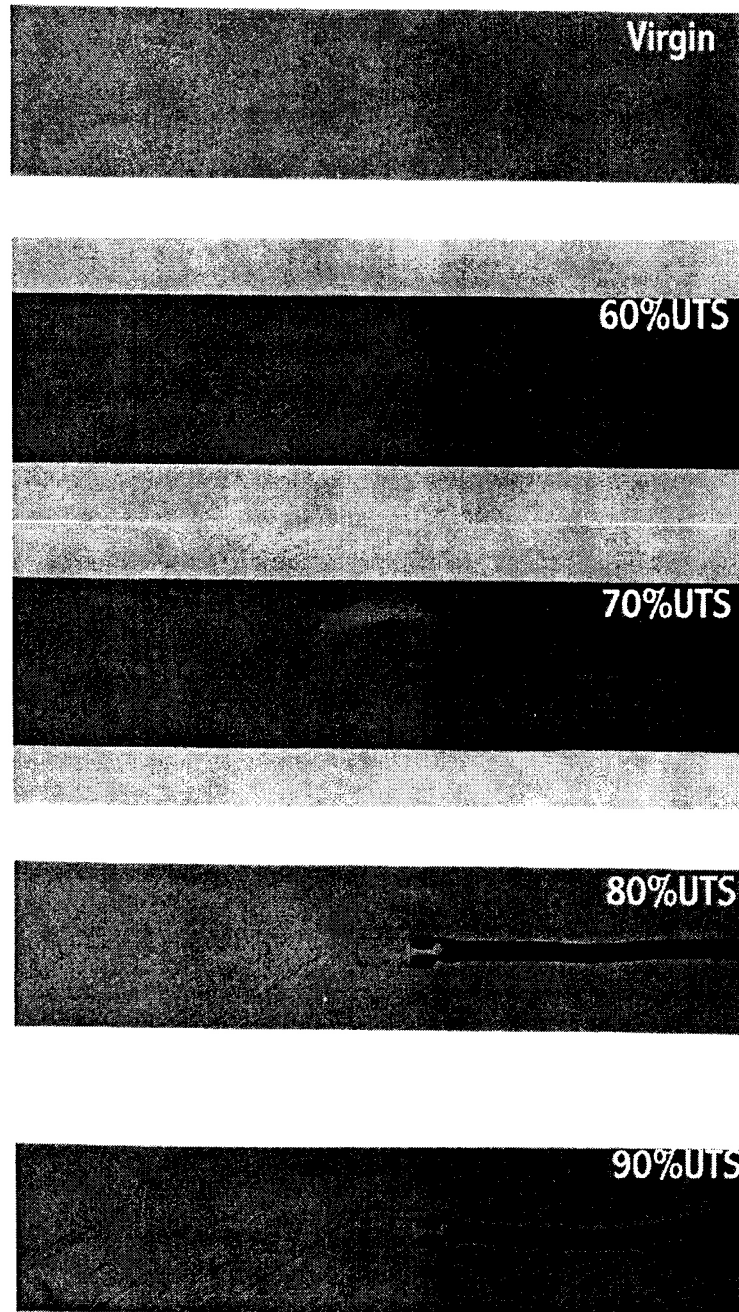


Fig. 29. X-ray images showing damage after creep loading in $[45/-45]_{3S}$ composite ($\phi = 30^\circ$) at various stress levels (in %UTS).

shown here) the foregoing response became stiffer with increasing coupon width because of the larger confinement provided by the wider tabs.

4.2 DATA REDUCTION

4.2.1 Creep and Recovery

The extensive data base for creep and recovery strains, listed in Table 3, could be expressed empirically as a sum, $E = \epsilon_v + \epsilon_p$, of a fully recoverable viscoelastic component ϵ_v and a permanent component ϵ_p . The viscoelastic component could be related in power-law form, namely

$$E, = (D_0 + D_1 t^n) \sigma_0 ; \quad (17)$$

most generally, $\epsilon_i = f(\sigma_0, t, T, \phi)$, where t refers to time under load. Also, it may be anticipated that D_0, D_1 , and perhaps also n , vary with σ_0, T , and ϕ .

Typical results, confined to $\phi = 45^\circ$, are exhibited in Figs. 30–33. These and similar results for other angles ϕ , which are depicted in Figs. 34–36, yield the following empirical expression for the permanent strain ϵ_p :

$$\epsilon_p = A(t/t_1)^{0.22} \exp[13.32(T/T_R) + 24.2(\sigma/\sigma_R)]F(\theta) , \quad (18)$$

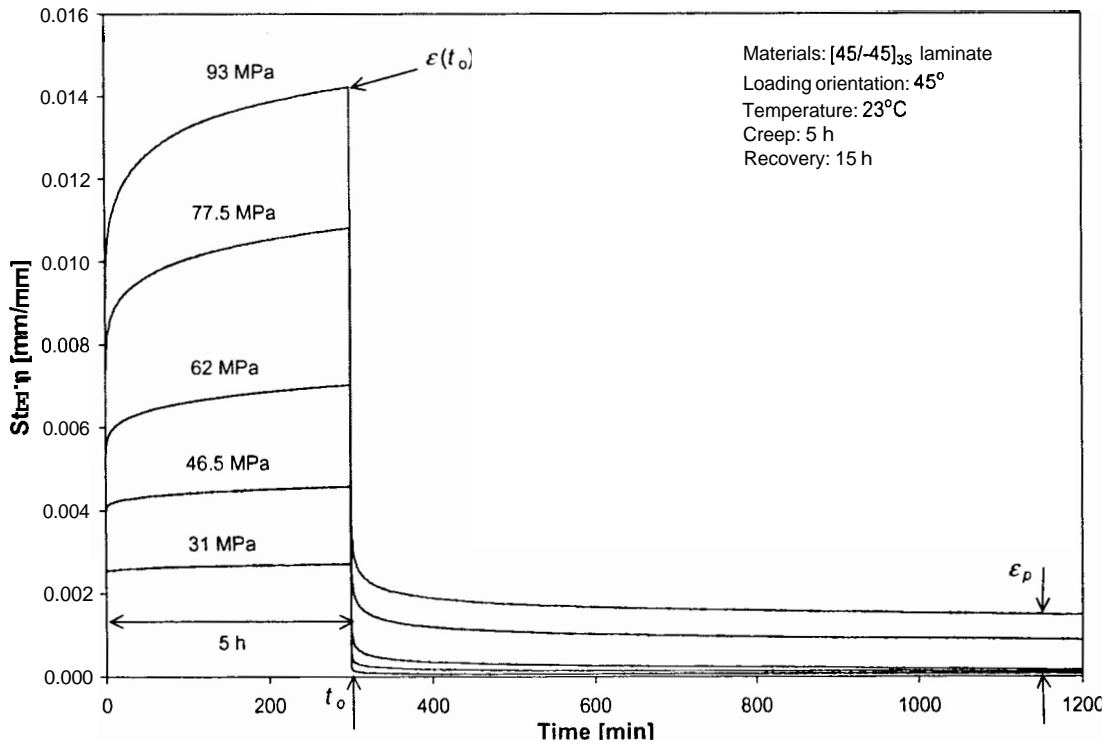


Fig. 30. Typical creep and recovery curves of $[\pm 45]_{3S}$ laminate coupons ($\phi = 45^\circ$) at 23°C under various stress levels.

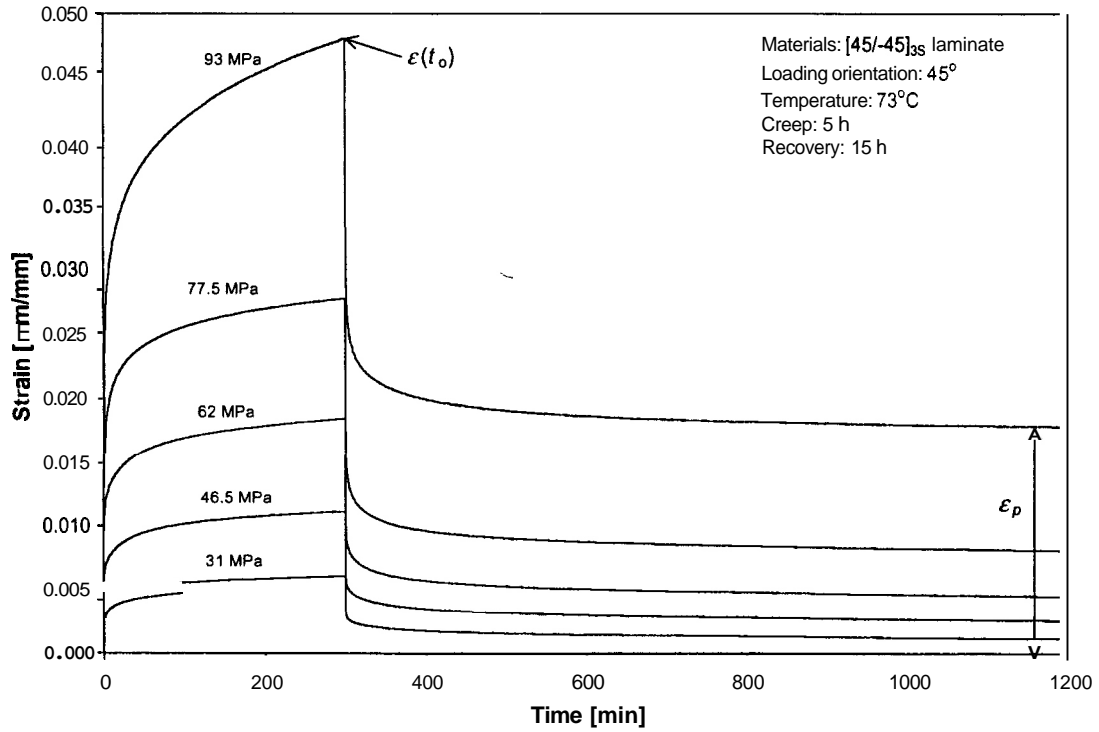


Fig. 31. Typical creep and recovery curves of $[\pm 45]_{3S}$ laminate coupons ($\phi = 45^\circ$) at 73°C under various stress levels.

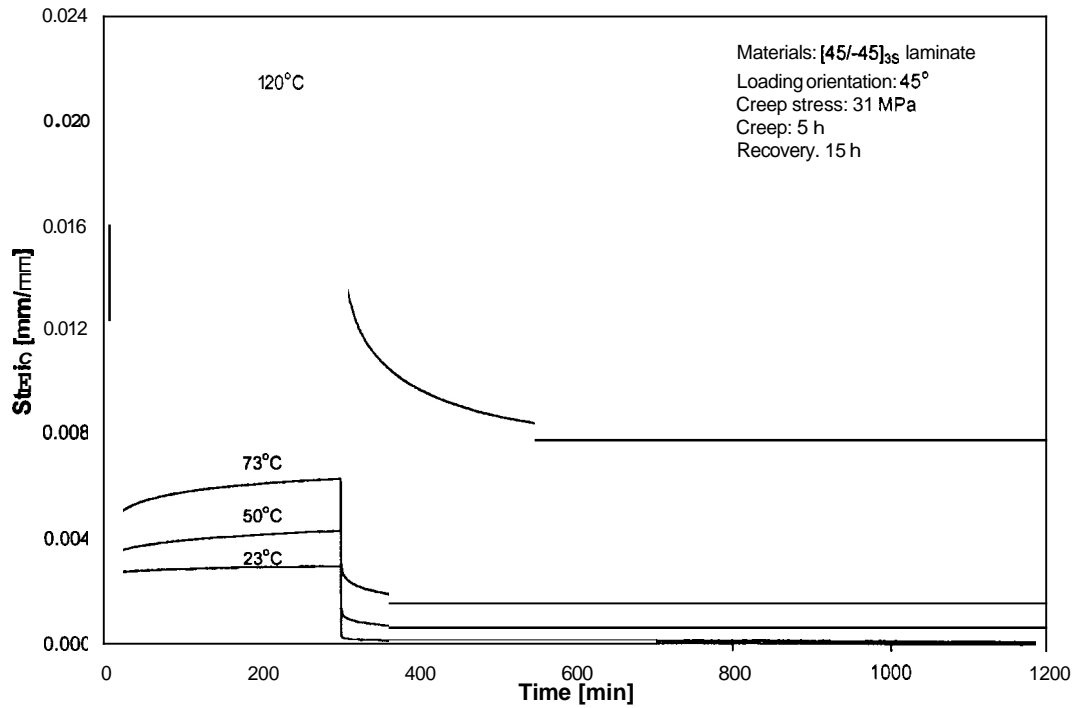


Fig. 32. Comparison of the typical creep-recovery curves under the same stress level 31 MPa at different temperatures, showing the effect of temperature on the creep deformation.

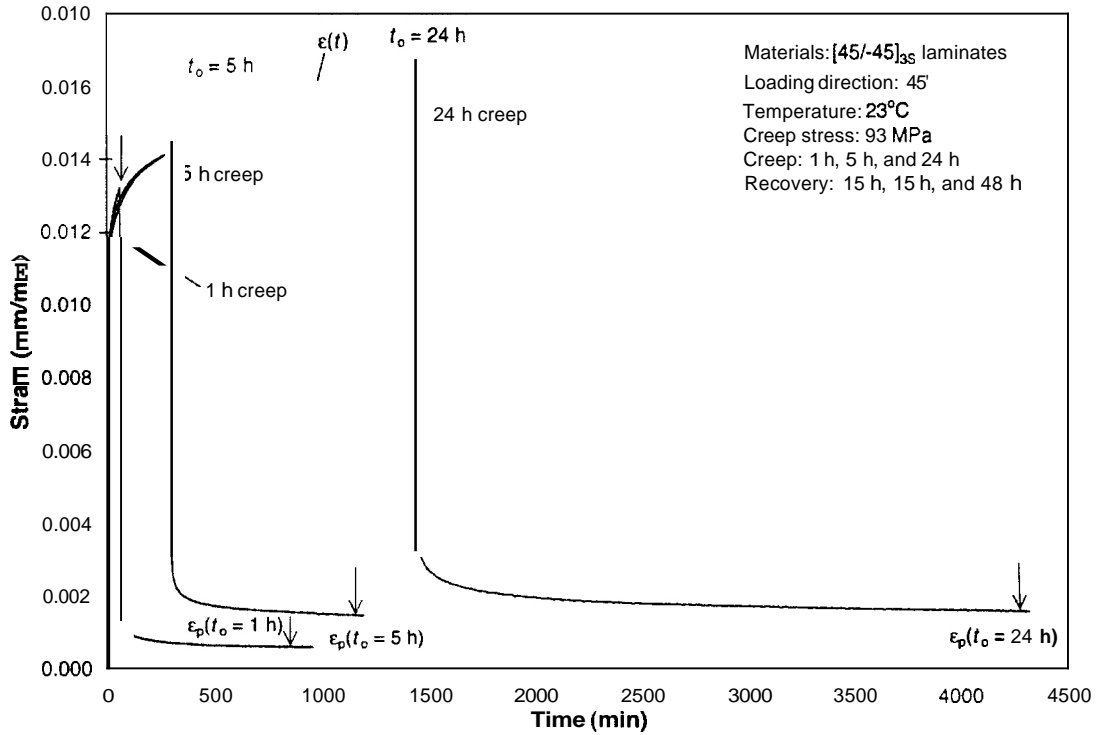


Fig. 33. Comparison of the creep and recovery curves under different creep durations, showing the influence of creep time on the permanent deformation.

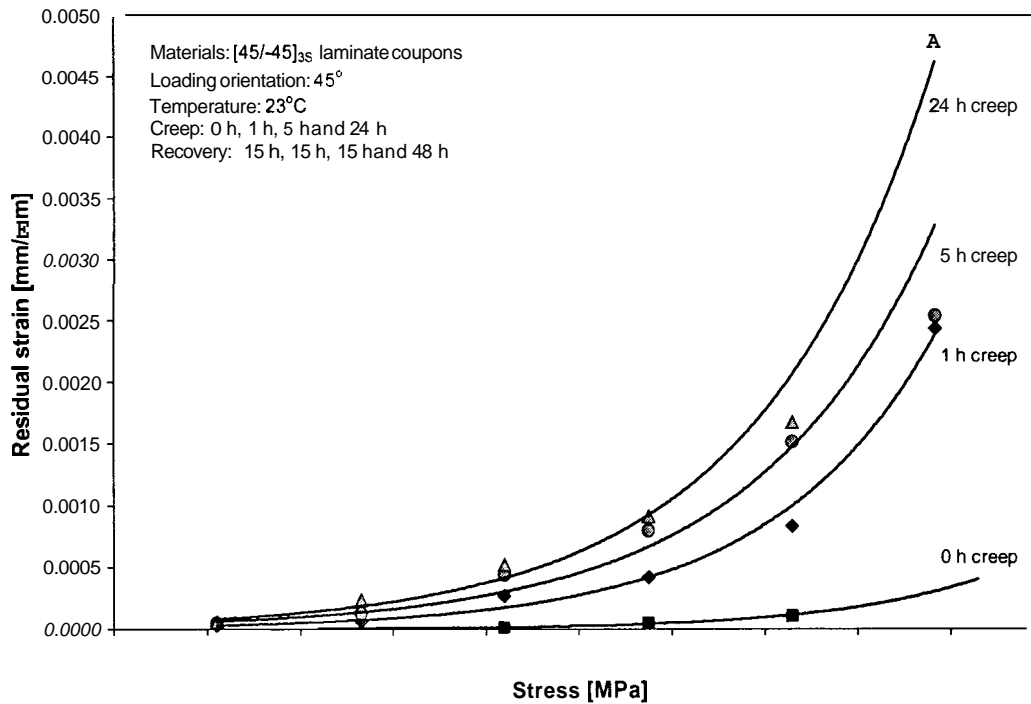


Fig. 34. Plot of permanent residual strain vs applied stress for 45° coupons at 23°C with different creep durations, showing the influence of stress and creep time on the permanent deformation.

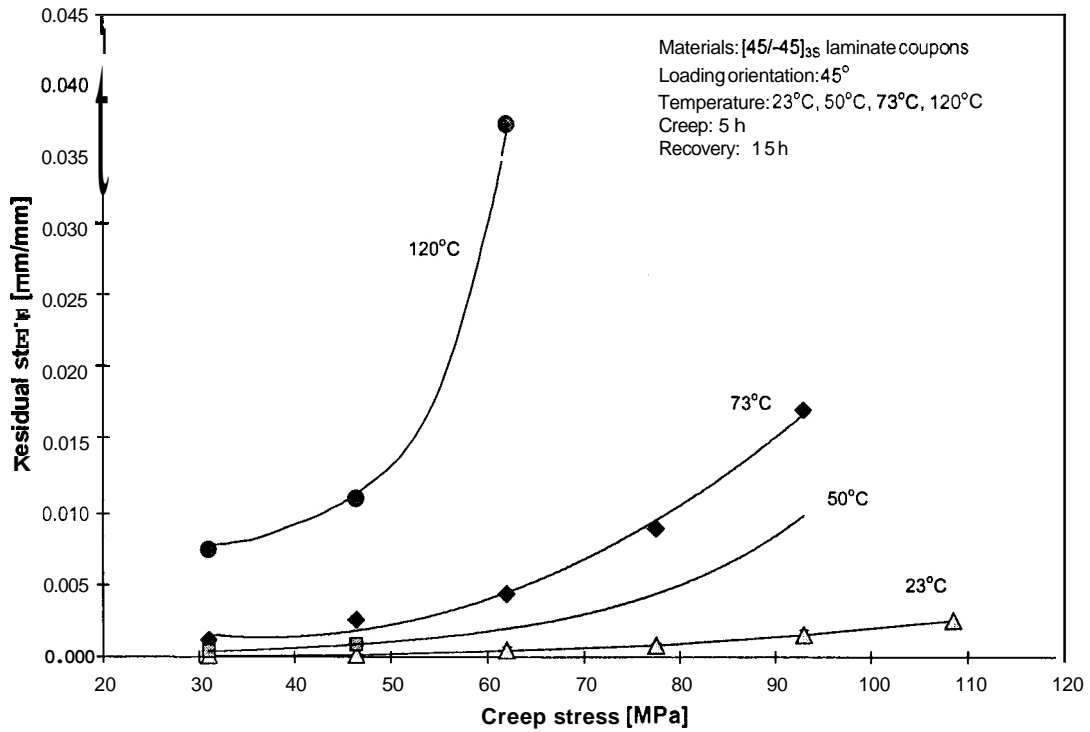


Fig. 35. Plot of permanent residual strain vs applied stress for 45° coupons at different temperatures, showing the influence of stress and temperature on the permanent deformation.

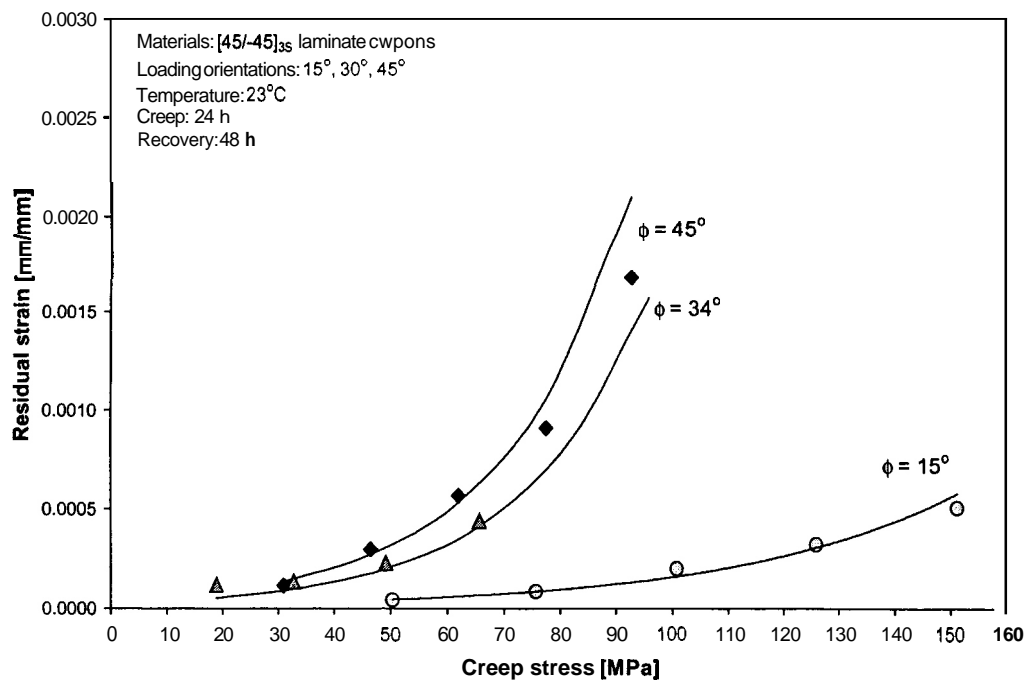


Fig. 36. Plot of permanent residual strain vs applied stress for test coupons with three orientation angles, showing the influence of loading orientation on the permanent deformation.

where

$$F(\theta) = 1.1643 \cdot \left(1 - \frac{|\theta|}{45}\right) + 1.3257 \cdot \left[1 - \left(\frac{\theta}{45}\right)^2\right] - 1.49 \cdot \left(1 - \frac{|\theta|}{45}\right)^3 \quad (19)$$

In the above, $\theta = 45^\circ - \phi$ (indegrees), where ϕ is the orientation angle. Also t is time in minutes, σ is the creep stress in megapascals, T is temperature in degrees Kelvin, A is a dimensionless constant $= -3 \times 10^{-11}$, $t_1 = 60$ min, $T_R = 296^\circ\text{K}$, and $\sigma_R = 550$ MPa, which is the tensile strength of the 0° specimen at 23°C . Accordingly, the recovery strain is given by

$$\epsilon_r = D_1 [t^n - (t - t_0)^n] \sigma_0 + \epsilon_p(t_0, T, \sigma_0, \phi), \quad t > t_0 \quad (20)$$

Note that, by hypothesis, no further permanent deformation occurs after load removal at time t_0 .

The essential role of ϵ_p in the fitting of creep and recovery data is exhibited in Fig. 37. Restricting attention to 5-h creep data for $[\pm 45^\circ]_{3S}$ coupons, followed by 24-h recovery, it was possible to fit the stress and temperature dependence of the power-law parameters by the following expressions, upon using averaged values for the creep parameters:

$$\epsilon = \{D_0 + D_1 [t \cdot a(T)]^n\} \sigma_0 + \epsilon_p \quad (21)$$

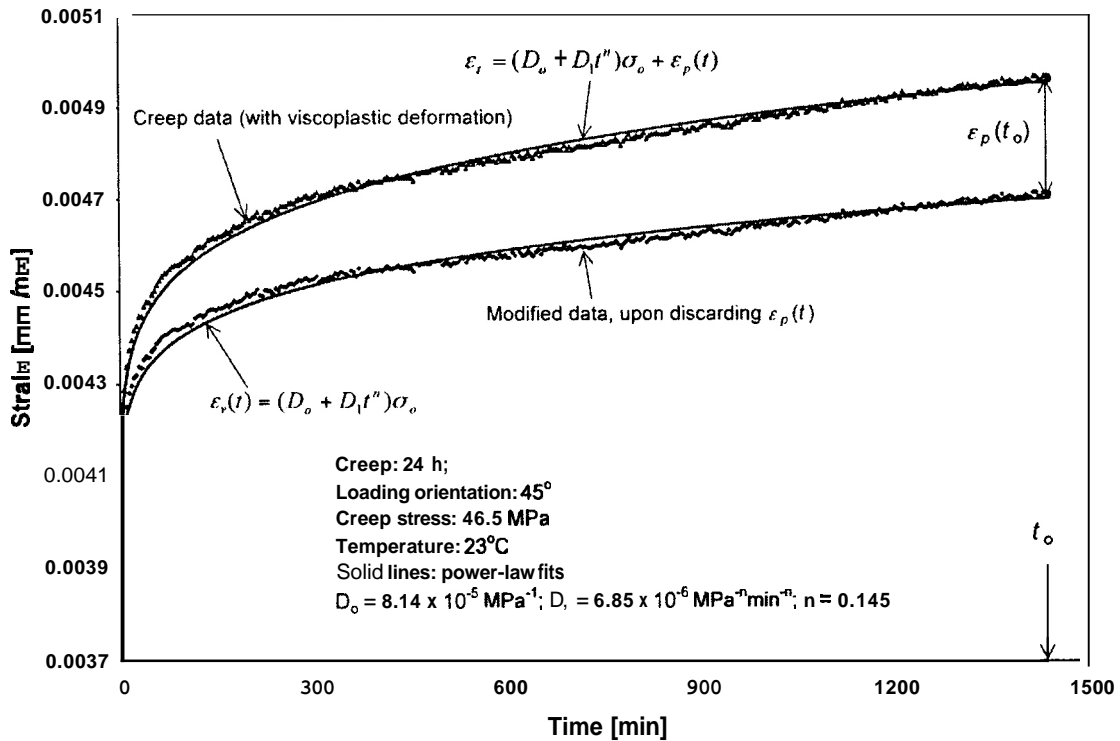


Fig. 37. Typical creep data (upper plot) and the modified viscoelastic portion (lower plot). Comparisons with power-law prediction are shown by the solid lines ($\phi = 45^\circ$, 24-h creep, 23°C).

where $n = 0.25$, $D_0 = D_0(T) = (7.02 + 0.05037) \times 10^{-5} \text{ MPa}^{-1}$ (T in $^{\circ}\text{C}$, $23^{\circ}\text{C} < T < 73^{\circ}\text{C}$), $D_1 = [1.61 + 0.05713(\sigma - 31)H(\sigma - 31)] \times 10^{-6} \text{ MPa}^{-n} \text{ min}^{-n}$ and the "shift factor," $a(T) = \exp[74(1 - T_R/T)]$ (T in $^{\circ}\text{K}$). Here $H(\cdot)$ denotes the unit step function.

An example for the utilization of Eq. (21) in fitting the elevated modified temperature data is shown in Fig. 38.

It must be emphasized that in view of the aforementioned substantial sample-to-sample variations, all the above parametric values, including those listed in Eq. (18), are scattered by about 10–15% around their averages.

4.2.2 Long-Term Representation of Creep Data

As noted previously, the values of the power-law parameters and their dependence on stress and temperature were based on 5-h creep data. It turned out that, to obtain optimal fits for either longer or shorter creep times, it was necessary to employ different values of D_0 , D_1 , and n . Specifically, D_1 had to be increased, while n needed to be decreased, with creep time t_0 (see Tables A.1 and A.2 in Appendix A). This observation pointed out the inadequacy of the three-parameter power law in serving as a model to predict the time-dependent response of the composite under consideration. For example, consider the data for 24-h creep time followed by an additional 48-h recovery period shown in Fig. 39. The optimal power law parameters, determined so as to fit the first 5-h creep data alone, yielded increasing overestimates of subsequent creep and recovery data, as shown in Fig. 39 for the overall data. Conversely, employment of the 24-h power-law parameters provided an improved match against data as shown in Fig. 40. It was thus attempted to fit the creep and recovery data by means of a Prony series, namely

$$\varepsilon_v = A_0 + \sum_{i=1}^n A_i (1 - e^{-t/\tau_i}), \quad (22)$$

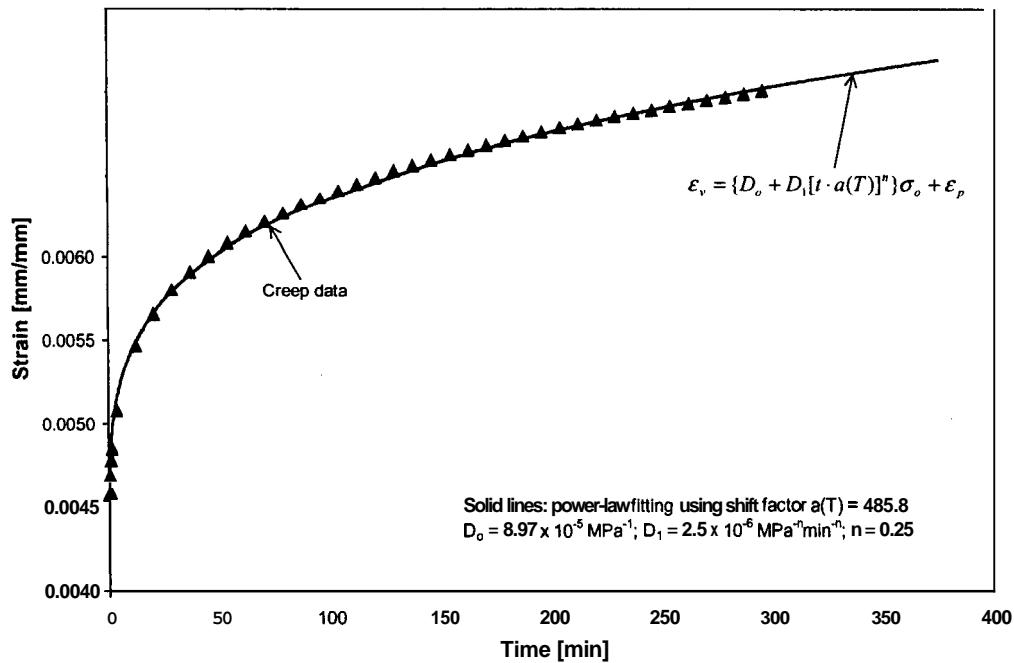
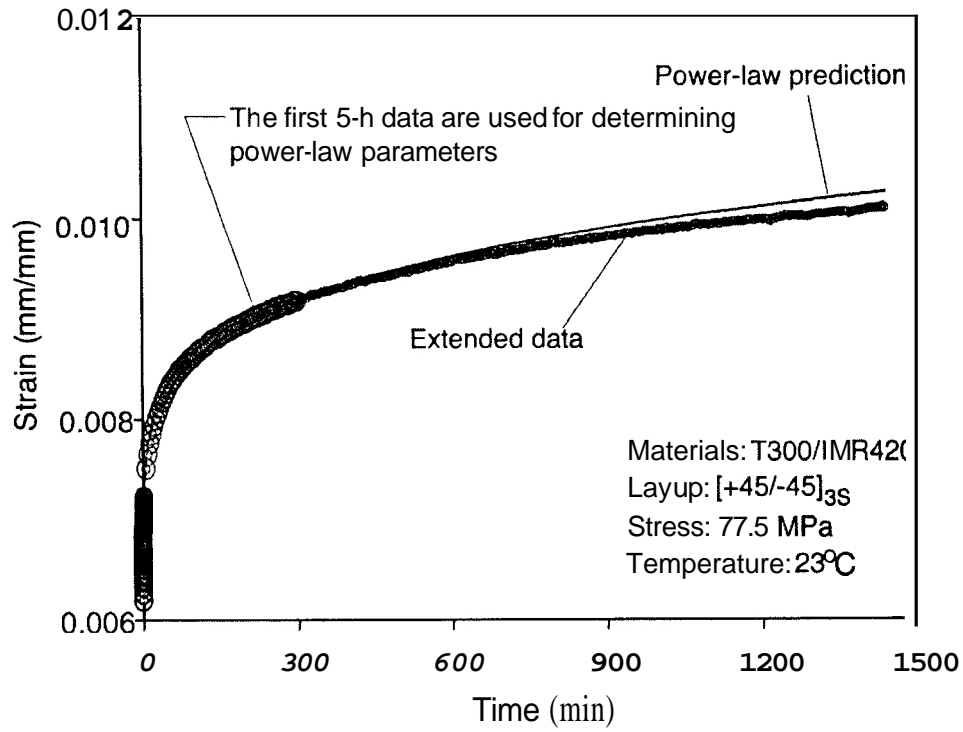
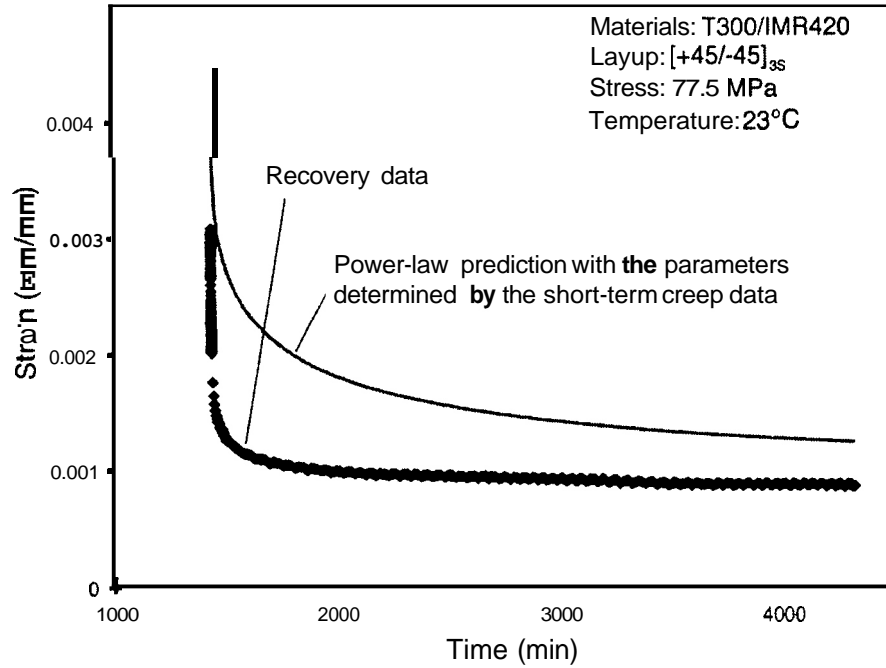


Fig. 38. Typical creep data and the power-law prediction with shift factor ($\phi = 45^{\circ}$, 5-h creep, 50°C).



(a)



(b)

Fig. 39. Creep and recovery data and corresponding power-law fits: (a) creep, (b) recovery.

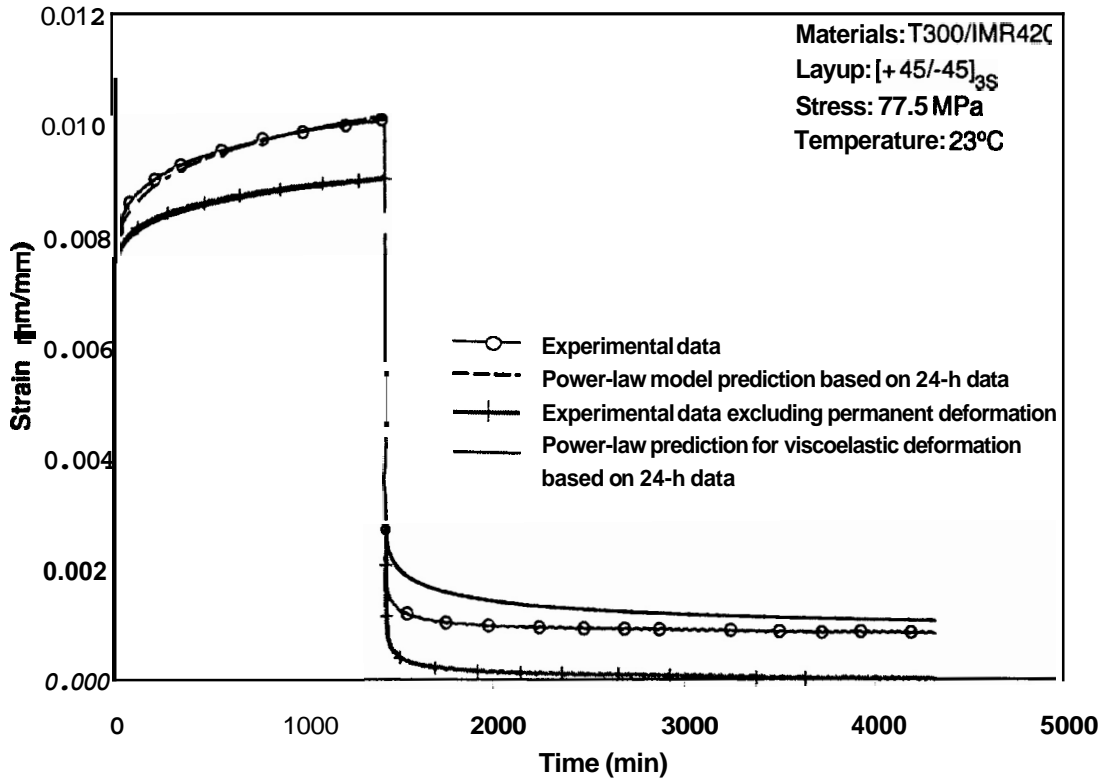


Fig. 40. Experimental creep and recovery data and modified power-law fits.

which contains a larger number of independent parameters. The above representation, which involves $n + 1$ amplitudes A_i ($i = 0, \dots, n$) and n retardation times τ_i ($i = 1, \dots, n$), can be rewritten as

$$\{\varepsilon_v\} = A_0 + [D]_{MN} \{A\}_N, \quad (23)$$

where $D_{kL} = 1 - \exp(-t_k/\tau_L)$.

Obviously, $A_0 = \varepsilon_v(0)$. Thus, M data points, corresponding to times $t = t_k$ are to be matched against $2n$ parameters A_i and τ_i . For attaining the best fit, it is necessary to have $M > 2n$.

The "linear" parameters A_i may be determined by correlating Eqs. (22) and (23) with experimental data, once the "nonlinear" parameters τ_i are known. This can be achieved by employment of the Gauss elimination procedure and optimal regression in the sense of least-square error. An overdetermined system $M > 2n$ generates smoother data-fitting curves. Subsequently, the determination of the parameters τ_i was achieved by an iterative, nonlinear optimization scheme for the least-square error. A similar approach is outlined elsewhere.*

Starting with assumed initial values of the nonlinear parameters τ_i , the data on the left side of Eq. (23) is utilized to solve for a concurrent set of values of A_i . With this set of A_i , the resulting error in the fit serves to guide the adjustment of τ_i for the next iteration. This procedure is repeated utilizing nonlinear least-square methods, such as the steepest descent technique, until convergence is achieved to within a prescribed tolerance.* A flow chart of the optimization scheme is shown in Appendix B, with the corresponding least-square errors listed in Table 4.

*This tolerance is related to observed, inevitable fluctuations in the recorded data.

Table 4. Least-square error in correspondence to number of exponential parameters

i	3	4	5	6	7	8
$\Delta(\times 10^{-6} \text{ mm/mm})$	0.9210	0.4110	0.2437	0.3450	0.2215	0.2183

Though not detailed here, data fits with $i \geq 4$ were indistinguishable from each other. Consequently, it was decided that $i = 4$ presented the “best” choice. The corresponding Prony series parameters are listed in Table 5.

Obviously, the nine-parameter Prony series generated here provided a better fit with the creep data at hand. More significantly, this representation *predicts* the creep and recovery behavior rather accurately for durations that extend beyond the time ranges employed for fitting the creep data. This is shown in Fig. 41, where the permanent component of strain ϵ_p was deleted for clarity. This good agreement between data and model presents an improvement over the result shown in Fig. 39.

It is possible to employ the empirical Eq. (21) to incorporate the effects of stress and temperature within the Prony series in Eq. (22). Accordingly, $A_o(T)$ should vary like $D_o(T)$; all A_i should have the same, common, dependence on σ as $D_1(\sigma)$; and all τ_i are to be decreased by a common shift factor function $a(T)$.

Table 5. Prony series parameters of fit to the early 5-h creep data in Fig. 20(a) ($A_o = 0.0063 \text{ mm/mm}$)

I	A_i	τ_i
1	0.0004	0.0021
2	0.0008	1.0956
3	0.0007	47.3746
4	0.0011	351.7997

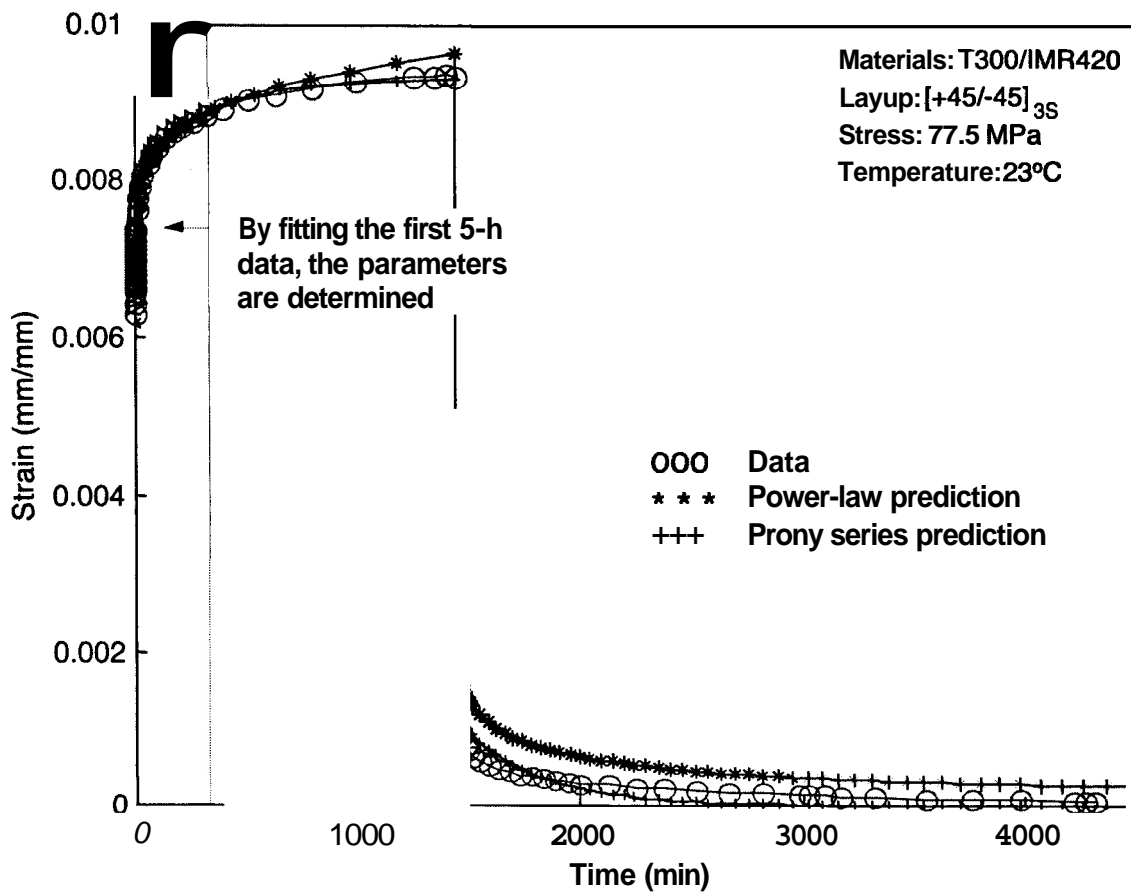


Fig. 41. Comparison of the predictions (Prony series and power-law models) to experimental creep and recovery data. Permanent deformation is excluded.

5. PREDICTIONS FOR CROSSPLY BEHAVIOR

5.1 EFFECT OF LOAD ORIENTATION ANGLE ON CREEP

Inversion of Eq. (8), for $\phi = \pm 45^\circ$, gives

$$\varepsilon_x = + \left(\frac{4}{4 Q_{11} + Q_{22} + 2Q_{12}} + \frac{1}{Q_{66}} \right) \sigma_x . \quad (24)$$

In Eq. (24), only Q_{22} and Q_{66} incorporate the properties of the matrix phase to a significant degree and are thereby time dependent. However, as noted earlier, for balanced crossply layouts Q_{22} always appears in combination with Q_{11} , in the form of $Q_{11} + Q_{22}$. Furthermore, as shown in Sect. 3.6, Q_{11} exceeds Q_{22} by 2 orders of magnitude. Thus, it is possible to neglect the time-dependent variation of Q_{22} and attribute all creep to the temporal dependence of Q_{66} . Denote

$$Q_{66} = Q_{66}(t) = Q_{66}(0) + \Delta Q_{66}(t) . \quad (25)$$

Comparison of Eqs. (24) and (25) with the power-law expression (17) yields

$$D_o = \frac{1}{4} \left(\frac{4}{Q_{11} + Q_{22} + 2Q_{12}} + \frac{1}{Q_{66}(0)} \right) , \quad (26)$$

where all the foregoing values of Q_{ij} , including $Q_{66}(0)$, are given in Sect. 3.5.2. Consequently,

$$\frac{1}{Q_{66}(t)} = \frac{1}{Q_{66}(0)} + 4D_1 t^n = \frac{1}{Q_{66}(0)} + \left(\frac{4}{Q_{11} + Q_{22} + 2Q_{12}} + \frac{1}{Q_{66}(0)} \right) \frac{D_1 t^n}{D_o} . \quad (27)$$

Substitution of Eq. (27) into Eq. (9) indicated that v_{xy}^{45} decreases but slightly with time. Though not shown here, this result was confirmed experimentally.

With $Q_{66}(t)$ thus determined, the longitudinal creep strain $\varepsilon_x(t)$ of any $[\phi/(\phi + \pi/2)]_S$ crossply layup orientated by an angle ϕ about the direction of the uniaxially applied step stress σ_o , can be calculated using the inverses of Eq. (6). Computations were performed within the linear range of viscoelastic behavior and in the absence of permanent deformation.

Direct substitution of numerical values for $\phi = 15^\circ$ and 34° into Eqs. (5) and (6) resulted in the predictive curves for $\varepsilon(t)$ shown in Figs. 42 and 43. These predictions, which employed the average power-law parameters, $D_o = 8.13 \times 10^{-5} \text{ MPa}^{-1}$, $D_1 = 2.49 \times 10^{-6} \text{ MPa}^{-n} \text{ min}^{-n}$, and $n = 0.238$, were compared against several replicate data sets.

Note the very good agreement between predicted and recorded creep behavior exhibited in those figures. Inverting Eq. (10) one obtains

$$\varepsilon_x = \frac{2(Q_{11} + Q_{22})}{(Q_{11} + Q_{22})^2 - 4Q_{12}^2} \sigma_x , \quad (28)$$

whereby all creep, if any, is due to the time dependence of Q_{22} . In view of Sect. 3.6, such dependence would cause ε_x to increase by about 0.4% above its initial value over time. Indeed, the creep and recovery data shown in Fig. 44 demonstrate the presence of the indiscernible amount of creep at 0° orientation even at the relatively high stress levels of 168 and 350 MPa.

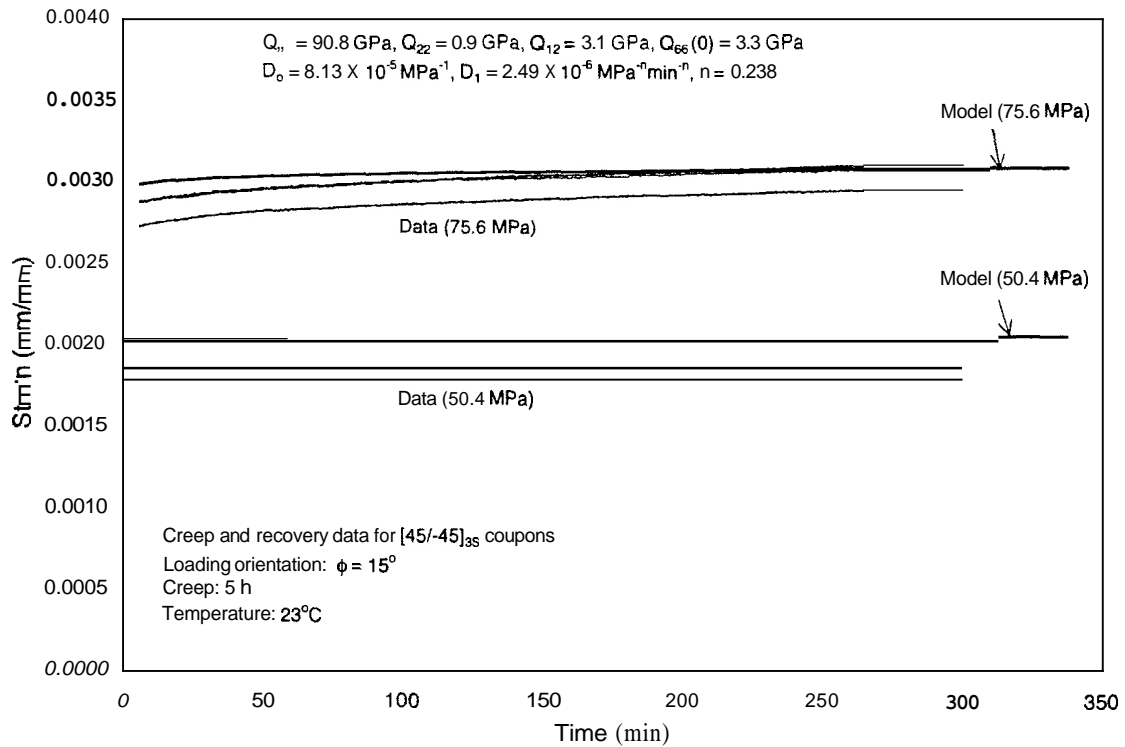


Fig. 42. Comparison of creep data from three replicate specimens with theoretical predictions for stress-strain response within the linear range ($\phi = 15^\circ$, 5-h creep, 23°C).

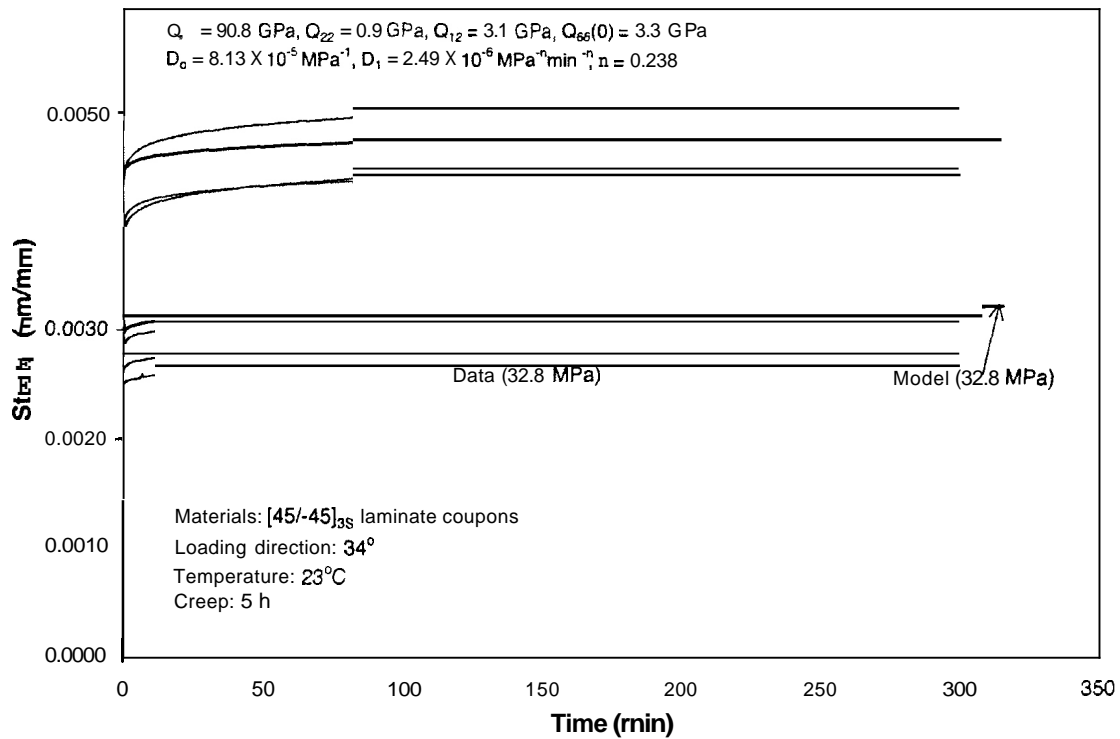


Fig. 43. Comparison of creep data from three replicate specimens with theoretical predictions for stress-strain response within the linear range ($\phi = 34^\circ$, 5-h creep, 23°C).

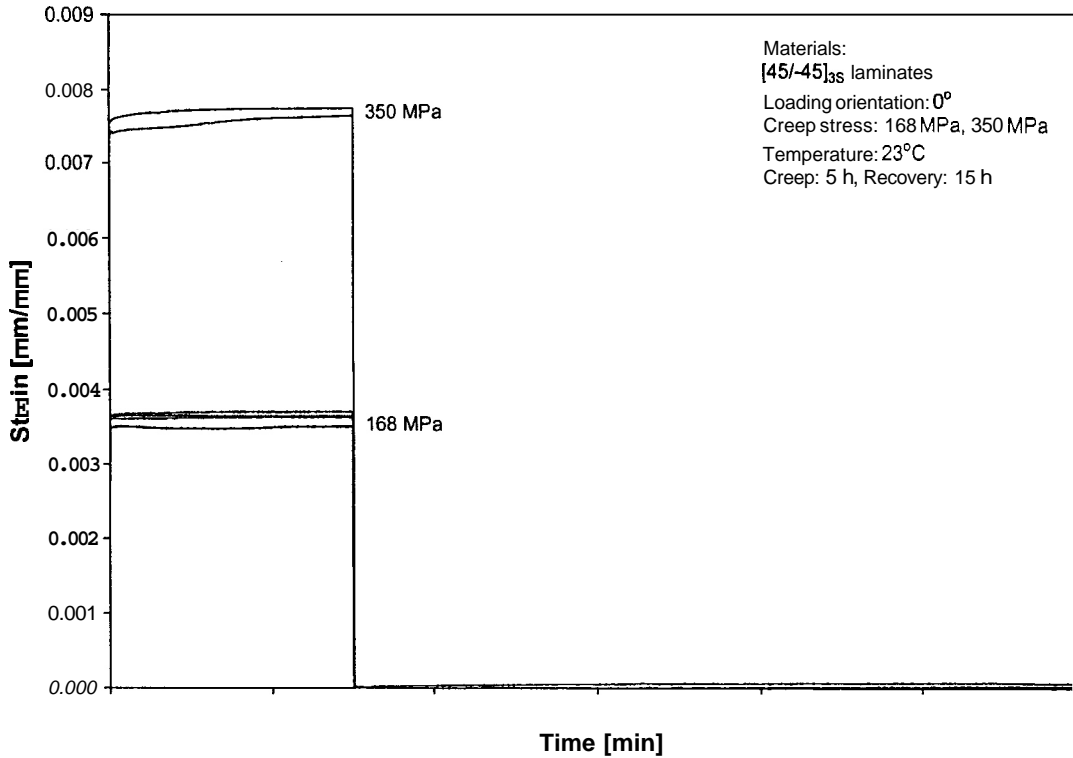


Fig. 44. Creep and recovery data of 0° coupons under stress levels of 168 MPa and 350 MPa ($\phi = 0^\circ$, 5-h creep, 15-h recovery, 23°C).

5.2 CREEP UNDER TWO-STEP STRESS INPUT

In view of the wide scatter in the response of the composite material at hand, which increases with stress level as shown in Figs. 25 and 26, it is extremely difficult to predict its behavior under complex inputs in the elevated range of stresses. However, for a limited range of nonlinearity, namely, in the absence of internal damage and permanent deformation, such predictions may still be feasible. For this purpose, consider the case of a two-step stress history applied to a $[\pm 45^\circ]_{3S}$ sample:

$$\begin{aligned}\sigma &= \sigma_o[H(t) - H(t - t_o)] + \sigma_1[H(t - t_o) - H(t - t_1)] \\ &= \sigma_o[H(t) - H(t - t_1)] + (\sigma_1 - \sigma_o)[H(t - t_o) - H(t - t_1)] ,\end{aligned}\tag{29}$$

where, as before, $H(\cdot)$ denotes the unit step function.

The following specific values were employed in the test program: $\sigma_o = 31$ MPa, $\sigma_1 = 46.5$ MPa, $t_o = 300$ min, and $t_1 = 600$ min. The above stress history is shown by the dashed line in Fig. 45.

Consider the power-law representation given in Eq. (17). As can be noted from Tables A.1 and A.2, to attain "best" data fits it is necessary to vary the creep parameters D_o , D_1 , and n with the stress level σ . Specifically, for $\sigma = 31$ MPa, one may employ $D_o = 7.85 \times 10^{-5} \text{ MPa}^{-1}$, $D_1 = 2.49 \times 10^{-6} \text{ MPa}^{-n} \text{ min}^{-n}$, and $n = 0.238$; for $\sigma = 46.5$ MPa, the suitable parameters are $D_o = 8 \times$

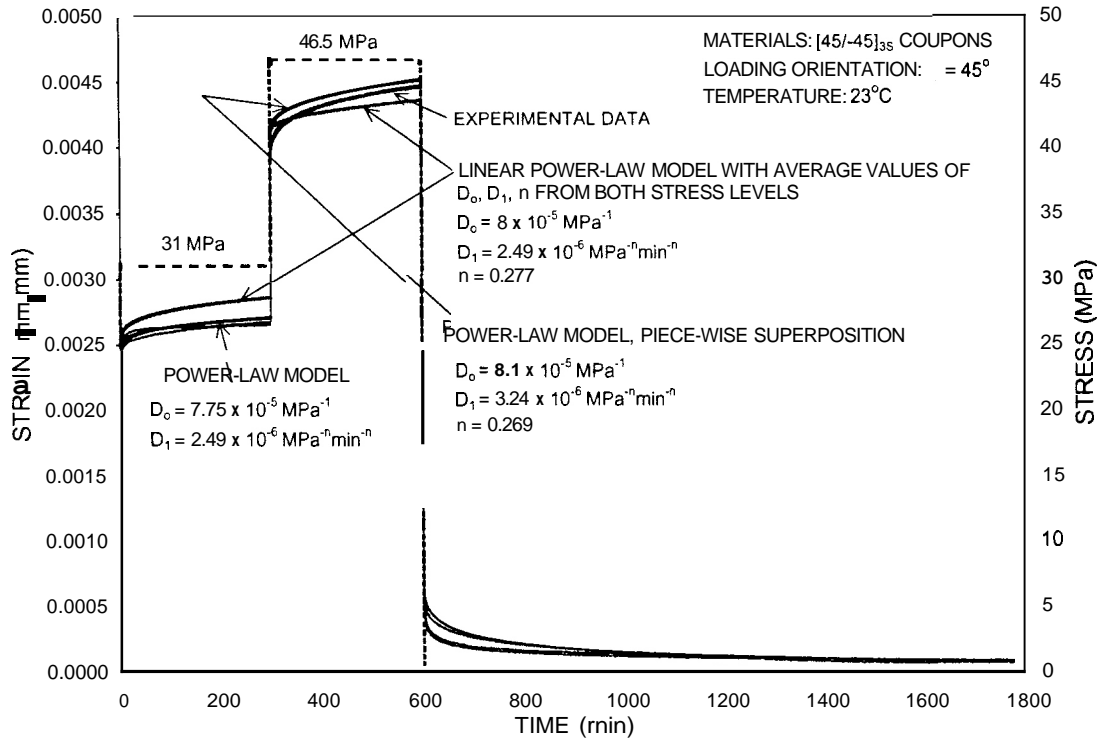


Fig. 45. Experimental data and model prediction under a two-step load history for $[\pm 45]_{3S}$ coupons at 23°C .

10^{-5} MPa^{-1} , $D_1 = 3.24 \times 10^{-6} \text{ MPa}^{-n} \text{ min}^{-n}$, and $n = 0.269$. (The average numerical values of the above parameters are 7.93×10^{-5} , 2.87×10^{-6} , and 0.253, respectively.)

A good prediction for the creep and recovery under the above two-step stress history is obtained by superimposing the creep and recovery strains that are due to $\alpha(t) = \sigma_0[H(t) - H(t - t_0)]$ with values of D_0 , D_1 , and n that correspond to $\sigma_0 = 31 \text{ MPa}$ and the creep and recovery strains caused by $\alpha(t) = \sigma_1[H(t - t_0) - H(t - t_1)]$ with values of D_0 , D_1 , and n associated with $\sigma_1 = 46.5 \text{ MPa}$. This "piecewise superposition" that employs stress-varying creep parameters,⁹ provides a far better agreement with creep data than linear superposition employing average values of creep parameters D_0 , D_1 , and n . Results are shown in Fig. 45.

6. THE TIME-DEPENDENT AND NONLINEAR RESPONSE OF QUASI-ISOTROPIC LAYUPS

6.1 MATERIALS AND TESTING PROGRAM

The quasi-isotropic test coupons were cut at different angles, ϕ , relative to the fiber direction in the top ply, as shown in Fig. 46.*

Tensile tests were again conducted using an 810MTS Material Testing System with a loading rate of 1.016mm/min at four different temperatures (23°C, 50°C, 73°C, and 120°C). An axial extensometer and several strain gages were used for recording the strains in both the longitudinal and transverse directions of the test coupons. At least three replicate specimens were tested for each case.

Additional test coupons, with the same features as mentioned previously, were employed to conduct creep and recovery tests. The short-term creep and recovery tests were performed on the 810MTS Material Testing System at various levels of fixed stresses under load control mode. One extensometer and several strain gages were attached to the surfaces of test coupons to record the deformation response during creep loading, followed by recovery on unloading. With one exception, all the foregoing tests involved 24 h of creep followed by 48 h of strain recovery. Tests were performed at three temperature levels (23°C, 73°C, and 120°C). Residual strain values at the end of the recovery period were considered to represent permanent deformation. The creep and recovery test program is listed in Table 6.

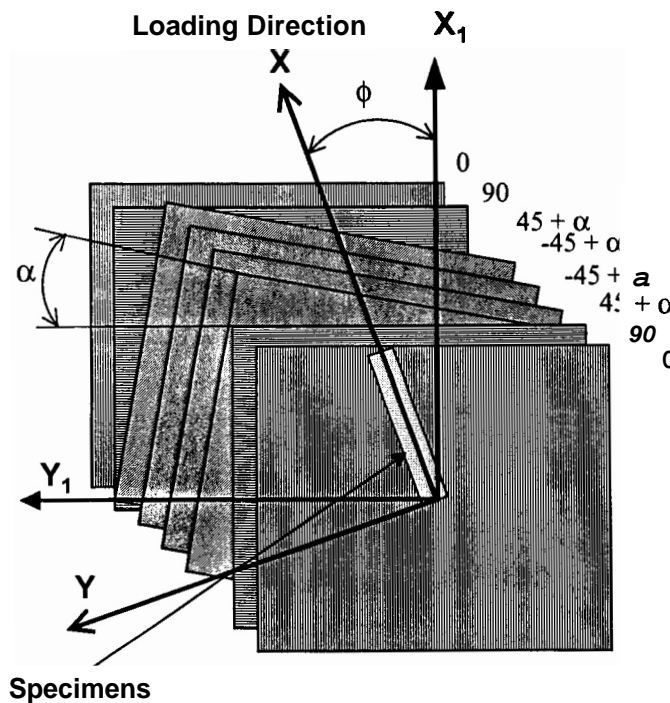


Fig. 46. Illustration of quasi-isotropic laminates with layup misalignment.

*In that figure, some ply groups are misaligned. The observable effects of such misalignment are discussed later.

Table 6. Creep and recovery test program

Creep stress σ_0 (MPa)	Creep/recovery times $t_0/(r-1)t_0$ (h)	Number of test specimens	Creep stress σ_0 (MPa)	Creep/recovery times $t_0/(r-1)t_0$ (h)	Number of test specimens
	$\phi = 0^\circ, T = 73^\circ\text{C}$			$\phi = 22.5^\circ, T = 73^\circ\text{C}$	
59.2	24/48	2	59.2	24/48	2
88.8	24/48	3	88.8	24/48	2
118.4	24/48	3	118.4	24/48	2
148	24/48	2	148	24/48	2
177.6	24/48	2	177.6	24/48	3
	$\phi = 0^\circ, T = 120^\circ\text{C}$			$\phi = 22.5^\circ, T = 120^\circ\text{C}$	
59.2	24/48	1	59.2	24/48	4
88.8	24/48	1	88.8	24/48	2
118.4	24/48	1	118.4	24/48	4
148	24/48	1	148	24/48	4
148	72/48	1	177.6	24/48	2
177.6	24/48	1			
	$\phi = 0^\circ, T = 23^\circ\text{C}$			$\phi = 90^\circ, T = 23^\circ\text{C}$	
118.4	24/48	1	118.4	24/48	1
	$\phi = 45^\circ, T = 23^\circ\text{C}$		148	24/48	1
177.6	24/48	1			
	$\phi = 45^\circ, T = 73^\circ\text{C}$			$\phi = 90^\circ, T = 73^\circ\text{C}$	
59.2	24/48	2	59.2	24/48	2
			118.4	24/48	2
	$\phi = 67.5^\circ, T = 23^\circ\text{C}$		177.6	24/48	1
118.4	24/48	1			
	$\phi = 67.5^\circ, T = 73^\circ\text{C}$			$\phi = 90^\circ, T = 120^\circ\text{C}$	
148	24/48	2	177.6	24/48	1
177.6	24/48	2			

6.2 LINEAR RANGE OF LAMINATE RESPONSE

6.2.1 Tensile Properties of [0/90/45/-45]_S Laminates

With the foregoing properties at hand, it was possible to evaluate the longitudinal stiffness E , of the quasi-isotropic laminate under uniaxial tension. Recalling Eq. (6), one obtains expressions for the in-plane laminate stiffnesses given in Eq. (30), which include an imperfection angle α as shown in Fig. 46. For the quasi-isotropic laminate under consideration, $h_0 = 0.28$ mm, and the total number of plies is $n_p = 8$.

Obviously, for a perfect quasi-isotropic layup (i.e., with $\alpha = 0$), E , should not depend on load orientation. Nevertheless, actual room temperature experimental data, which are listed in Table 7 and depicted in Fig. 47, indicate the presence of angular dependence in E , even within the linear range of stress-strain response. This departure from quasi-isotropy can be traced to reported layup misalignments during the manufacturing process, when adjacent, stitched crossply pairs could not be stacked precisely at $\pm 45^\circ$ to each other, as desired.

To assess the effect of such misalignments, consider the circumstance where the inner [$\pm 45^\circ$] ply groups were tilted by a common angle α about their proper directions during the

Table 7. Tensile data for quasi-isotropic composite coupons loaded at various orientations

Orientation angle (deg)	Temperature (°C)	Stiffness (GPa)	Tensile strength (MPa)	Failure strain (%)	Poisson's ratio
0	23	30.8 ± 0.7	306.0 ± 10.0	0.98 ± 0.05	0.305 ± 0.05
	50	29.8 ± 1.3	291.6 ± 43.5	0.94 ± 0.17	
	73	31.2 ± 1.5	284.6 ± 37.3	0.94 ± 0.18	
	120	26.7 ± 2.3	260.5 ± 44.9	0.98 ± 0.12	
15	23	28.9 ± 0.5	239.5 ± 28.6	0.86 ± 0.11	0.355 ± 0.05
22.5	23	29.0 ± 2.7	254.5 ± 21.3	0.92 ± 0.10	
	50	32.1 ± 0.8	306.8 ± 4.6	0.91 ± 0.04	
	73	31.4 ± 1.2	273.5 ± 12.3	0.87 ± 0.11	
120	25.8 ± 4.1	218.1 ± 27.4	1.00 ± 0.14	0.393 ± 0.02	
30	23	26.9 ± 0.8	277.7 ± 5.0	1.09 ± 0.03	0.355 ± 0.05
45	23	32.2 ± 0.8	295.0 ± 15.9	0.92 ± 0.04	
67.5	23	29.9 ± 0.5	289.7 ± 23.7	1.01 ± 0.11	
	50	30.6 ± 0.1	298.8 ± 9.1	1.04 ± 0.02	
	73	27.5 ± 0.4	288.5 ± 2.1	1.02 ± 0.05	
	120	24.3 ± 0.3	205.2 ± 4.7	1.16 ± 0.2	
90	23	30.2 ± 1.0	294.1 ± 7.4	0.96 ± 0.03	0.355 ± 0.05
	50	30.7 ± 2.5	288.9 ± 5.4	0.92 ± 0.06	
	73	30.2 ± 0.5	303.0 ± 2.1	0.99 ± 0.03	

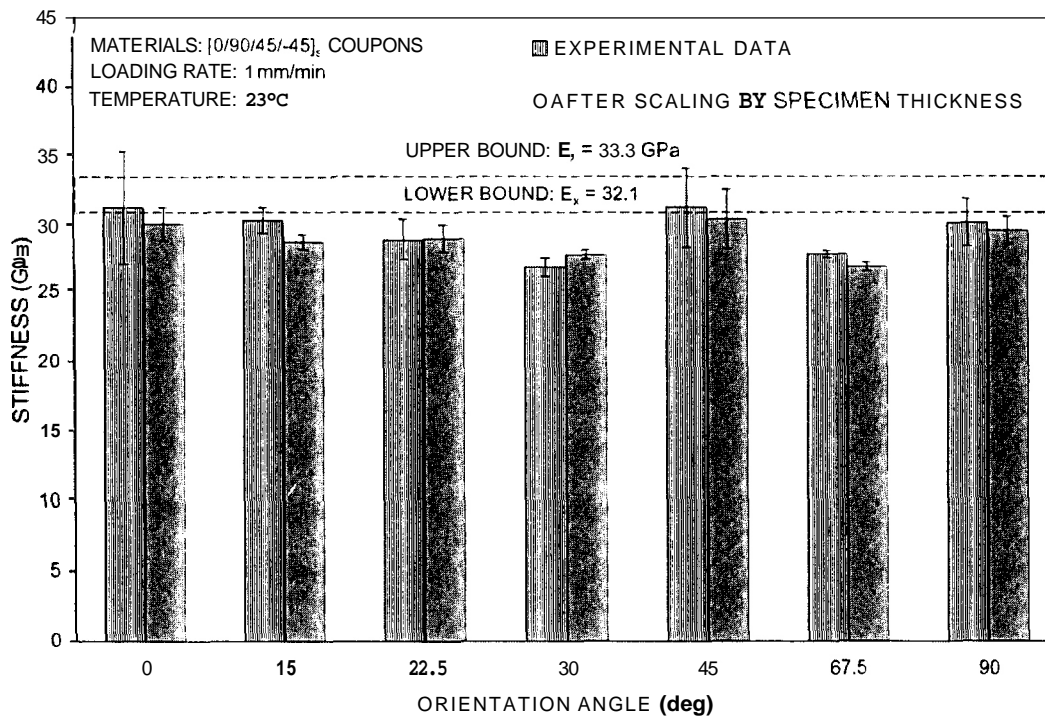


Fig. 47. Stiffness vs orientation angle of quasi-isotropic composite at 23°C. The dashed line denotes the values for ideal quasi-isotropic laminates, calculated according to laminate theory.

manufacturing process, as shown in Fig. 46. Straightforward manipulations of laminate equations¹⁰ yield the following expressions:

$$\begin{aligned}
 A_{11} = A_{22} &= 2h_o(Q_{11} + Q_{22})\left\{\cos^4 \phi + \sin^4 \phi + \frac{1}{2} + \frac{1}{2}\sin^2[2(\alpha + \phi)]\right\} + \\
 &\quad + 2h_o(Q_{12} + 2Q_{66})\{\sin^2(2\phi) + \cos^2[2(\alpha + \phi)]\}; \\
 A_{12} &= 2h_o(Q_{11} + Q_{22} - 4Q_{66})\frac{1}{2}\{\sin^2(2\phi) + \cos^2[2(\alpha + \phi)]\} + \\
 &\quad + 4h_oQ_{12}\left\{\cos^4 \phi + \sin^4 \phi + \frac{1}{2} + \frac{1}{2}\sin^2[2(\alpha + \phi)]\right\} \\
 A_{16} = -A_{26} &= 2h_o(Q_{11} - Q_{22} - 2Q_{12} - 4Q_{66})\frac{1}{4}\{\sin(4\phi) - \sin[4(\alpha + \phi)]\} \\
 A_{66} &= 2h_o(Q_{11} + Q_{22} - 2Q_{12})\frac{1}{2}\{\sin^2(2\phi) + \cos^2[2(\alpha + \phi)]\} + 4h_oQ_{66}\{\cos^2(2\phi) + \sin^2[2(\alpha + \phi)]\}.
 \end{aligned}
 \tag{30}$$

As noted in Sect. 3.5.2 and 3.6, the best estimates for the Q_{ij} values are $Q_{11} = 89.6$, $Q_{22} = 2.1$, $Q_{12} = 3.1$, and $Q_{66} = 3.3$ (all in GPa).

The resulting departure from quasi-isotropy can be evaluated by combining Eqs. (30) and (6). Results are depicted in Fig. 48, where E_x at different orientations ϕ is plotted vs the misalignment angle α , with α varying between 0° and 20° . It is evident that departures from quasi-isotropy increase with α .

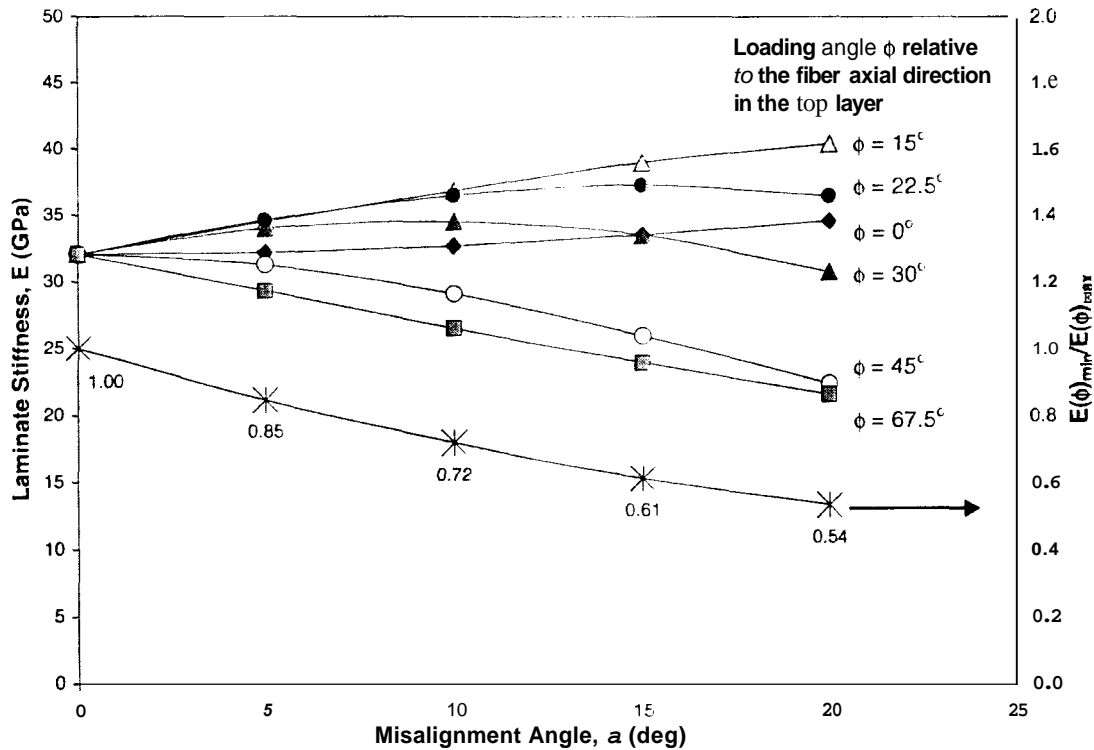


Fig. 48. Influence of laminate layup misalignment on the stiffness of quasi-isotropic composite.

Note, however, that the results shown in Fig. 48 correspond to the assumed misaligned configuration depicted in Fig. 46. This configuration may or may not correspond to the actual misalignments that occur during the layup process. Due to practical limitations, it is only possible to measure the angular orientations of the outer layers of the laminate, while the directions of the inner plies may be estimated with some uncertainty with the aid of X-ray photographs. Nevertheless, an analysis of the idealized misaligned layup shown in Fig. 46 can provide a reasonable estimate for the magnitude of misalignment angles that occurred during the actual layup processes." For the actual ratio of E_{\min}/E_{\max} that was recorded experimentally, it appears that a reasonably good estimate is $\alpha = 5^\circ$.

6.3 STRESS-STRAIN BEHAVIOR IN THE NONLINEAR RANGE

6.3.1 Crossply Composite

To explain certain aspects of observed departures from quasi-isotropic response, it is necessary to utilize the nonlinear stress-strain data of crossply laminates. For the crossply composite, the stress-strain response is highly orientation dependent. For loading orientations $\phi = 0^\circ$ and 90° , which are parallel to fiber directions, the stress-strain curves are nearly linear up to failure, as shown in Fig. 49. However, that linear range diminishes monotonically, and nonlinearity tends to prevail, as the angle between load and fiber direction increases. This angular dependence becomes most pronounced at $\phi = 45^\circ$. The nonlinearity becomes further accentuated with temperature, as shown in Fig. 50.

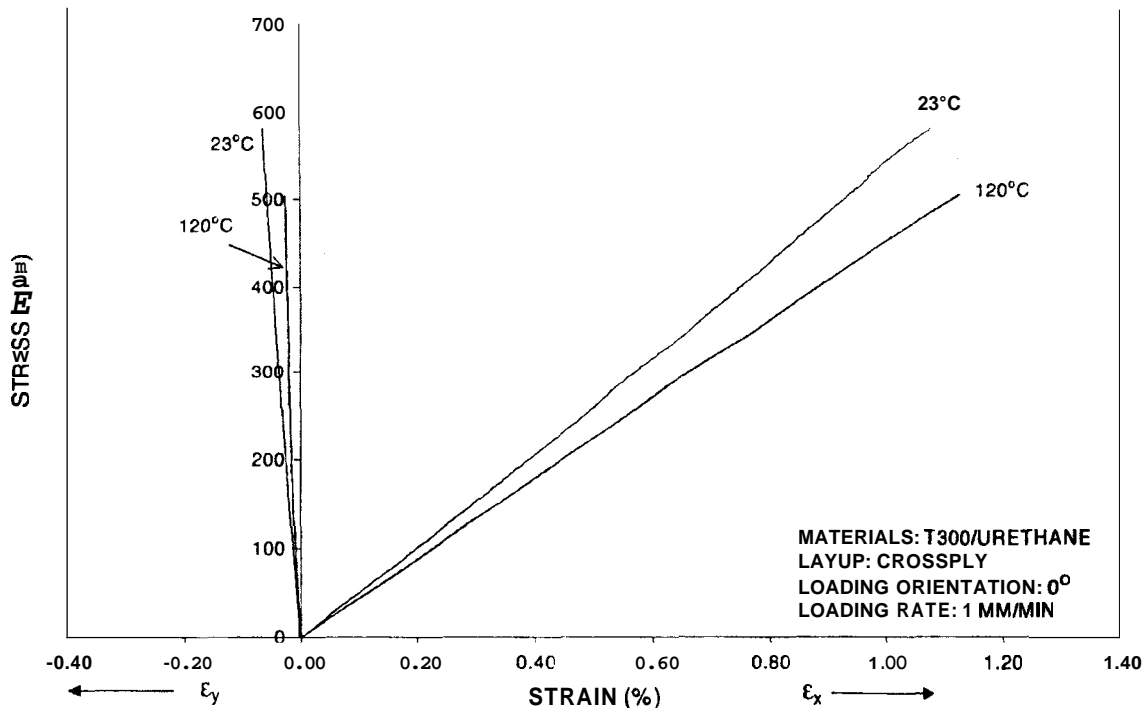


Fig. 49. Typical stress-strain curves of crossply composite, with loads applied at orientation angle $\phi = 0^\circ$ under two temperatures.

*Although a wide scope of possibilities exists for the locations and orientations of the misaligned plies, the in-plane stiffnesses of the laminate are highly insensitive to any particular ordering of those locations within the laminate.

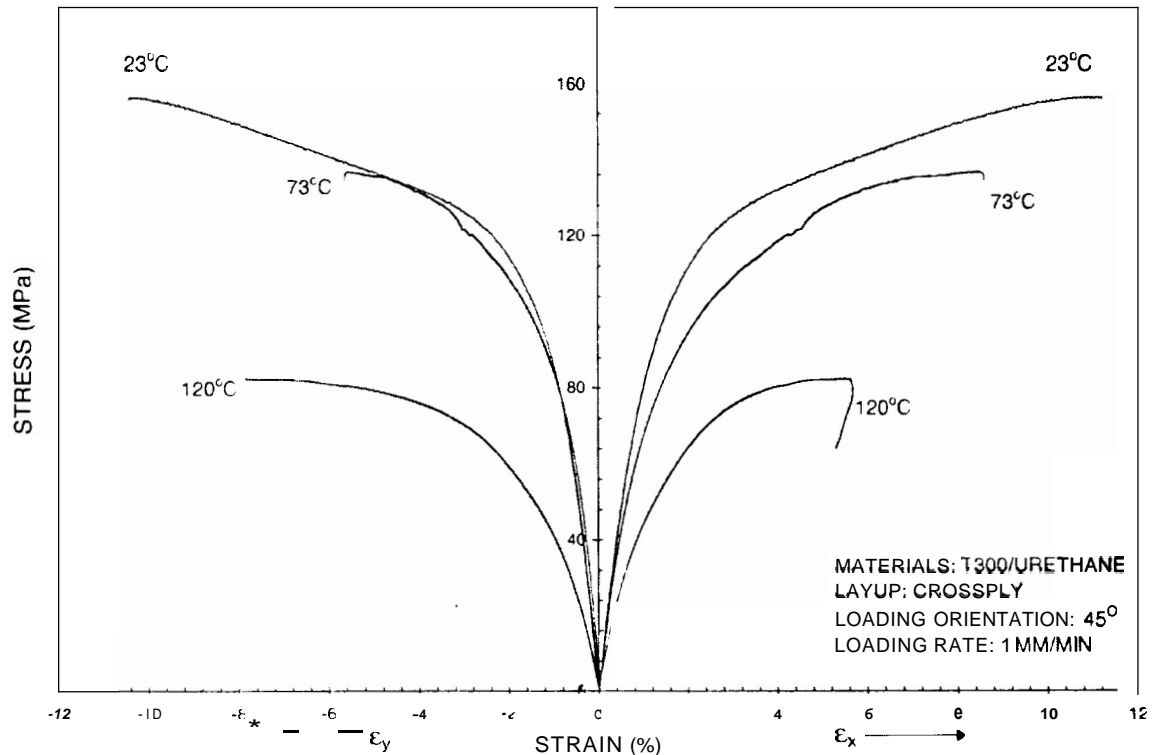


Fig. 50. Typical stress-strain curves of crossply composite, with loads applied at orientation angle $\phi = 45^\circ$ under three temperatures.

6.3.2 Quasi-Isotropic Composite

The main purpose of this subsection is to provide a rational, mechanics-based, explanation for the consistently observed dependence of the stress-strain response of the quasi-isotropic composite on load orientation at the elevated stress range.

Typical stress-strain to failure curves for quasi-isotropic coupons tested at various orientations are shown in Figs. 51–54. Despite the data scatter that is attributable to layup mismatch angles α as shown in Fig. 46, these figures exhibit consistent departures between the response of coupons tested in orientations ϕ , such as 0° , 45° , and 90° , which are parallel to fiber directions, and the softer behavior of samples tested in intermediate orientations ϕ such as 15° , 22.5° , 30° , and 67.5° . Clearly, the response at angles ϕ is nonlinear, with nonlinearity increasing with both stress and temperature. Note that, ideally, all stress-strain curves should coalesce toward a common straight line near the origin. However, this may not occur in all circumstances, because of the aforementioned layup misalignments, as discussed in Sect. 6.2.1. A specific example for a departure between the response at $\phi = 0^\circ$ and the behavior at $\phi = 22.5^\circ$, which emanates from the origin of the stress and strain coordinates, is shown in Fig. 55. Obviously, in this case some of the plies in the sample tested at $\phi = 22.5^\circ$ are misaligned about their designated quasi-isotropic orientations, and the effects of nonlinearity and misalignment compound each other. Other causes, such as an unequal spacings between fiber strands, can also contribute to the observed disparity.

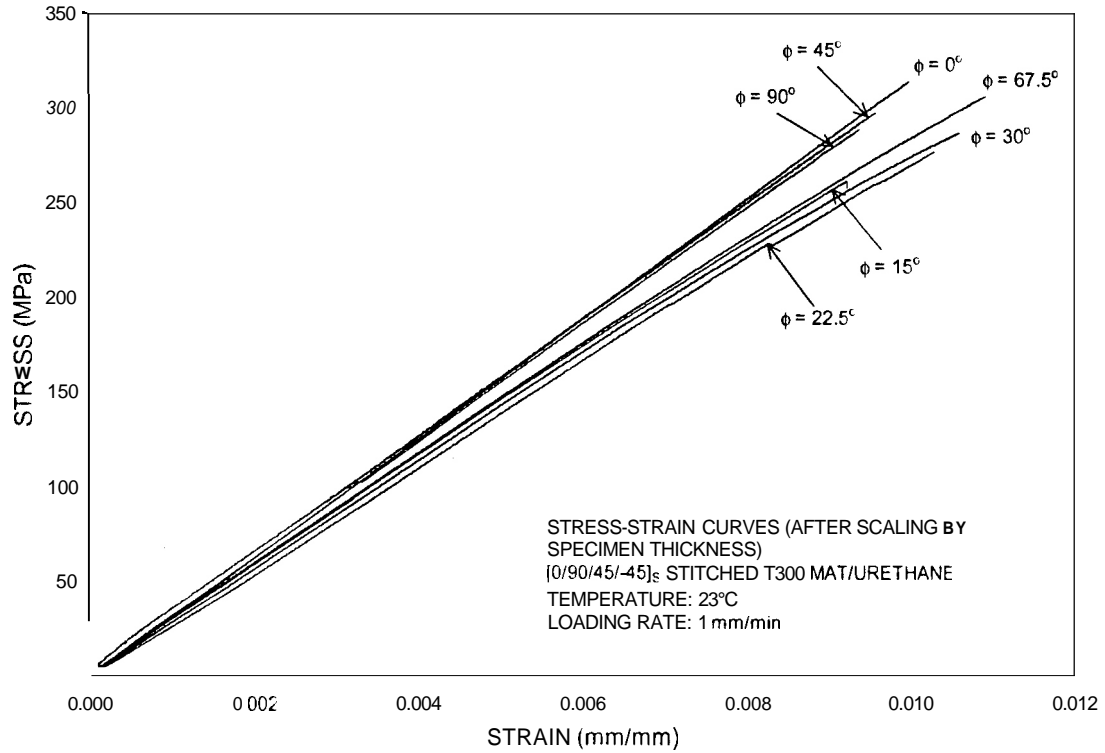


Fig. 51. Typical stress-strain curves of quasi-isotropic composite at various orientations at 23°C.

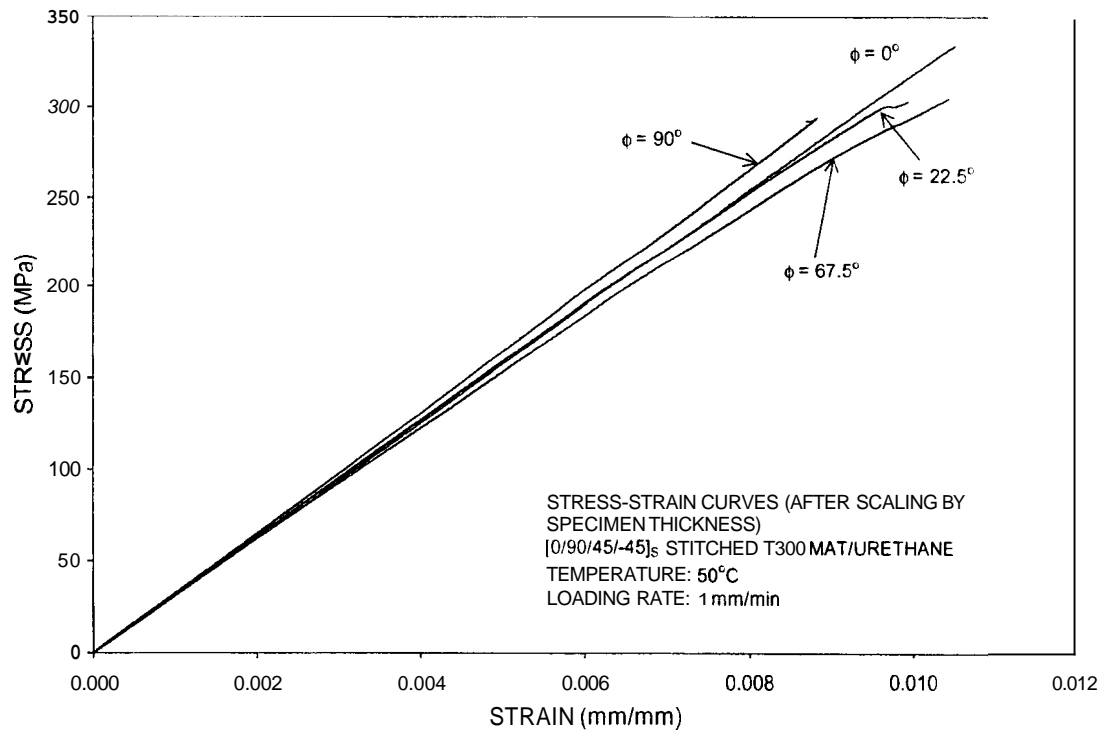


Fig. 52. Typical stress-strain curves of quasi-isotropic stitched composite at various orientations at 50°C.

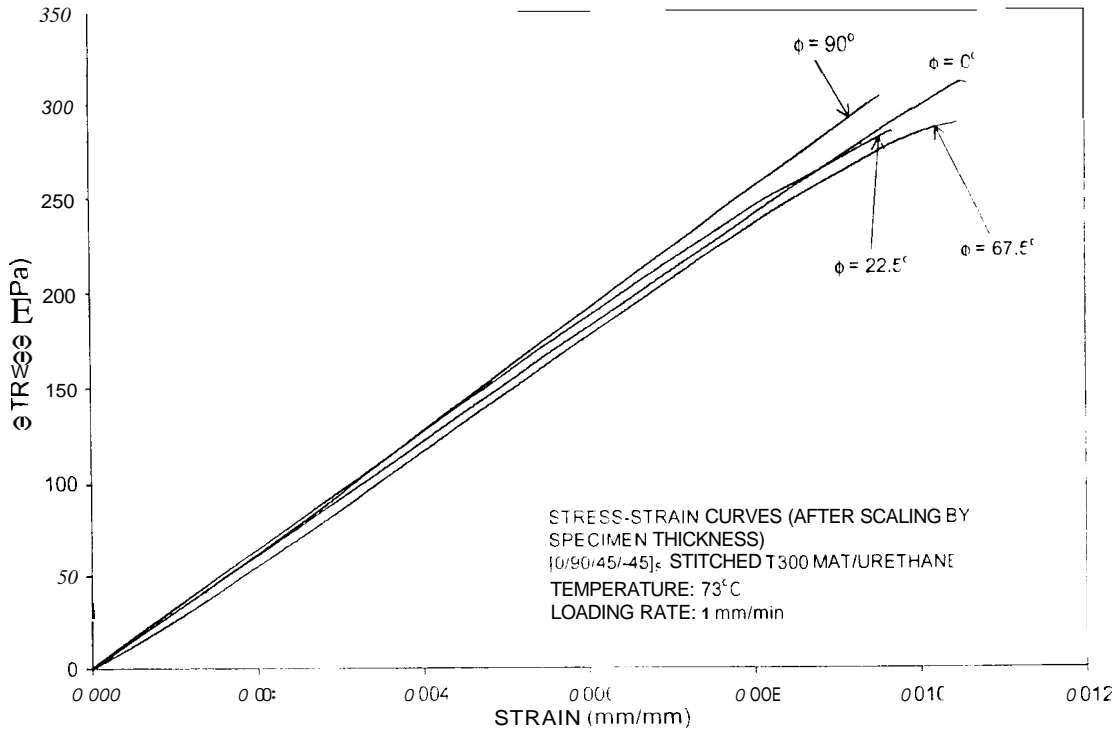


Fig. 53. Typical stress-strain curves of quasi-isotropic composite at various orientations at 73°C.

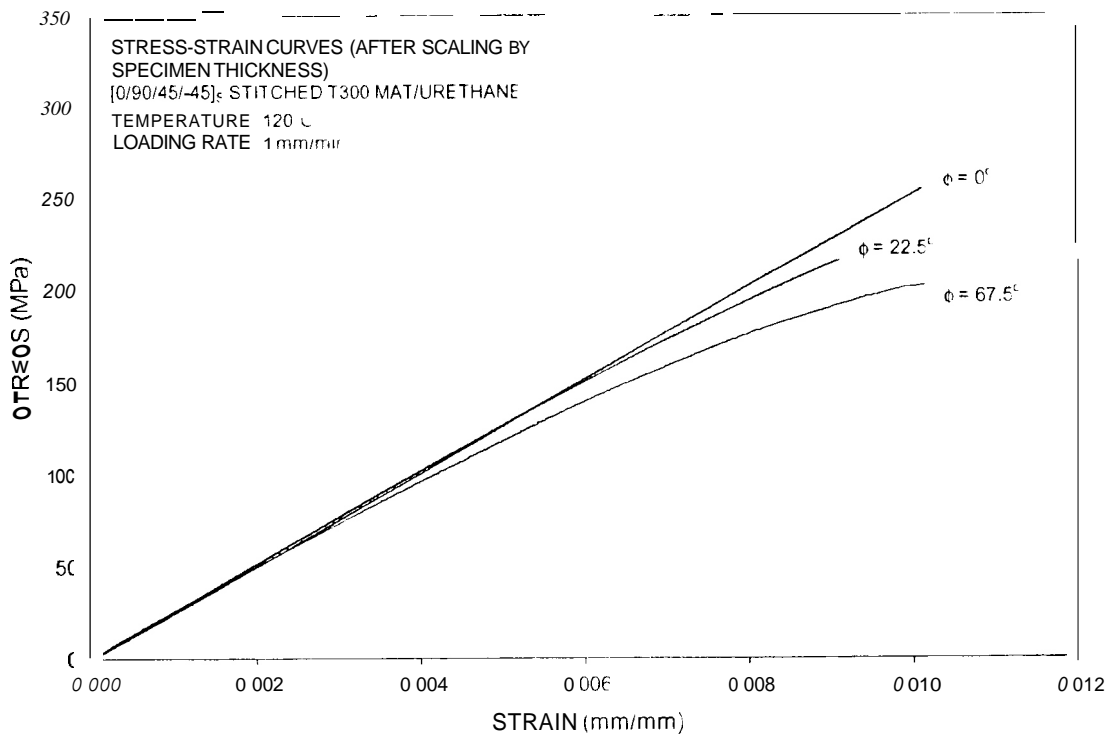


Fig. 54. Typical stress-strain curves of quasi-isotropic composite at various orientations at 120°C.

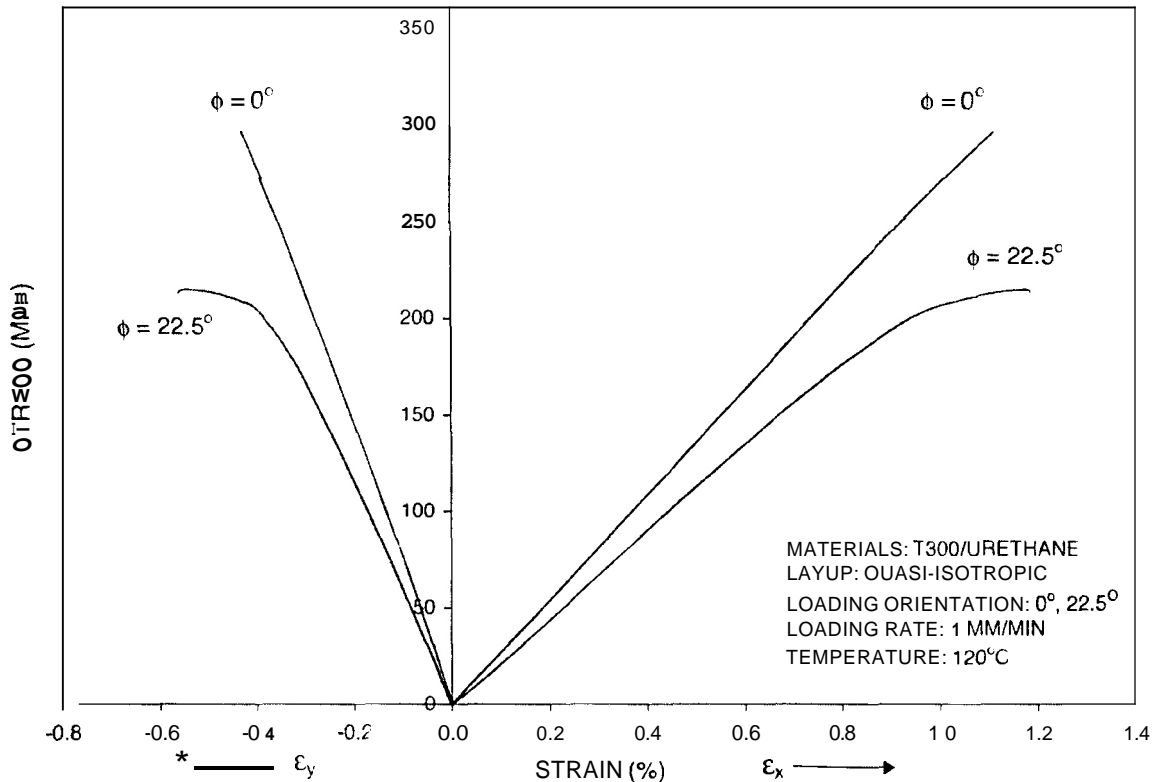


Fig. 55. Comparison of stress-strain curves of quasi-isotropic composite with two different loading orientations ($\phi = 0^\circ$ and 22.5°) at 120°C .

6.3.3 Basic Nonlinear Properties and an Approximate Model

It is possible to account for the nonlinear behavior of fiber-reinforced polymeric composites by means of plasticity and viscoplasticity theories¹¹⁻¹³ The formulation involves the association of the effective stress $\bar{\sigma}$ with the effective plastic strain $\bar{\epsilon}^p$ within the larger context of plasticity theory. Because a negligible amount of nonlinearity occurs parallel to the fiber direction, x_1 , the normal stress σ_{11} is assumed to play no role in $\bar{\sigma}$. Thereby, in a two-dimensional case, the effective stress $\bar{\sigma}$ is associated with shear stress, τ_{12} , and the stress normal to the fiber direction, σ_{22} , through the expression

$$\bar{\sigma} = \left[\frac{3}{2} (\sigma_{22}^2 + 2a\tau_{12}^2) \right]^{1/2} .$$

Furthermore, in most circumstances, $\bar{\sigma}$ and $\bar{\epsilon}^p$ were related by the empirical expression $\bar{\epsilon}^p = A\bar{\sigma}^n$. The details are reproduced in Appendix C.

The determination of the parameters a, A , and n requires the employment of a comprehensive experimental program that utilizes unidirectionally reinforced off-axis plies, at various off-axis orientations, θ , although it appears that balanced $\pm\theta$ angle plies could also be utilized. Unfortunately, such samples were not available for the composite at hand.

It was therefore decided to assess the values of a, A , and n from the quasi-isotropic data by means of an approximate approach and subsequently verify the validity of those parameters by employing them to predict the nonlinear response of the $[\pm 45]_{3S}$ crossply samples, utilizing an

incremental computational method. The rationale behind the current approach is that because the quasi-isotropic layups exhibited only a limited amount of plasticity, a nonincremental representation of their nonlinear stress-strain behavior would simplify the evaluation of the parameters a, A , and n , while keeping the errors within acceptable limits. However, in view of the significant nonlinearity in the response of the $[\pm 45]_{3S}$ crossply samples, the prediction of their behavior by means of the more accurate model would establish the validity of the aforementioned parametric values.

For a single, off-axis, unidirectional composite under monotonically increasing load N_x , the increment of the total strain can be decomposed into elastic and plastic portions:

$$\begin{aligned} d\epsilon_x &= d\epsilon_x^e + d\epsilon_x^p ; \\ d\epsilon_y &= d\epsilon_y^e + d\epsilon_y^p . \end{aligned} \quad (31)$$

As mentioned earlier, the stress-strain response of the quasi-isotropic composite exhibited only small-to-moderate nonlinearity, as shown in Fig. 56. Thereby, it was decided to avoid a step-by-step, incremental, laminate analysis for this layup and, as an approximation, to integrate Eq. (31) directly, thereby obtaining for each individual ply

$$\epsilon_x = \bar{s}_{11} \sigma_x + [h(\theta)]^{n+1} A \sigma_x^n ; \quad (32)$$

$$\epsilon_y = \bar{s}_{12} \sigma_x + \nu_{xy}^p [h(\theta)]^{n+1} A \sigma_x^n \quad (33)$$

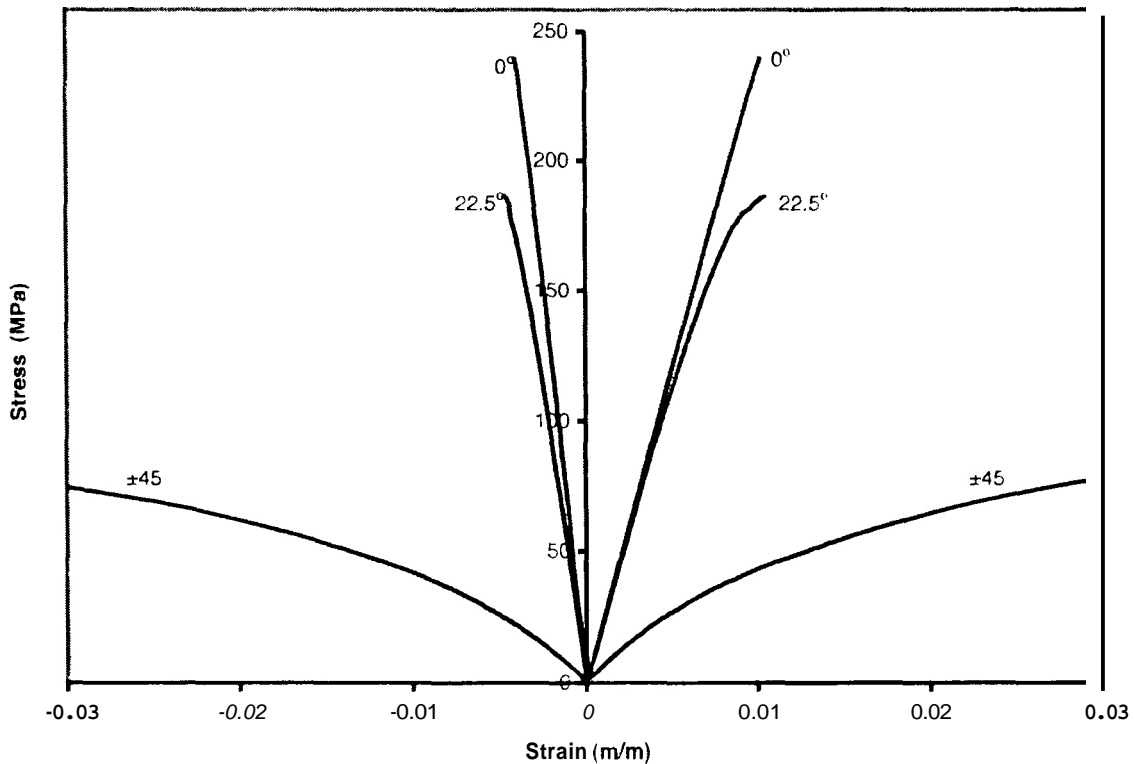


Fig. 56. Longitudinal and transverse strains vs stress for quasi-isotropic and $[\pm 45]_{3S}$ coupons at 120°C .

In Eqs. (32) and (33), \bar{s}_{11} and \bar{s}_{12} are the off-axis elastic compliance components of unidirectional lamina, while A , n , and $h(\theta)$ are the plastic parameters and transformation function detailed in Appendix C and given in Eq. (C.13). Furthermore, the “plastic Poisson’s ratio” ν_{xy}^p can be expressed as⁸

$$\nu_{xy}^p = -\frac{1-2a}{2a + \tan^2 \theta} \quad (34)$$

In view of the fact that the longitudinal plastic strain must have a common value for each and every ply in the laminate at all stress levels, as shown in Fig. 57, Eq. (32) yields

$$[h(\theta)]_1^{n+1} A \sigma_{x,1}^n = [h(\theta)]_2^{n+1} A \sigma_{x,2}^n = \dots = [h(\theta)]_N^{n+1} A \sigma_{x,N}^n = \epsilon_x^p, \quad (35)$$

where N is the number of plies of the laminate. For plies of equal thickness t , the average stress σ_x is given by

$$\sigma_x = \frac{N_x}{H} = \frac{t}{H} \left(\sigma_{x,1} + \sigma_{x,2} + \dots + \sigma_{x,N} \right), \quad (36)$$

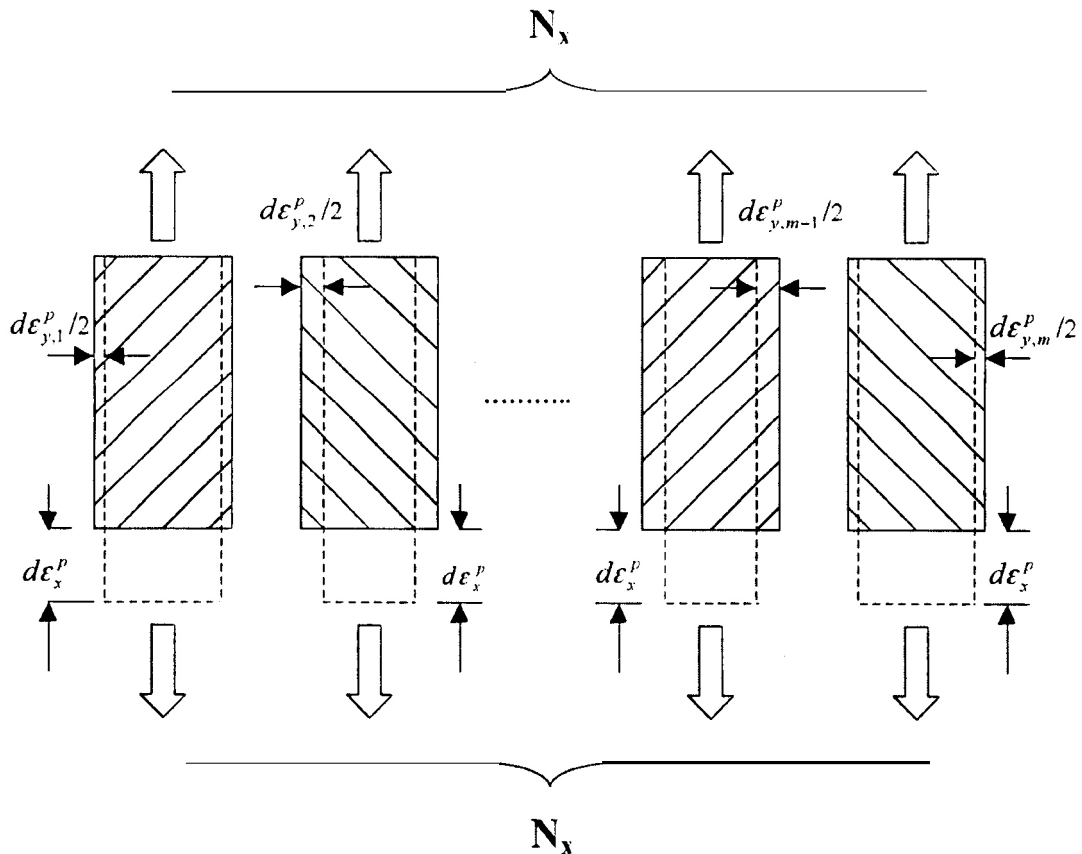


Fig. 57. Schematic drawing of strain compatibility requirements for composite laminates.

where $H = Nr$ is the laminate thickness, and all ply stresses $\sigma_{x,i}$ must satisfy Eq. (35). Note that the total number of plies of the laminate is $N = H/r$; thus, the average stress σ_x may be expressed as:

$$\begin{aligned} \sigma_x &= \frac{1}{N} \left\langle \left\{ \frac{\sigma_x}{[h(\theta)]_i^{1+\frac{1}{n}}} \right\}^n \right\rangle \frac{\epsilon_x^p}{[h(\theta)]_N^{1+\frac{1}{n}}} \\ &= \frac{1}{N} \left\langle \frac{1}{[h(\theta)]_i^{1+\frac{1}{n}}} \right\rangle \left(\frac{\epsilon_x^p}{A} \right)^{\frac{1}{n}} \end{aligned} \quad (37)$$

which leads to

$$\epsilon_x^p = N^n \frac{A}{\left\{ \sum_{i=1}^N \frac{1}{[h(\theta)]_i^{1+\frac{1}{n}}} \right\}^n} \sigma_x^n \quad (38)$$

Similarly, the average value of the transverse plastic strain can be approximated by

$$\begin{aligned} \epsilon_y^p &= \frac{1}{N} \left(\epsilon_{y,1}^p + \epsilon_{y,2}^p + \dots + \epsilon_{y,N}^p \right) \\ &= \frac{1}{N} \left(\nu_{xy,1}^p + \nu_{xy,2}^p + \dots + \nu_{xy,N}^p \right) \epsilon_x^p \end{aligned} \quad (39)$$

resulting in an averaged "plastic Poisson's ratio"

$$\nu_{xy}^p = \frac{1}{N} \sum_{i=1}^N \nu_{xy,i}^p \quad (40)$$

The total strain-stress relation may thus be expressed as:

$$\epsilon_x = H a_{11} \sigma_x + N^n \frac{A}{\left\{ \sum_{i=1}^N \frac{1}{[h(\theta)]_i^{1+\frac{1}{n}}} \right\}^n} \sigma_x^n \quad (41)$$

$$\epsilon_x = Ha_{12}\sigma_x + N^{n-1} \frac{A \left[\sum_{i=1}^N v_{xy,i}^p \right]}{\left\{ \sum_{i=1}^N \frac{1}{[h(\theta)]_i^{1+\frac{1}{n}}} \right\}^n} \sigma_x^n \quad (42)$$

The first terms on the right sides of Eqs. (41) and (42) account for the elastic portions of ϵ_x . In those equations a_{11} and a_{12} are the well known linear laminate level compliances. Denote the elastic coefficients η_x and η_y as $\eta_x = Ha_{11}$ and $\eta_y = Ha_{12}$, and let the plastic coefficients ξ_x and ξ_y be

$$\xi_x = N^n \frac{A}{\left\{ \sum_{i=1}^N \frac{1}{[h(\theta)]_i^{1+\frac{1}{n}}} \right\}^n} \quad (43)$$

$$\xi_y = N^{n-1} \frac{A \left[\sum_{i=1}^N v_{xy,i}^p \right]}{\left\{ \sum_{i=1}^N \frac{1}{[h(\theta)]_i^{1+\frac{1}{n}}} \right\}^n} \quad (44)$$

Equations (41) and (42) are then reduced to

$$\epsilon_x = \eta_x \sigma_x + \xi_x \sigma_x^n \quad (45)$$

$$\epsilon_y = \eta_y \sigma_x + \xi_y \sigma_x^n \quad (46)$$

The elastic and plastic coefficients η_x , η_y , ξ_x , ξ_y , and the parameter n in Eqs. (45) and (46) may be evaluated by fitting experimental data. This was accomplished by means of a nonlinear optimization scheme that was designed to determine the η_x , η_y , ξ_x , ξ_y , and n values that correspond to the best least-square fit against both ϵ_x and ϵ_y vs σ_x data sets. An outline of this scheme is given in Appendix D.

Once the plastic parameter n and coefficients ξ_x , and ξ_y were determined by the aforementioned optimization procedure, the remaining plastic parameters \mathbf{A} and \mathbf{a} [the parameter \mathbf{a} is embedded in the function $h(\theta)$] can be determined by correlating Eqs. (43), (44) and (C.13).*

Note that the present approximation inherently discards any nonlinearity that occurs in the quasi-isotropic composite loaded in any of the fiber directions because by Eq. (C.13), $h(\theta) = 0$, and thereby both ξ_x and ξ_y vanish. This deficiency results from the assumption inherent in the current approximation that overlooks the requirement of ply-by-ply uniformity of the transverse strain ϵ_y throughout the laminate. As noted earlier, the above approximation is not admissible for

* See Appendix C for Eq. (C.13).

crossply laminates loaded in off-axis directions because in those circumstances nonlinearity dominates the response.

The optimization scheme was employed to fit the stress-strain data shown in Fig. 56 for the quasi-isotropic laminates loaded at 22.5° about the 0° fiber direction, at 120°C . The scheme yielded the values of $n = 6.619$, $a = 3.983$, and $A = 8.923 \times 10^{-19}$ (MPa^{-n}). The resulting predictions, for both σ_x vs ϵ_x and σ_x vs E_p , are plotted in Fig. 58 where they are compared against the experimental data. In view of the previous remarks, these values are approximate. Nevertheless, it is worth noting that the values of η_x and η_y came in close agreement with the laminate values Ha_{11} and Ha_{22} .

To assess the validity of the aforementioned approximate values of n , a , and A , these parameters were employed to predict the response of the $[\pm 45]_{3S}$ crossply composite by means of a detailed incremental scheme that ascertained uniformity of both longitudinal and transverse strains.

The plasticity strain-stress expression from Appendix C is

$$\epsilon_{x,i}^p = [h(\theta)]_i^{n+1} A \sigma_{x,i}^n \quad (C.18)$$

which can be written as

$$\sigma_{x,i} = \left\{ \frac{1}{[h(\theta)]_i^{n+1} A} \right\}^{\frac{1}{n}} (\epsilon_{x,i}^p)^{\frac{1}{n}} \quad (47)$$

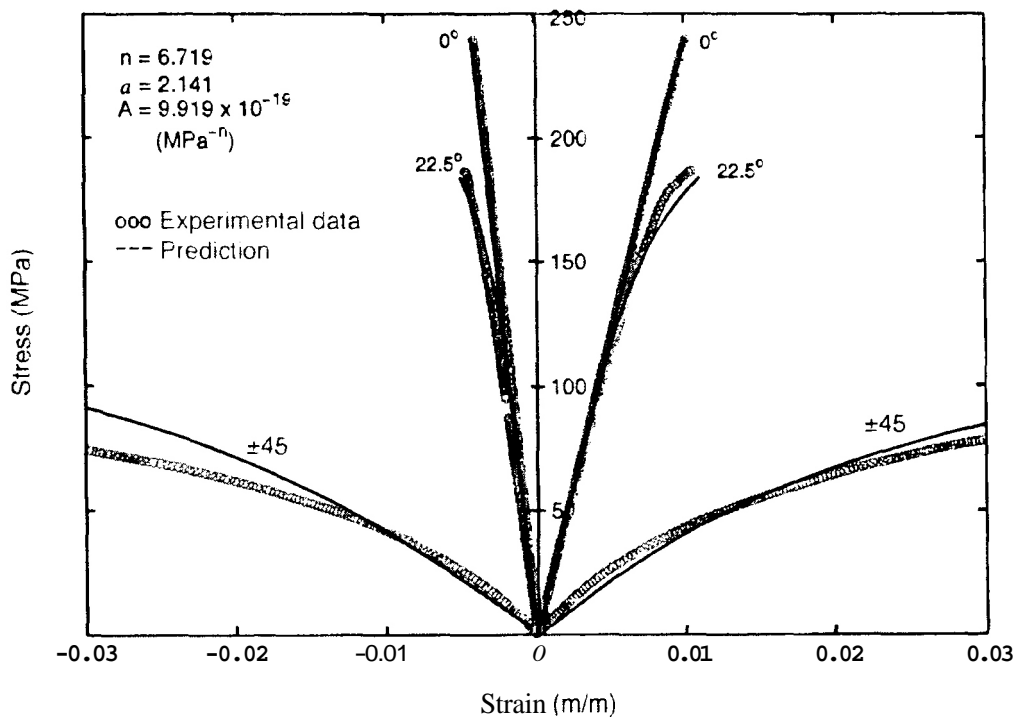


Fig. 58. Predicted and recorded values of longitudinal and transverse strains for the laminates and loading conditions noted in Fig. 55. Predictions based on elasto-plastic behavior with $n = 6.719$, $a = 2.141$, and $A = 9.919 \times 10^{-19} \text{MPa}^{-n}$. Data for $[\pm 45]_{3S}$ crossply laminates was included in generating the above values.

Differentiation of Eq. (47) gives the incremental relationship

$$d\sigma_{x,i} = \frac{1}{n[h(\theta)]_i^{1+\frac{1}{n}} A^{\frac{1}{n}}} (\epsilon_{x,i}^p)^{\frac{1}{n}-1} d\epsilon_{x,i}^p \quad (48)$$

Because, by hypothesis [Eq. (36)], all $\epsilon_{x,i}^p$ and $d\epsilon_{x,i}^p$ have common values for all plies, the summation of all increments $d\sigma_{x,i}$ yields the following expression for the average stress increment:

$$d\sigma_x = \frac{1}{N} \left\{ \sum_{i=1}^N \frac{1}{n[h(\theta)]_i^{1+\frac{1}{n}} A^{\frac{1}{n}}} \right\} (\epsilon_x^p)^{\frac{1}{n}-1} d\epsilon_x^p \quad (49)$$

Consequently, the incremental relationship between laminate level incremental plastic strain $d\epsilon_x^p$ and stress $d\sigma_x$ reads

$$d\epsilon_x^p = \left\{ \frac{NnA^{\frac{1}{n}}}{\sum_{i=1}^N \frac{1}{[h(\theta)]_i^{1+\frac{1}{n}}}} \right\} (\epsilon_x^p)^{-\frac{1}{n}} d\sigma_x \quad (50)$$

Note also that in view of Eq. (34), ν_{x1}^p has a common value for all plies in the special case of the $[\pm 45^\circ]_{3S}$ layups. Consequently, the requirement of uniformity of transverse strains is automatically satisfied in the present circumstance. Equation (50) was solved numerically for stress increments $\Delta\sigma_x = 1$ MPa. The computations employed the same values of n , a , and A as those selected matching the quasi-isotropic data. Results for both ϵ_x and ϵ_y vs σ_x are also shown in Fig. 58, where good agreement is exhibited between computational prediction and experimental data for the crossply composite.

Nevertheless, the current computation scheme does not address the requirement that the plastic component of shear stress, namely γ_{xy}^p , should also be common to all plies. It is reasonable to expect that the accounting for this latter requirement would further reduce the level of a , that corresponds to a prescribed level of E , thus leading to an even better fit between data and predictions for the response of the $[\pm 45^\circ]_{3S}$ crossply composite shown in Fig. 58.

With regard to the quasi-isotropic specimens, note that the stress-strain data for the 22.5° load orientation exhibit an abrupt change in slope prior to failure, as can be seen in Fig. 58. A similar behavior was noticed by other researchers,¹² where such change in slope was attributed to the formation of damage, the representation of which falls beyond the scope of the plasticity formulation used here.

Employing the previous values of a , A , and n and the approximate computational scheme, it was possible to predict the departure from quasi-isotropy at increasing stress levels, as loads continue to be directed away from the fiber directions. Results are shown in Fig. 59.

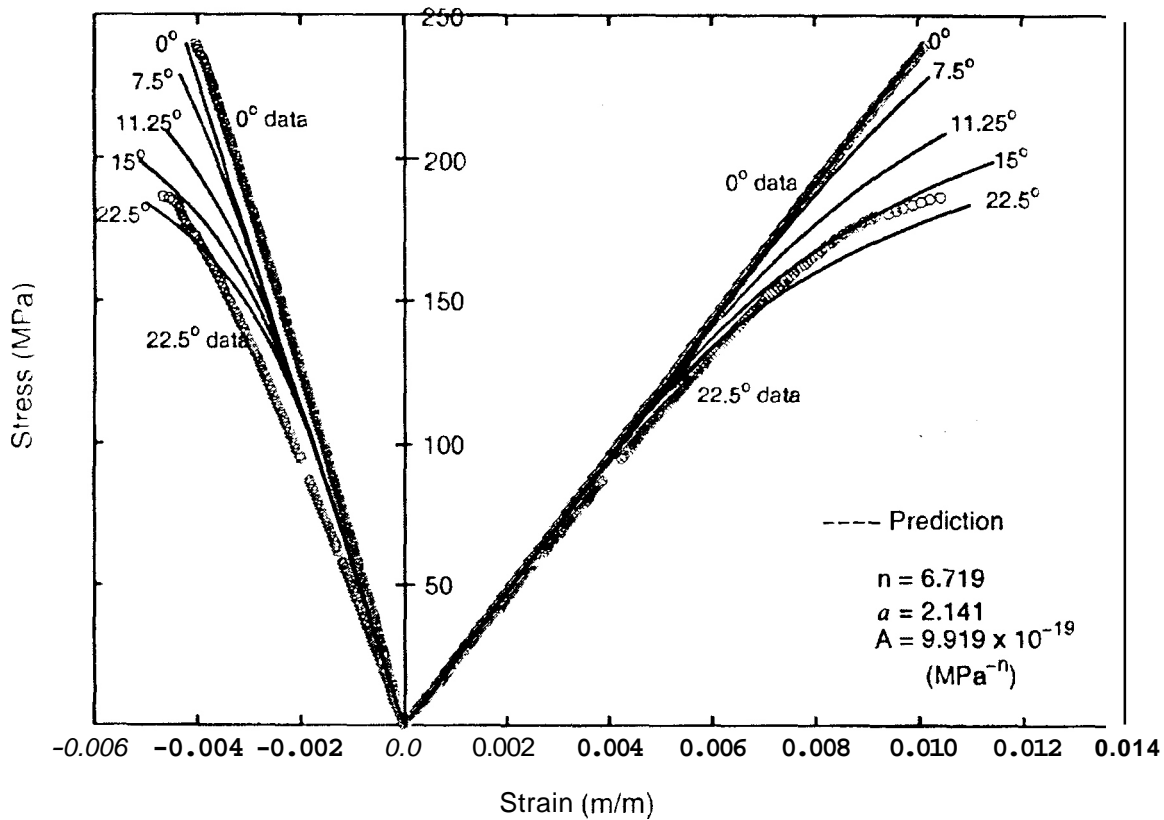


Fig. 59. Predictions of the anisotropic response of quasi-isotropic laminate beyond the linear range, under loading at various orientations about the fiber direction. Comparative data are shown for 0° and 22.5° orientations only.

The plastic components of strain, ϵ_x^p and ϵ_y^p , are shown in Fig. 60 for both the $[0/90/\pm 45]_3$ quasi-isotropic composite, as loads are directed away from the fiber directions, and for the $[\pm 45]_{3S}$ crossply composite. It can be observed that for the quasi-isotropic composite, the effect of nonlinearity is negligible for stresses below 120 MPa. Above 120 MPa, nonlinearity becomes significant, and the stress-strain response is no longer isotropic. For the crossply composite, nonlinearity appears to occur even at the low stress range and subsequently induces large in-plane deformation.

An estimate of the error associated with the approximate computation of the quasi-isotropic response at a loading orientation of 22.5°, which discarded the required commonality of transverse strains, is exhibited by the curves displayed in Fig. 61. The thin lines in that figure represent the maximum and minimum values of $\epsilon_{y,i}^p$ in individual plies, and the thicker line exhibits the average value of $\epsilon_{y,i}^p$ computed by the approximate method. It can be seen that the width of the error band in terms of strain increases with stress and reaches a range of up to $\pm 20\%$ at failure. The resulting discrepancy for the σ_x vs ϵ_x plot would obviously be smaller.

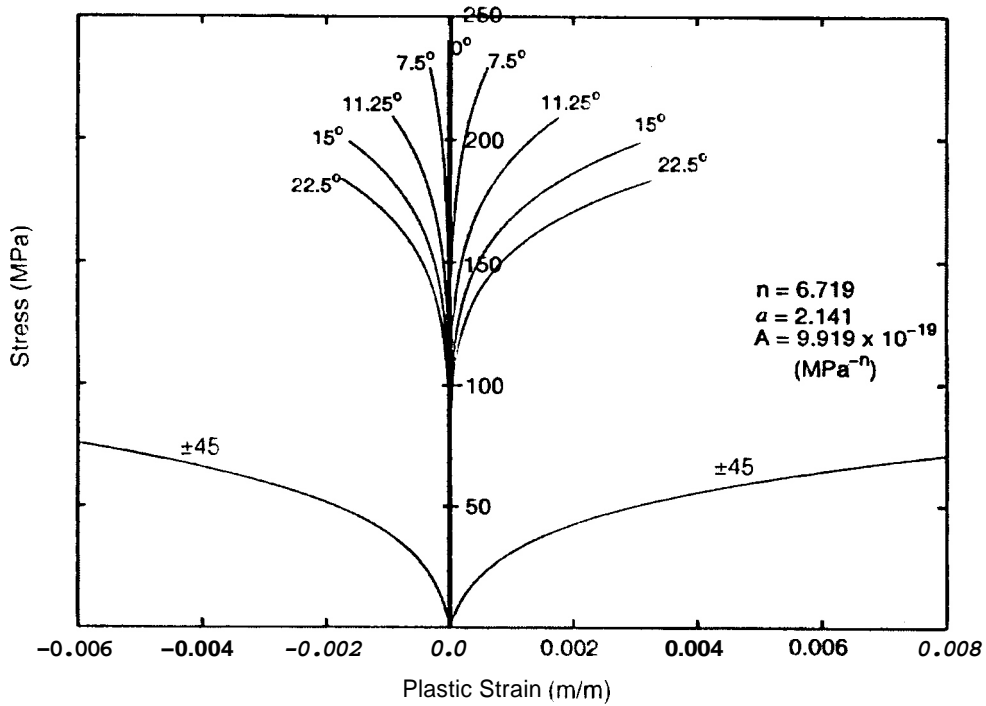


Fig. 60. Predicted values of the longitudinal and transverse components of plastic strains for quasi-isotropic laminates loaded at various orientations about the fiber direction and for $[\pm 45]_{3S}$ laminates.

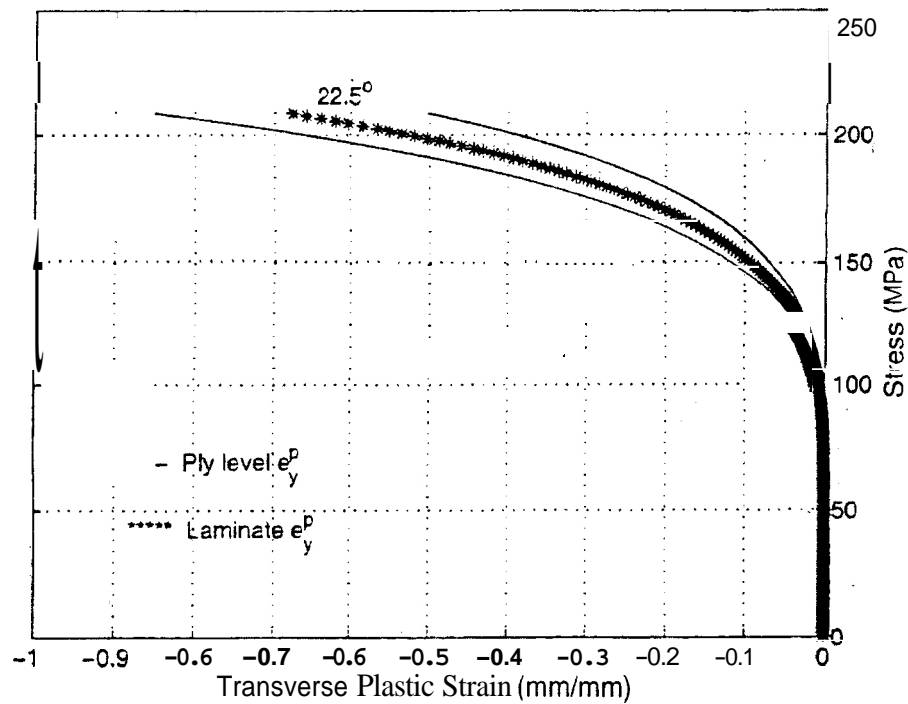


Fig. 61. Maximal and minimal values of transverse plastic strain in the individual plies of a quasi-isotropic laminate loaded at 22.5° about the 0° fiber direction. The disparity provides an error estimate for the approximate scheme.

6.4 TIME-DEPENDENT RESPONSE

6.4.1 Data

Similarly to the case of tensile tests, the creep and recovery behavior of quasi-isotropic composite coupons was found to depend on the load orientation angle ϕ , and this dependence was further accentuated with increasing stress amplitudes. Typical creep and recovery curves of quasi-isotropic coupons under various creep stresses at loading angles $\phi = 0^\circ$ and $\phi = 22.5^\circ$ are shown in Figs. 62 and 63, at temperatures of 73°C and 120°C , respectively. Similar results are shown in Fig. 64 for room temperature (23°C), in which case only five specimens were tested in view of the minimal amount of creep at that temperature level. Nevertheless, it can be seen from the 118.4-MPa tests that even in this case there is a discernible difference between the creep at the "off-axis" direction of 67.5° and the case where loads are applied parallel to a fiber direction, such as 0° or 90° . Furthermore, Figs. 62–64 show that the permanent deformation also depends on load orientation angle ϕ and intensifies with stress and temperature.

6.4.2 Data Reduction

By fitting the creep data with a power-law expression, namely

$$\epsilon_c = (D_0 + D_1 t^n) \sigma_c \quad (51)$$

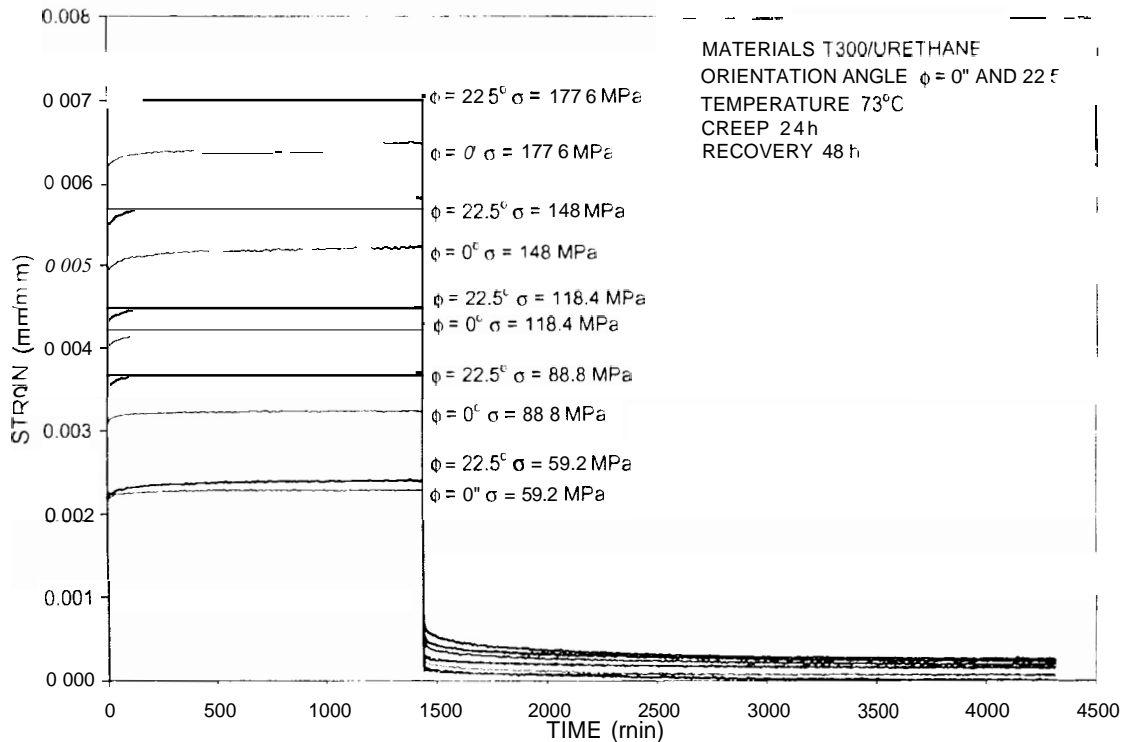


Fig. 62. Typical creep-recovery curves of quasi-isotropic composite with two orientations at 73°C .

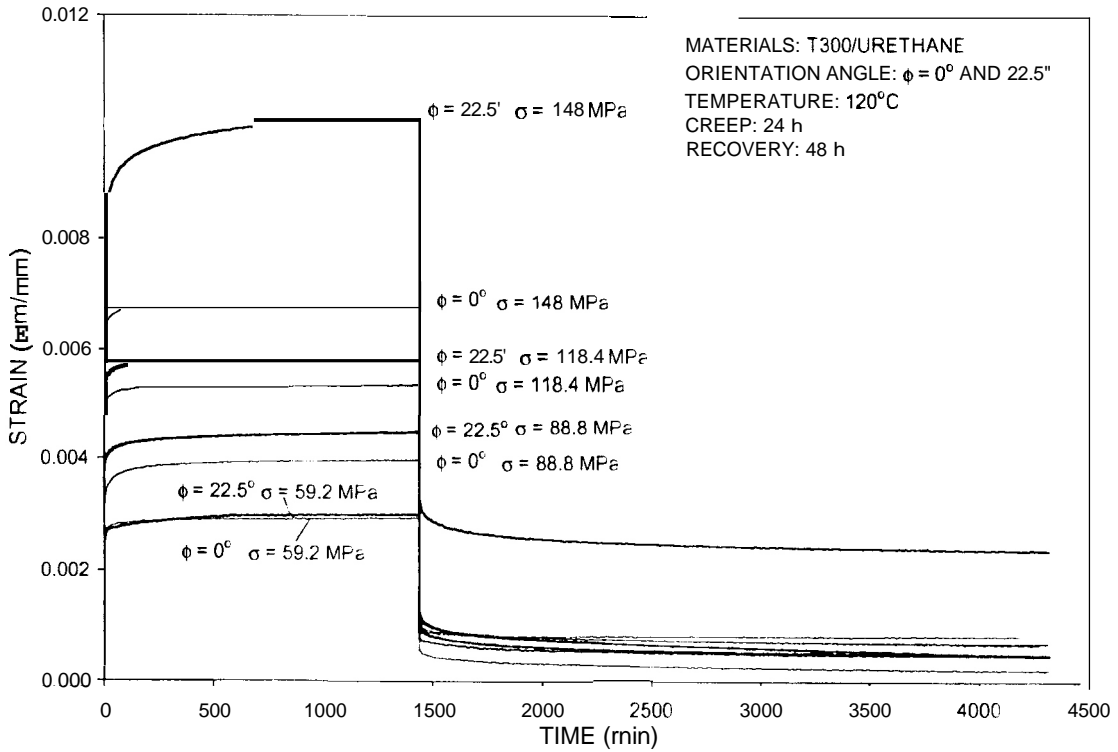


Fig. 63. Typical creep-recovery curves of quasi-isotropic composite with two orientations at 120°C .

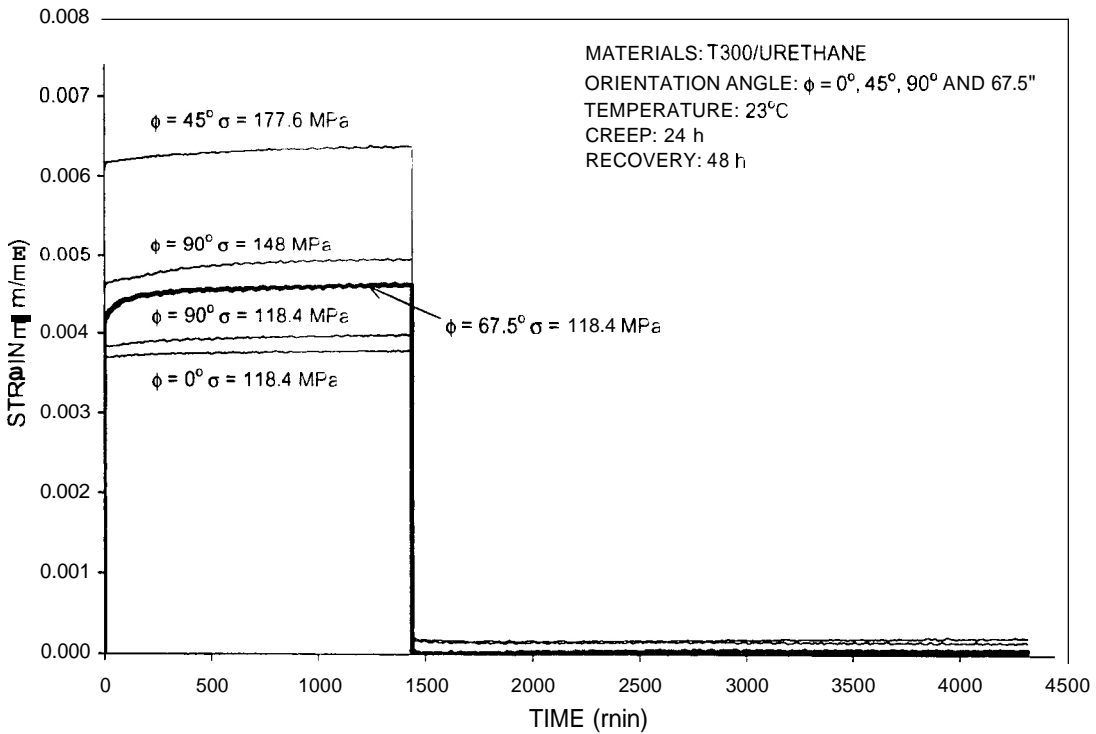


Fig. 64. Typical creep-recovery curves of quasi-isotropic composite with different loading orientations at 23°C .

one can obtain the parameters D_0 , D_1 , and n as listed in Tables 8 and Table 9. These tables suggest that, for these short tests, D_0 , D_1 and D_1 are essentially independent of stress and orientation angle ϕ . However, the power n appears to be higher for $\phi = 22.5^\circ$ than for $\phi = 0^\circ$.

6.4.3 Correlation Between Tensile Response and Creep Behavior

The creep and recovery responses under different loading angles for the quasi-isotropic coupons appear to be consistent with the behavior observed in the tensile tests. Both creep and residual permanent strains were larger at load orientation of $\phi = 22.5^\circ$ than those that occurred when loads were applied parallel to any of the quasi-isotropic fiber directions. Such difference can be attributed to Irreversible (plastic) nonlinearity, as depicted by the additional deformation ($\Delta\varepsilon$) that develops within the coupons loaded at $\phi = 22.5^\circ$ shown in Fig. 65. As noted earlier, the quantity $\Delta\varepsilon$ was found to increase with stress and temperature.

6.4.4 Prediction of Creep Behavior of Quasi-Isotropic Composites Based on Crossply Viscoelastic Characterization

For the quasi-isotropic layup, the In-plane laminate stiffnesses A_{ij} are independent of the loading orientation ϕ within the linear range. The following expressions for A_{ij} can be obtained from Eq. (30) upon setting $\alpha = 0$:

$$\begin{aligned} A_{11} &= A_{22} = h_o [3(Q_{11} + Q_{22}) + 2Q_{12} + 4Q_{66}] \\ A_{12} &= h_o [(Q_{11} + Q_{22}) + 6Q_{12} - 4Q_{66}] \quad (53) \\ A_{16} &= A_{26} = 0 \quad . \\ A_{66} &= h_o [(Q_{11} + Q_{22}) - 2Q_{12} + 4Q_{66}] \quad . \end{aligned}$$

Table 8. Parameters used for the simulations of the creep and recovery results ($\phi = 0^\circ, 73^\circ\text{C}$)

σ_0 (MPa)	Creep time (h)	Recovery time (h)	D_0 (MPa ⁻¹ , $\times 10^{-5}$)	D_1 (MPa ⁻ⁿ min ⁻ⁿ , $\times 10^{-6}$)	n
59.2	24	48	3.43	1.44	0.045
59.2	24	4h	3.58	2.01	0.045
88.8	24	48	3.34	3.31	0.050
88.8	24	48	3.93	2.20	0.045
88.8	24	48	3.34	2.20	0.045
118.4	24	48	3.51	1.78	0.045
118.4	24	48	3.45	1.08	0.045
118.4	24	48	3.51	2.15	0.080
148	24	48	3.28	1.53	0.060
148	24	48	3.84	1.48	0.060
177.6	24	48	3.58	4.00	0.050
177.6	24	48	2.96	6.20	0.040

**Table 9. Parameters used for the simulations of the creep and recovery results
($\phi = 22.5^\circ, 73^\circ\text{C}$)**

σ_0 (MPa)	Creep time (h)	Recovery time (h)	D_0 ($\text{MPa}^{-1}, \times 10^{-5}$)	D_1 ($\text{MPa}^{-n} \text{min}^{-n}, \times 10^{-6}$)	n
59.2	24	48	3.49	2.95	0.080
59.2	24	4s	3.61	2.50	0.080
88.8	24	48	3.74	3.05	0.045
88.6	24	48	2.93	4.80	0.055
118.4	24	48	3.44	2.14	0.080
118.4	24	4P	3.70	0.65	0.080
148	24	48	3.87	3.41	0.045
148	24	48	3.51	1.60	0.090
177.6	24	48	3.53	1.00	0.050
177.6	24	48	3.53	1.68	0.045
177.6	24	4P	3.59	2.35	0.070

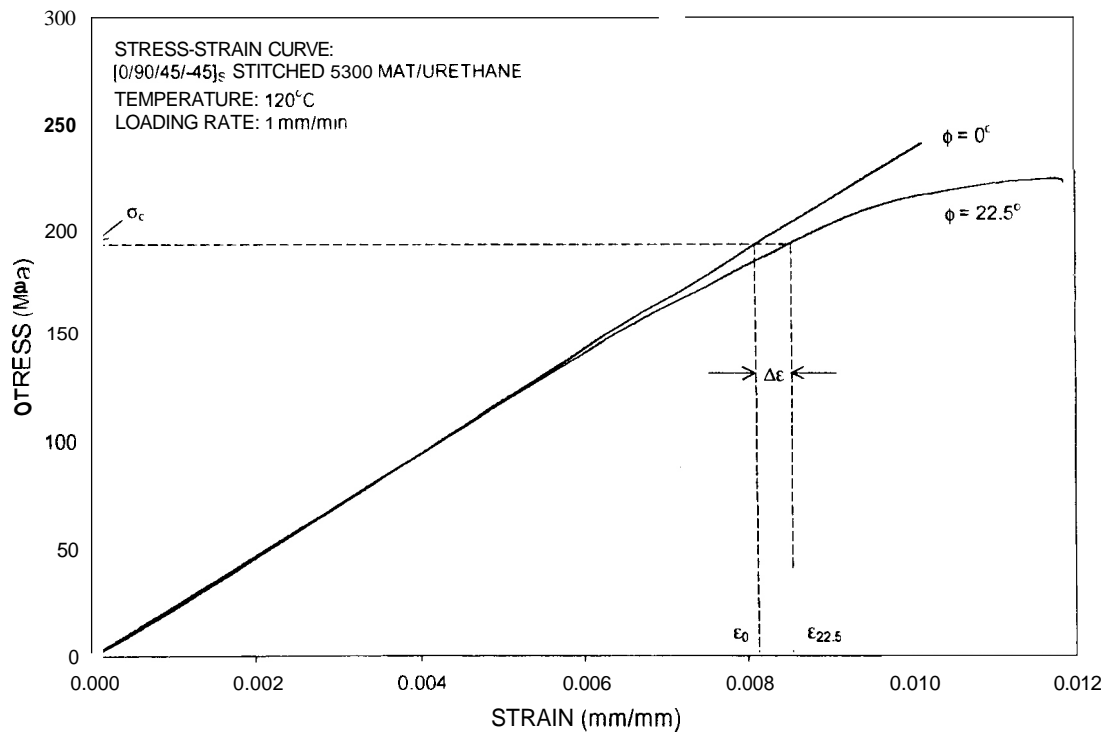


Fig. 65. Typical stress-strain to failure response of quasi-isotropic composite at 120°C with loads applied at $\phi = 0^\circ$ and $\phi = 22.5^\circ$ about the fiber direction.

Subsequently, Eq. (6) yields the following relationship between longitudinal strain ϵ_x and stress σ_x :

$$\epsilon_x = n_p \frac{3(Q_{11} + Q_{22}) + 2Q_{12} + 4Q_{66}}{[3(Q_{11} + Q_{22}) + 2Q_{12} + 4Q_{66}]^2 - [(Q_{11} + Q_{22}) + 6Q_{12} - 4Q_{66}]^2} \sigma_x \quad (54)$$

As noted in Sect. 5.1, it is possible to attribute all time dependence to Q_{66} and express it by means of Eq. (27).

Upon employing $D_0 = 4.18 \times 10^{-5} \text{ MPa}^{-1}$, $D_1 = 6.6 \times 10^{-6} \text{ MPa}^{-n} \text{ min}^{-n}$, and $n = 0.245$ as power-law creep parameters that fall within the range of values that fit the creep data for the crossply composite, it is possible to predict the creep behavior of the quasi-isotropic composite by substituting Eq. (27) into Eq. (53). An example for such a prediction is shown in Fig. 66. Although the values of the instantaneous strain are subject to some uncertainty that is attributable to sample-to-sample variability in the value of $Q_{11} + Q_{22}$, the predicted time-dependent portion of strain falls parallel to the recorded data, exhibiting excellent agreement with experimental results.

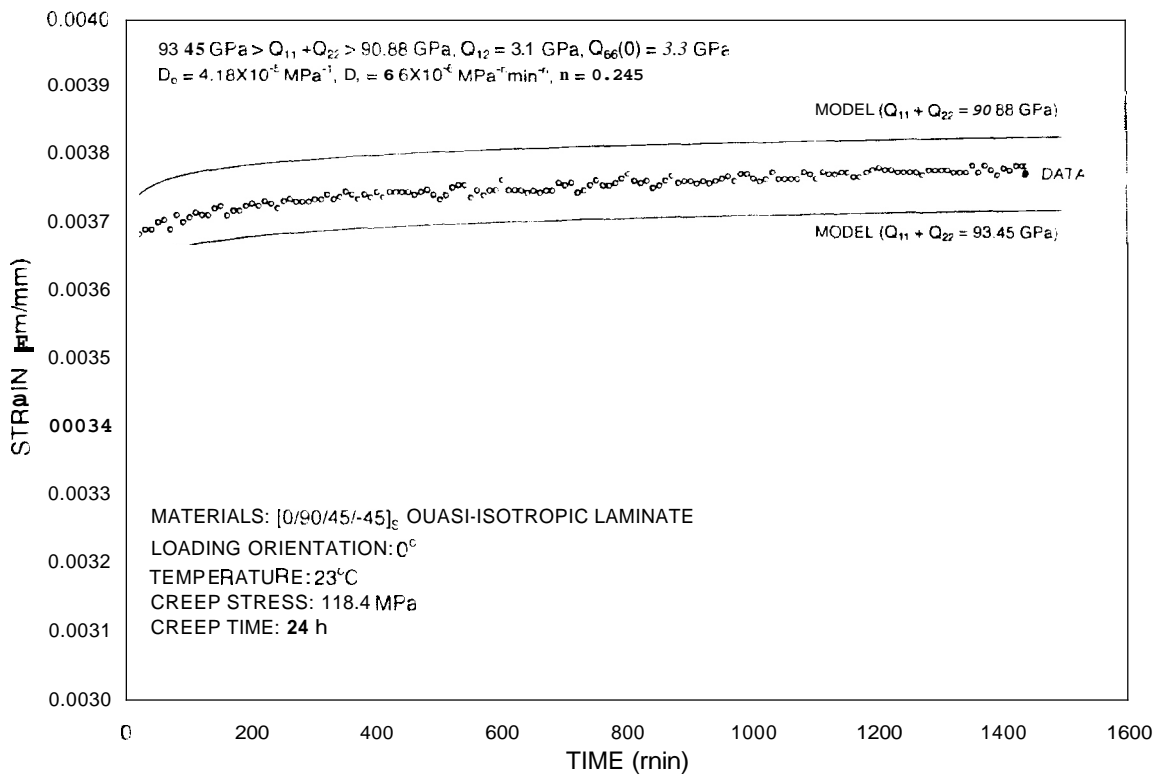


Fig. 66. Prediction of creep behavior of quasi-isotropic composite based on crossply viscoelastic characterization.

7. CONCLUSIONS

The mechanical behavior of stitched T300 mat/urethane 420 IMR composites exhibits a substantial degree of randomness, which most likely results from the presence of multitudes of initial flaws that can be attributed to nonuniformities in resin penetration during the rapid injection process and the nonuniform fiber spacing. The effect of this randomness becomes especially pronounced at elevated stresses and temperatures. Creep under sustained loading, as well as nonlinearity in material response, are caused by the inherent molecular structure of the polymeric phase, but their extents are enhanced by the growth of the abovementioned internal flaws. Because carbon fibers arrest nearly all creep parallel to their directions, this aspect of material behavior is nearly absent in quasi-isotropic laminates. For this same reason, both deformation and creep of crossply layups are highly sensitive to load orientation. This directional dependence of material behavior limits the applicability of crossply laminates to those circumstances where the directions of anticipated design loads are well defined.

In spite of the randomness, it is possible to establish a well-defined safe range for the load carrying capacity of the composite. Within this range, which overlaps the region of linear response, it is possible to predict the behavior of these laminates by means of classical laminate theory in combination with linear viscoelasticity. Note that the light stitching incorporated within the composite has no detrimental effect on its behavior.

REFERENCES

1. J. M. Corum et al., *Basic Properties of Reference Crossply Carbon-Fiber Composite*, ORNL/TM-2000/29. Oak Ridge National Laboratory, March 2000.
2. J. M. Corum et al., *Durability-Based Design Properties of Reference Crossply Carbon-Fiber Composite*, ORNL/TM-2000/322. Oak Ridge National Laboratory, April 2001.
3. J. M. Corum et al., *Durability-Based Design Criteria for a Quasi-Isotropic Carbon-Fiber Automotive Composite*, ORNL/TM-2002/39, Oak Ridge National Laboratory, March 2002.
4. S. Deng and Y. Weitsman, *Mechanical Response of Sritched T300 Mat/Urethane 420 IMR composite Laminates; Property/Orientation Dependence and Damage Evolution*, ORNL/TM-2000/103, Oak Ridge National Laboratory Report, February 2000.
5. ASTM Standard D34 10-87. *Standard Test Method for Compressive Properties of Unidirectional or Crossply Fiber-Resin Composites*. American Society for Testing and Materials.
6. J. Gao and Y. Weitsman. *The Tensile Mechanical Properties and Failure Behavior of Sritched T300 Mat/Urethane 420 IMR Composite*, The University of Tennessee Report, MAES98-2.0-CM. July 1998.
7. J. C. Halpin, *Revised Primer on Composite Materials: Analysis*, 2nd ed., Technomic Publishing Co., Stamford, CT, 1992.
8. J. W. Dally and W. F. Riley. *Experimental Stress Analysis*, McGraw-Hill, Inc., New York, 1991.
9. A. C. Pipkin and T. G. Ropers. "A Non-Linear Integral Representation for Viscoelastic Behavior," *J. Mech. Phys. Solids*, **16**, 1968, pp. 59–72.
10. S. W. Tsai and H. T. Hahn. *Introduction to Composite Materials*, Technomic Publishing Co., Stamford, CT, 1980.
11. C. T. Sun and J. L. Chen. "A Simplified Flow Rule for Characterizing Nonlinear Behavior of Fiber Composites." *J. Comp. Mater.*, **23**, October 1989, pp. 1009–1020.
12. C. T. Sun and K. J. Yoon. "Elastic-Plastic Analysis of AS4/PEEK Composite laminate Using a One-Parameter Plasticity Model," *J. Comp. Mater.*, **26**(2), 1992, pp. 293–308.
13. R. A. Schapery, "Nonlinear Viscoelastic and Viscoplastic Constitutive Equations Based on Thermodynamics," *Mechanics of Time-Dependent Materials*, **1**(2), 1997, pp. 209–240.
14. V. M. Winn and S. Sridharan, "An Investigation into the Accuracy of a One-Parameter Nonlinear Model for Unidirectional Composites," *J. Comp. Mater.*, **16**, 2001, pp. 1491–1507.



Appendix A. POWER-LAW PARAMETERS

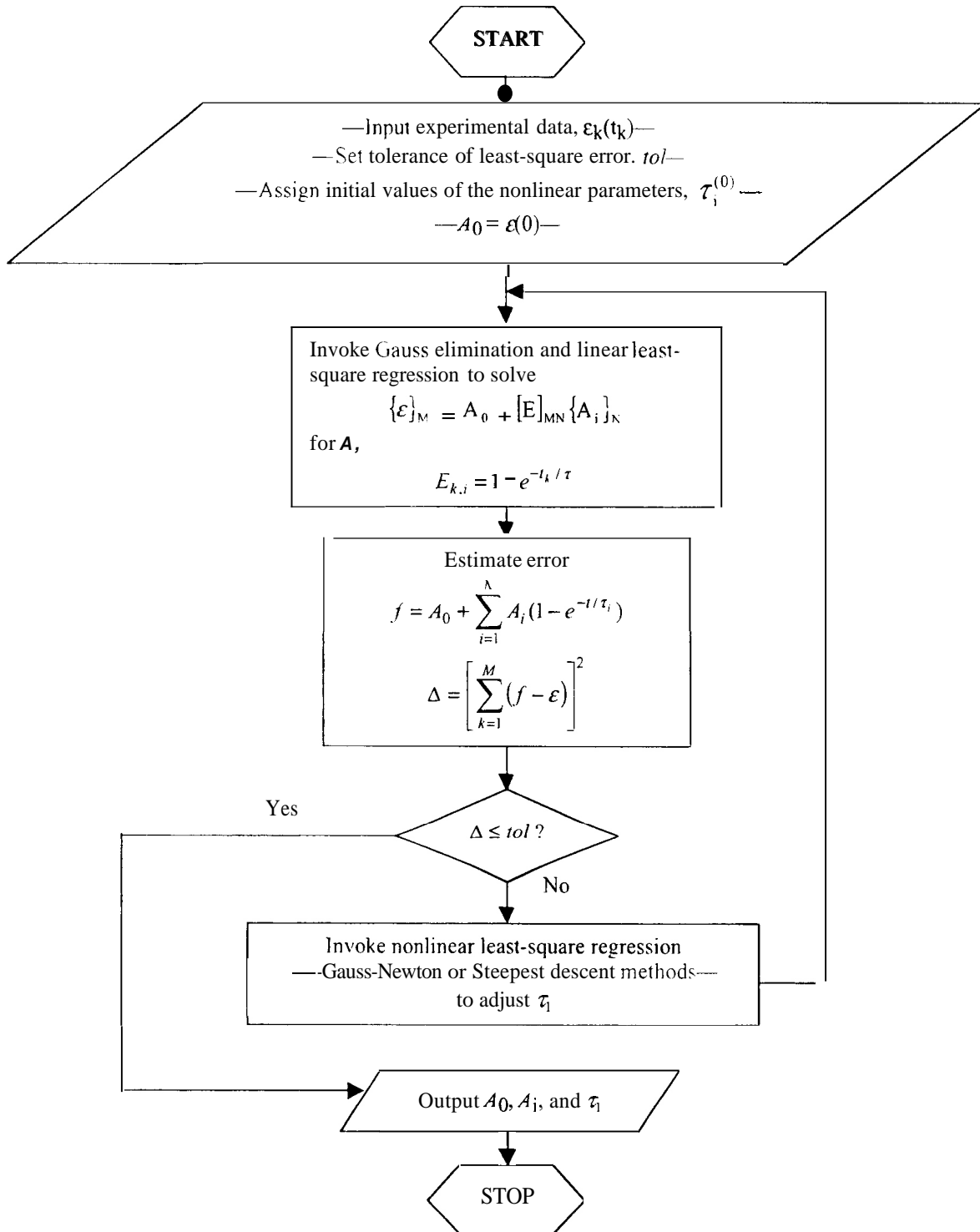
Table A.1. Best-fit power-law parameters D_0 , D_1 , and n for creep data at 31 MPa and several temperatures. Modified values correspond to viscoelastic creep $\epsilon_v(t)$ after accounting for permanent strains $\epsilon_p(t, T, \sigma, \phi)$. (Fits for individual replicate sample data)

σ_0 (MPa)	Creep time (h)	Recovery time (h)	D_0		D_1		n	
			(MPa ⁻¹ , ×10 ⁻⁵)		(MPa ⁻ⁿ min ⁻ⁿ , ×10 ⁻⁶)			
			Unmodified	Modified	Unmodified	Modified	Unmodified	Modified
120°C								
31	5	15	19.0	19.0	219.0	164.0	0.166	0.135
	5	15	22.3	22.3	340.0	215.0	0.110	0.102
	5	15	21.3	21.3	239.0	164.0	0.135	0.110
73°C								
31	1	15	11.0	11.0	27.4	21.4	0.258	0.264
	1	15	13.3	13.3	23.1	19.0	0.287	0.296
31	5	15	9.58	9.58	36.4	20.0	0.167	0.210
	5	15	10.4	10.4	30.3	19.0	0.210	0.220
	5	15	9.45	9.45	31.1	19.2	0.206	0.230
31	24	48	9.03	9.03	63.3	34.2	0.138	0.150
	24	48	10.7	10.7	37.8	25.0	0.149	0.140
50°C								
31	5	15	10.4	10.4	11.7	10.6	0.231	0.240
	5	15	9.34	9.34	9.00	7.12	0.284	0.285
	5	15	11.5	11.5	10.7	8.03	0.281	0.290
23°C								
31	5	15	7.74	7.74	3.44	2.58	0.205	0.198
	5	15	8.25	8.25	1.99	1.66	0.320	0.330
	5	15	8.12	8.12	0.95	0.59	0.340	0.380
31	24	48	8.23	8.23	5.11	5.25	0.194	0.145
	24	48	7.65	7.65	8.85	7.88	0.101	0.101

Table A.2. Best-fit power-law parameters D_0 , D_1 , and n for creep data at 46.5 MPa and several temperatures. Modified values correspond to viscoelastic creep $\varepsilon_v(t)$ after accounting for permanent strains $\varepsilon_p(t, T, \sigma, \phi)$. (Fits for individual replicate sample data)

σ_0 (MPa)	Creep time (h)	Recovery time (h)	D_0		D_1		n	
			(MPa ⁻¹ , ×10 ⁻⁵)		(MPa ⁻ⁿ min ⁻ⁿ , ×10 ⁻⁶)			
			Unmodified	Modified	Unmodified	Modified	Unmodified	Modified
120°C								
46.5	∞	15	28.8	28.8	243.0	229.0	0.203	0.120
	∞	15	25.2	25.2	226.0	202.0	0.203	0.120
	∞	15	16.4	16.4	151.0	52.9	0.204	0.198
	∞	15	16.1	16.1	118.0	88.7	0.168	0.150
73°C								
46.5	1	15	13.5	13.7	39.6	27.5	0.318	0.332
	1	15	12.6	12.6	24.9	14.4	0.227	0.320
46.5	∞	15	10.h	10.6	57.9	25.8	0.146	0.210
	∞	15	10.6	10.6	60.9	33.0	0.130	0.155
	∞	15	10.h	10.8	47.8	34.5	0.179	0.165
	∞	15	10.5	10.5	47.7	28.5	0.184	0.185
	∞	15	10.5	10.5	47.7	28.5	0.184	0.185
46.5	24	48	11.5	11.5	107.0	85.9	0.129	0.128
	24	48	10.7	10.7	38.3	20.9	0.146	0.145
50°C								
46.5	∞	15	9.39	9.34	12.5	11.3	0.265	0.245
	∞	15	8.52	8.52	16.2	11.9	0.220	0.230
	∞	15	8.97	8.97	14.8	12.7	0.249	0.220
23°C								
46.5	∞	15	8.37	8.37	3.92	3.24	0.232	0.245
	5	1f;	8.30	8.30	4.94	4.59	0.244	0.242
	∞	1S	8.99	8.99	2.61	2.68	0.286	0.268
46.5	24	48	7.73	7.73	7.95	5.75	0.164	0.160
	24	48	8.14	8.14	7.65	6.85	0.164	0.145
	24	48	7.36	7.36	6.95	6.49	0.164	0.155

**Appendix B. OPTIMAL DETERMINATION OF LINEAR PARAMETERS A_j
AND NONLINEAR PARAMETERS τ_i OF THE PRONY SERIES**



Appendix C. THE MODELING OF PLASTIC NONLINEARITY IN POLYMERIC COMPOSITES

This appendix summarizes the three-parameter plasticity model proposed by Sun and Chen.¹ The model assumes the distortional energy in a unidirectionally reinforced composite lamina for the state of plane stress to be given by

$$2f(\sigma_{ij}) = \sigma_{22}^2 + 2a\tau_{12}^2 \leq k \quad , \quad (C.1)$$

where a is an empirical plastic parameter, σ_{22} is the in-plane stress transverse to the fiber direction, and τ_{12} is the in-plane shear stress. Also f is the yield function, and k represents the yield surface at which plastic flow occurs. The incremental plastic strain is given by:

$$d\epsilon_{ij}^p = \frac{\partial f}{\partial \sigma_{ij}} d\lambda \quad (C.2)$$

In Eq. (C.2), $d\lambda$ is a proportionality factor, termed the plastic multiplier.

Substituting Eq. (C.1) into (C.2) the plastic strain components may be expressed in an expanded form:

$$\begin{Bmatrix} d\epsilon_{11}^p \\ d\epsilon_{22}^p \\ d\gamma_{12}^p \end{Bmatrix} = \begin{Bmatrix} 0 \\ \sigma_{22} \\ 2a\tau_{12} \end{Bmatrix} d\lambda \quad . \quad (C.3)$$

Consider incremental plastic work per unit volume:

$$dW^p = \sigma_{ij} d\epsilon_{ij}^p = 2fd\lambda \quad . \quad (C.4)$$

Based on equivalent plastic work, a measure of plasticity may be related by effective stress and effective plastic strain, which are defined as

$$\bar{\sigma} = \sqrt{3f} \quad , \quad \text{or} \quad f = \frac{\bar{\sigma}^2}{3} \quad (C.5)$$

and thus

$$d\bar{\epsilon}^p = \frac{2}{3} \bar{\sigma} d\lambda \quad . \quad (C.6)$$

An empirical model, expressed in power-law form, was found to provide a reasonable representation for the plastic behavior of composites. Because nonlinearity in the stress-strain response of many composites appears to occur at the onset of loading, one has

$$\bar{\epsilon}^p = A\bar{\sigma}^n \quad . \quad (C.7)$$

Combining Eqs. (C.1) and (C.5), one obtains

$$\bar{\sigma} = \left[\frac{3}{2} (\hat{\sigma}_{22}^2 + 2a\hat{\tau}_{12}^2) \right]^{\frac{1}{2}} . \quad (C.8)$$

Substitution of Eq. (C.8) into (C.7) yields

$$\bar{\epsilon}^p = A \left[\frac{3}{2} (\hat{\sigma}_{22}^2 + 2a\hat{\tau}_{12}^2) \right]^{\frac{n}{2}} . \quad (C.9)$$

Equations (C.1) and (C.7) through (C.9) suggest that the plastic response of polymeric composites may be characterized by the three constants n , a , and A .

For an off-axis unidirectional composite under uniaxial load N_x oriented at an angle θ about the fiber direction, the stress components relative to the principal directions of symmetry are

$$\begin{Bmatrix} \sigma_{11} \\ \sigma_{22} \\ \tau_{12} \end{Bmatrix} = \begin{Bmatrix} \cos^2 \theta \\ \sin^2 \theta \\ -\sin \theta \cos \theta \end{Bmatrix} \sigma_x \quad (C.10)$$

Also, the plastic strain in the loading direction is

$$d\epsilon_x^p = \cos^2 \theta d\epsilon_{11}^p + \sin^2 \theta d\epsilon_{22}^p - \sin \theta \cos \theta d\gamma_{12}^p \quad (C.11)$$

Combination of Eqs. (C.3), (C.10), and (C.11) leads to

$$d\epsilon_x^p = \frac{2}{3} [h(\theta)] \sigma_x d\lambda , \quad (C.12)$$

where $h(\theta)$ is given by

$$h(\theta) = \left[\frac{3}{2} (\sin^4 \theta + 2a \sin^2 \theta \cos^2 \theta) \right]^{\frac{1}{2}} . \quad (C.13)$$

In conjunction with the transformation function $h(\theta)$, the effective stress and effective plastic strain may also be expressed in terms of σ_x . From Eqs. (C.6), (C.8), and (C.10) one obtains

$$\bar{\sigma} = h(\theta) \sigma_x . \quad (C.14)$$

and

$$d\bar{\epsilon}^p = \frac{2}{3} h(\theta) \sigma_x d\lambda . \quad (C.15)$$

Comparison of Eqs. (C.15) and (C.12) yields

$$d\bar{\epsilon}^p = \frac{d\epsilon_\lambda^p}{h(\theta)} ; \quad (C.16)$$

whereby, upon integration

$$\bar{\epsilon}^p = \frac{\epsilon_\lambda^p}{h(\theta)} . \quad (C.17)$$

Substituting Eqs. (C.14) and (C.17) into Eq. (C.7) one obtains

$$E_x^n = [h(\theta)]^{n+1} A \sigma_x^n . \quad (C.18)$$

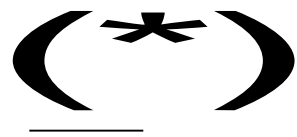
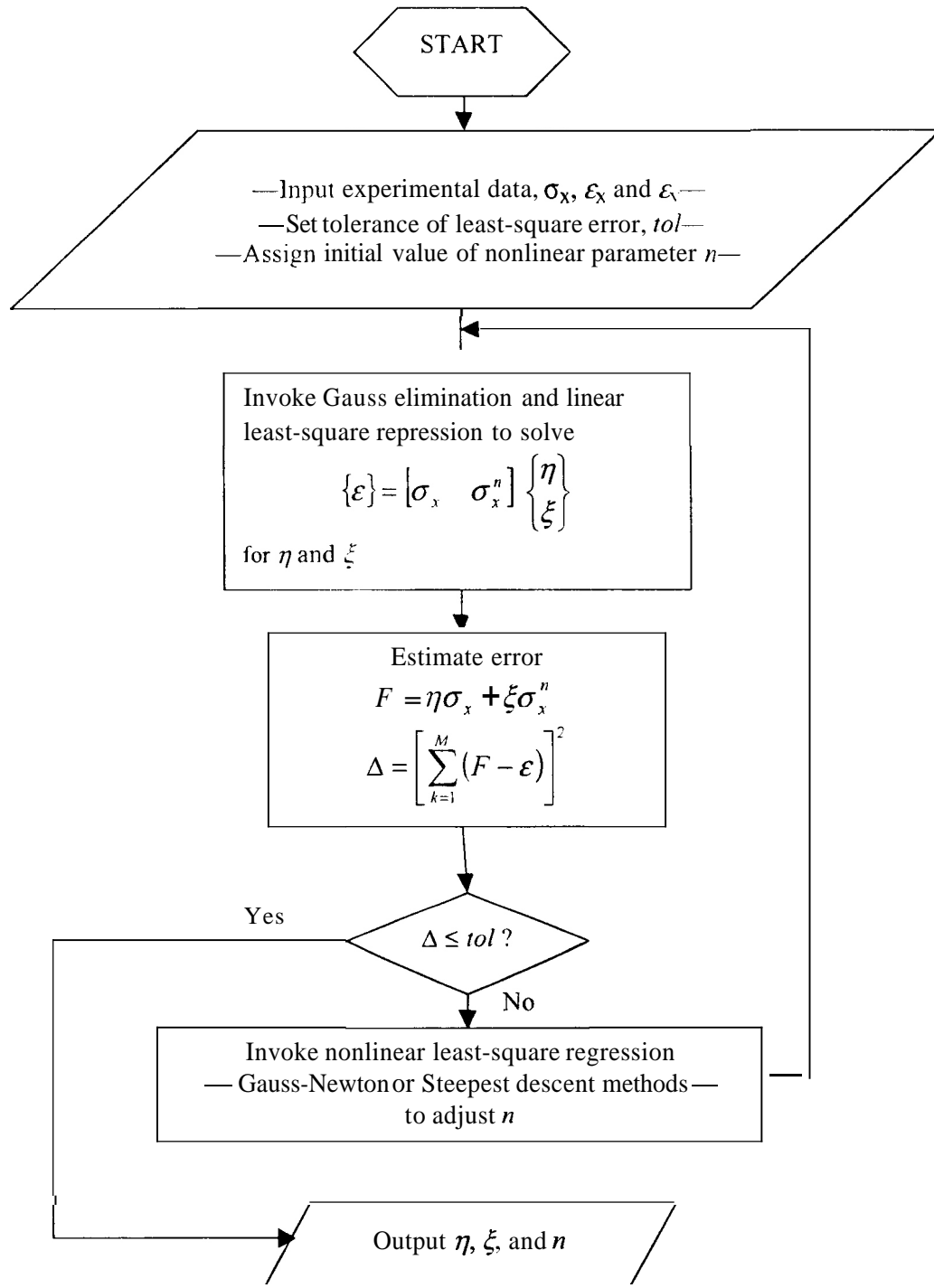
Equation (C.18) expresses the plastic strain-stress relation in an off-axis unidirectional composite under a uniaxial load. This shows that under a certain stress level the corresponding plastic strain is determined by the material plastic properties n , A , and a , where a is embedded in $h(\theta)$.

In the case of laminates, all individual plies, oriented at different angles about the load direction, are assumed to undergo the same strains E_x , E_y , and γ_{xy} . To ascertain this commonality of deformation at each stage of loading, with $h(\theta)$ varying from ply to ply, it is necessary to perform an incremental computation because the plastic components of strain vary nonlinearly with stress.

REFERENCES

1. C. T. Sun and J. L. Chen, "A Simplified Flow Rule for Characterizing Nonlinear Behavior of Fiber Composites," *J. Comp. Mater.*, **23**, October 1989, pp. 1009–1020.

**Appendix D. OPTIMAL NONLINEAR LEAST-SQUARE DATA FITTING
 SCHERIE TO DETERMINE THE PLASTIC
 PARAMETERS A , A , AND n**



Appendix E. A MATHEMATICAL DEMONSTRATION FOR THE DEPARTURE FROM QUASI-ISOTROPY CAUSED BY NONLINEARITY

Though not supported by experimental data, it is possible to provide a straightforward demonstration for the fact that the response of quasi-isotropic laminates becomes orientation dependent in the nonlinear range of stress-strain behavior by means of a simplified nonlinear formulation.

For this purpose, assume that the basic stress-strain relations of a unidirectional ply are given by

$$\begin{aligned}\sigma_1 &= Q_{11}\varepsilon_1 + Q_{12}\varepsilon_2, \\ \sigma_2 &= Q_{12}\varepsilon_1 + Q_{22}\varepsilon_2, \\ \sigma_6 &= f(\varepsilon_6).\end{aligned}\tag{E.1}$$

Thus, Eq. (E.1) presumes that all nonlinearity dwells in the stress-strain response in shear alone. Obviously, $f(\varepsilon_6) = -f(-\varepsilon_6)$ and $\lim_{\varepsilon_6 \rightarrow 0} f(\varepsilon_6) = Q_{66}$.

Straightforward manipulations of Eq. (E.1) yield the following expressions for the response of a quasi-isotropic laminate under uniaxial stress applied at an angle ϕ about the X_1 axis:

$$\begin{aligned}\sigma_x &= \frac{1}{2} (m^4 + n^4) (Q_{11} + Q_{22}) + 2m^2n^2Q_{12} \varepsilon_x \\ \sigma_x &= \left[\frac{1}{2} (m^4 + n^4) (Q_{11} + Q_{22}) + 2m^2n^2Q_{12} \right] \varepsilon_x \\ &\quad + [m^2n^2 (Q_{11} + Q_{22}) + (m^4 + n^4)Q_{12}] \varepsilon_y \\ &\quad + mn [f\{(m^2 - n^2) \gamma_{xy} + 2mn (\varepsilon_x - \varepsilon_y)\} - f\{(m^2 - n^2) \gamma_{xy} - 2mn (\varepsilon_x - \varepsilon_y)\}],\end{aligned}\tag{E.2}$$

where $m = \cos\phi$ and $n = \sin\phi$.

In the special case that $\phi = 22.5^\circ$, the above expression reduces to

$$\sigma_x = \frac{1}{8} [3(Q_{11} + Q_{22}) + 2Q_{12}] \varepsilon_x + \frac{1}{8} [(Q_{11} + Q_{22}) + 6Q_{12}] \varepsilon_y + \frac{\sqrt{2}}{2} \tilde{f} \left\{ \frac{\sqrt{2}}{2} (\varepsilon_x - \varepsilon_y) \right\}\tag{E.3}$$

While, for $\phi = 0^\circ$, one obtains

$$\sigma_x = \frac{1}{8} [3(Q_{11} + Q_{22}) + 2Q_{12}] \varepsilon_x + \frac{1}{8} [(Q_{11} + Q_{22}) + 6Q_{12}] \varepsilon_y + \frac{1}{2} f(\varepsilon_x - \varepsilon_y).\tag{E.4}$$

Note that under uniaxial tension $\varepsilon_6 = 0$ for both $\phi = 0^\circ$ and $\phi = 22.5^\circ$.

The essential theme of the above expressions is that they clearly demonstrate that Eqs. (E.3) and (E.4) predict different results. The difference is entirely due to the fact that, in view of the nonlinear character of $f(x)$, $\frac{1}{\alpha} f(\alpha x) \neq f(x)$. It also follows that in the linear range, that is, as $f(x) \rightarrow Q_{66}x$, the aforementioned inequality becomes an equality and quasi-isotropy prevails.

Nevertheless, it is worth noting that, while demonstrating the departure from quasi-isotropy due to nonlinearity, it can be shown that the current formulation predicts that the response at 22.5° is stiffer than that at $\phi = 0^\circ$. Such a prediction is, of course, contradicted by data.

INTERNAL DISTRIBUTION

- | | |
|---------------------|-----------------------------|
| 1-2. R. L. Battiste | 13-14. M. B. Ruggles-Wrenn |
| 3. R. G. Boeman | 15. S. Simunovic |
| 4-6. J. M. Corum | 16. P. A. Sklad |
| 7. D. L. Erdman | 17. C. C. Southinayd |
| 8. J. G. Hansen | 18. J. M. Starbuck |
| 9. A. Ionita | 19. C. D. Warren |
| 10. V. Kunc | 20-23. Y. J. Weitsman |
| 11. E. Lara-Curzio | 24. R. E. Ziegler |
| 12. R. E. Norris | 25. ORNL Laboratory Records |

EXTERNAL DISTRIBUTION

- 26-28. S. Deng, University of Tennessee. Department of Mechanical and Aerospace Engineering, 307 Perkins Hall, Knoxville, TN 37996-2030
29. M. M. Fisher. American Plastics Council. 1300 Wilson Boulevard. Suite 800, Arlington, VA 22209
30. R. B. Freeman, The Budd Company, 1515 Atlantic Boulevard, Auburn Hills. MI 48326
- 31-60. L. Berger. Automotive Composite Consortium. General Motors, 30500 Mound Road, Mail Code 480-106-710. Box 9055, Warren, MI 48090-9055
61. J. M. Henshaw. Department of Mechanical Engineering, The University of Tulsa. 600 S. College Avenue, Tulsa. OK 74 104-31 89
62. G. A. Holmes. National Institute of Standards and Technology, Bldg. 224, Room B116, Mail Stop: Room B 108. Gaithersburg?MD 20899
63. D. Kossak. Cambridge Industries, 29333 Stephenson Highway, Madison Heights, MI 48071
- 64-66. X. Li. University of Tennessee! Department of Mechanical and Aerospace Engineering, 307 Perkins Hall. Knoxville, TN 37996-2030
67. S. R. Reeve, National Composite Center. 2000 Composite Drive, Kettei-ing, OH 45420
68. C. R. Schultheisz. National Institute of Standards and Technology, Building 224, Room A209, Gaithersburg, MD 20899
69. T. D. Seagrave, Bayer Corporation, 100 Bayer Road, Pittsburgh, PA 15205
70. L. V. Smith, Washington State University. School of Mechanics and Materials Engineering, Pullman, WA 99164-2920
71. D. Stewart. Stewart Automotive Research, LLC, 1260 Shotwell Street, Houston, TX 77020
72. X. J. Xin, Department of Mechanical and Nuclear Engineering, Kansas State University, 338 Rathbone Hall, Manhattan, KS 66506-5205
- 73-76. J. A. Carpenter. U.S. Department of Energy, 1000 Independence Avenue, SW, Washington, DC 20585
77. M. Rowllins, U.S. Department of Energy. Oak Ridge Site Office, Oak Ridge, TN 37831
78. S. Diamond, U.S. Department of Energy, 1000 Independence Avenue, SW, Washington, DC 20585

1
2
3
4
5
6
7
8
9
10
11
12
13
14
15
16
17
18
19
20
21
22
23
24
25
26
27
28
29
30
31
32
33
34
35
36
37
38
39
40
41
42
43
44
45
46
47
48
49
50
51
52
53
54
55
56
57
58
59
60
61
62
63
64
65
66
67
68
69
70
71
72
73
74
75
76
77
78
79
80
81
82
83
84
85
86
87
88
89
90
91
92
93
94
95
96
97
98
99
100